Compression/expansion within a cylindrical chamber: Application of a liquid piston and various porous inserts

A Thesis
SUBMITTED TO THE FACULTY OF
UNIVERSITY OF MINNESOTA
BY

Bo Yan

IN PARTIAL FULFILLMENT OF THE REQUIREMENTS
FOR THE DEGREE OF
MASTER OF OR SCIENCE

Terrence Simon, Perry Li

August 2013

© Bo Yan 2013
ALL RIGHTS RESERVED

Acknowledgements

I would like to express my deepest gratitude to my advisers Terry Simon and Perry Li, for their guidance, patience and persistent support. I would also like to thank my research colleagues and friends Chao Zhang, Jacob Wieberdink, Farzad Shirazi, Pieter Gagnon and Mohsen Saadat for their collaboration and support. Meanwhile, I want to thank Professor James Van de Ven for his insightful suggestions and helpful discussions. You all have been tremendously helpful. Much thanks to my dad Dinggong Yan, and my mom Suyuan Zhou, without your unconditional love and support, I would never come so far.

Support for this research comes from the National Science Foundation under grant number NSF/EFRI-1038294 and the University of Minnesota - Initiative for Renewable Energy and the Environment under project number RS-0027-11.

Dedication

This is for my awesome parents, Dinggong Yan and Suyuan Zhou.

Abstract

Efficiency of high pressure air compressors/expanders is critically important to the economic viability of Compressed Air Energy Storage (CAES) systems, where air is compressed to a high pressure, stored and expanded to output work when needed. Any rise in internal energy of air during compression is wasted as the compressed air cools back to ambient temperature. Similarly, a drop in temperature of the air during the expansion process would reduce the work output. Therefore, the amount of heat transfer between air and surrounding heat sink/source surfaces determines the compression/expansion efficiency. Slowing down the compression/expansion process would give more time for heat transfer, thus increasing the efficiency. However, it reduces the power of the compressor/expander which is undesirable for a CAES system. A porous medium inside the compression chamber and a liquid piston is an ideal candidate for effectively increasing the heat transfer area and, consequently, thermal efficiency of the compression/expansion process, without sacrificing power.

The present study focuses on experimentally testing and evaluating the effectiveness of various types of porous media, including two types of metal foam and two types of plastic interrupted plates of different pore size and porosities inside of a liquid-piston compression/expansion chamber. The liquid piston compression system is a cylindrical cavity first filled with air. As water is pumped into the bottom of the cavity, the air inside is compressed. Flow meters and pressure transducers are used to measure the volume and pressure changes during compression. Porous inserts of various designs are placed inside the chamber to reduce the rise in temperature as the air is compressed

and to reduce the temperature drop as the air is expanded. Compression and expansion efficiencies are investigated with and without the porous inserts. For the compression experiments, all the experiments are conducted with constant volume trajectories. However, in expansion experiments, the volume trajectories are determined by constant orifice opening area. The study shows that compression efficiency is increased from 77% without a porous insert to 94% with the best-performing, 40ppi metal foam insert at a compression ratio of 10 and compression time of 2s. Due to the significant amount of water trapping inside the metal foam, in the expansion tests, only interrupted plates are tested. The expansion efficiency is increased from 80% to 90% with the 2.5 mm characteristic size interrupted plate insert for expansion process at expansion ratio of 6 and expansion time of 2s. Normalized pressure volume trajectories and dimensionless temperature profiles are calculated and compared for different types of inserts.

It is concluded that adding a porous insert into the air space of a liquid piston compressor/expander is an effective means of boosting heat transfer rate and increase compression/expansion efficiency. It is recommended that future work is needed to optimize the pore size and layout of the porous insert and to couple other heat transfer augmentation schemes, including spray cooling trajectory optimization and control. Meanwhile, in order to investigate the compression/expansion process at a higher pressure and wider pressure ratios, a high compression/expansion setup is designed and being fabricated in order to have a better control the pressure-volume trajectory, and improve ease of operation. Detailed design requirements, specifications, system schematic, 3-D models and drawings are presented and discussed.

Table of Contents

Contents:

List of Tables

List of Figures:

Chapter 1

Introduction

1.1 Objectives of this program

Due to the growing concern on anthropogenic climate change and soaring fuel prices, there has been a strong emphasis on sustainability in the last decade. Renewable energy sources including hydroelectric power, wind power, solar, geothermal, biomass supplied 13.2 percent of the electricity produced in United States in 2012 [1]. Among all the renewable sources, wind power has grown the fastest. Currently, there is 60 gigawatts (GW) of wind capacity in United States, which contributes to roughly 3% of the total electricity consumed in this country. The growing speed is astonishing, it took only four years to grow from 20GW in 2008[2]. An aggressive but achievable goal made by President Obama is to derive 20% of the nation's energy from wind power by 2030 [3]. The progress in creating renewable sources being made is encouraging. However, integrating the energy generated by renewable sources into the current electric grid remains one of the major challenges in the power industry for decades. The intermittent nature of the renewable sources and the variations between generation and demand results in a deficiency in power supply during peak demand period (3:00pm to 8:00pm) and surplus in generation during off-peak hours (12:00am to 4:00am).The shortage in the peak period causes a soaring price of the electricity. For example, in Texas, the price cap for wholesale market can reach up to $5,000 per MWh (0.5c/kWh), nearly four times the national average price, and this price is expected to jump to $7000 per MWh in 2014 and

$9,000 per MWh in 2015[4]. The current solution is to turn on additional fossil fuel based power generation systems with rapid ramp rates, so called “Peaking power plants”, such as gas turbine fired power plants to meet the electricity shortage gap. While at late night, some of the power generation systems driven by renewable sources have to be lowered in power or even be shut down during the off-peak hours, wasting the potential energy that could have been derived from the renewable sources.

To ease the demand and generation variations and to allow more sustainable energy sources to the power mix, energy storage system can be implemented in the current power infrastructure. During off-peak hours, excessive energy generated by renewable sources could be stored and released during the high demand peak hours. It also increases the reliability and dynamic stability of the power system by providing steady, abundant energy reserves with rapid ramp rates. In addition, it is also capable of lowering the overall cost of a renewable energy power plant by downsizing the electrical collection and transmission lines to meet the average power production other than the peak power production [5]. Other benefits include increase flexibility for load balancing [6], potentially decrease the greenhouse gas emission, possibly lowering the electricity price, making the power generation system less susceptible to fluctuating fuel prices or shortage, etc. [7].

Many energy storage technologies have been developed, including pumped hydro, conventional compressed air energy storage, thermal storage, flywheels, super-capacitors, super-conducting magnets and a variety of batteries. Each type of energy storage system has its own comparative strengths and weaknesses. For extensive reviews on energy storage, readers may consult Chen et al.[8], Hadjipaschalis et al. [9], Zalba et al. [10] on

more specific review on thermal storage, Divya and Ostergaard [11] on battery storage technologies. In general, most energy storage systems suffer at least one of the following drawbacks: poor economic viability, low round-trip efficiency, high rate of self-discharge, low energy density, low power density, limited cycle life time, requiring exotic material and being site specific. One rising solution to address all of these problems is the open accumulator system, a compact and efficient compressed air energy storage which is highly scalable, with relatively high energy and power density characteristics and potentially high efficiency [22]. This system can be best categorized as mechanical-type energy source/storage and is best used to convert shaft power into compressed air before conversion to electricity.

The focus of the current research program is to develop a novel isothermal-compressed air energy storage system using the open-accumulator architecture. Its impetus is for off-shore wind turbine energy storage [12], but it is also capable of serving general storage purposes. Offshore wind power shares all the same benefits of onshore wind power relative to fossil based power. However, there are several additional benefits. Onshore wind resources in U.S. are mostly located in the middle of country, distant from population centers. Offshore high class wind zones are much closer to major population centers along the coast, hence significantly lowering the cost for high voltage transmission [13]. Offshore wind turbines could be placed far enough from shore to be inaudible and, possibly with low visibility to ease conflicts with the local residents. Furthermore, stronger and steadier coastal winds could leads to 150% increase in electricity generation [14] and 25 to 40% increase in capacity factor [15]. Moreover, larger turbines are more economically attractive, but the size of the onshore wind turbine

is limited by the transportation capability of the blades, tower and nacelle of the turbine. Mature marine technologies has been developed for building and shipping massive equipment for offshore oil/gas rigs and these technologies can be easily modified to transport and build large scale wind turbines. Some of the offshore turbines already exceed 5 MW [16] and soon will exceed 10 MW. For more complete ecological and economic cost-benefit analysis on offshore wind energy please consult Snyder and Kaiser [17].

Despite the staggering advantages of offshore wind energy over onshore wind, the largest drawback is that the offshore wind farm's overall cost is significantly higher than land based wind farms [18]. By coupling efficient compressed air energy storage system with an offshore wind farm could potentially lower the overall cost of the wind farm. The generator and transmission of the turbines could be sized based on mean power available, rather than the peak power. When wind is stronger than demand, excessive shaft power could be stored prior to electricity generation. When demand is higher, compressed air can be released to augment the total output. This could be achieved by the open accumulator system, which is a hybrid storage system that combines the power density advantage of hydraulics and the energy density advantage of pneumatics. A detailed description of open accumulator will be given in a later section.

1.2 Thesis objectives

The biggest challenge of the open-accumulator system is to be able to compress and expand air efficiently at high power. Since the storage medium is compressed air, the key to success is an efficient, power dense, high pressure ratio (up to 350:1) air compressor/expander.

When a compressor increases the air pressure, it also heats up the air. Energy spent on heating the air is the major loss for a compressor. During an expansion process, not only does the air pressure decrease, the temperature of air also decreases, resulting in shrinkage of the volume of air while decreasing the potential work output. Detailed principles will be discussed in chapter 2. Previous studies conducted shows that there are two different, but complementary, methods that could significantly increase the efficiency of an air compression/expansion process. The first one is to optimize the compression/expansion trajectory. A numerical optimization approach conducted by Sancken et al. [19] shows an optimized compression volume profile could result in 10 to 40% increase in storage power at a constant efficiency, more recent experimental study by Shirazi et al. [20] demonstrated the power density of a compression process with pressure ratio of 10 can be increased up to 20% under the same compression efficiency compared to linear volume trajectory. Even greater improvement is expected at higher compression/expansion ratio (such as 30-40).

The other approach is to increase the heat transfer rate between the air and heat sink/source during a compression/expansion process using porous medium inserts or spray cooling. Rice [21] shows that during a compression process with a compression ratio of 7, using a copper minitube array as an insert could results in 86% drop in peak temperature difference and a 32% increase in efficiency. While previous studies established basic directions, this thesis study is a continuation of previous approaches and focuses on experimentally validating the heat transfer augmentation aspect of the problem. In this study, a liquid piston experimental setup that is capable of compressing and expanding air up to 1.25MPa (182psi) has been developed to examine the

performance of various porous inserts. Pressure and volume of the air during compression and expansion processes are measured and calculated. Simple models are created using pressure and volume measurements to calculate the temperature change and efficiencies of the processes with and without added porous media. Two types of metal foam and two types of plastic interrupted plates are tested and evaluated quantitatively. In order to characterize the performance of porous media at a much wider power range and study the effect of spray cooling on the compression process, a high pressure compression/expansion system design is presented and discussed.

1.3 The open accumulator

The open accumulator proposed by Li and Van de Ven [22] is a hybrid between a conventional hydraulic accumulator and a pneumatic accumulator, inheriting the strengths from both technologies. Figure 1.1 shows a schematic of the open accumulator storage system coupled with a wind turbine. The open accumulator storage structure consists of an air compressor, a hydraulic pump/motor and an accumulator storage vessel. A dual operation mode is available in this configuration.

During the regular charging phase, mechanical shaft power from a wind turbine powers the water pump to drive the liquid piston air compressor and compresses ambient air to an elevated pressure which is then stored it in the accumulator. Meanwhile, the liquid at the bottom is discharged out of the accumulator to maintain the pressure inside the storage vessel. During the regeneration phases, air inside the accumulator is discharged into a liquid piston expander and expands in the expansion chamber to push the water through a water motor to generate electricity. Simultaneously, liquid is pumped into the accumulator to maintain constant pressure. In this mode, the total energy stored

in the accumulator is a function of the pressure and the amount of the air inside the accumulator. Since highly compressed air contains large amount of energy per unit mass, this mode takes the advantages of high energy density of pressurized air.

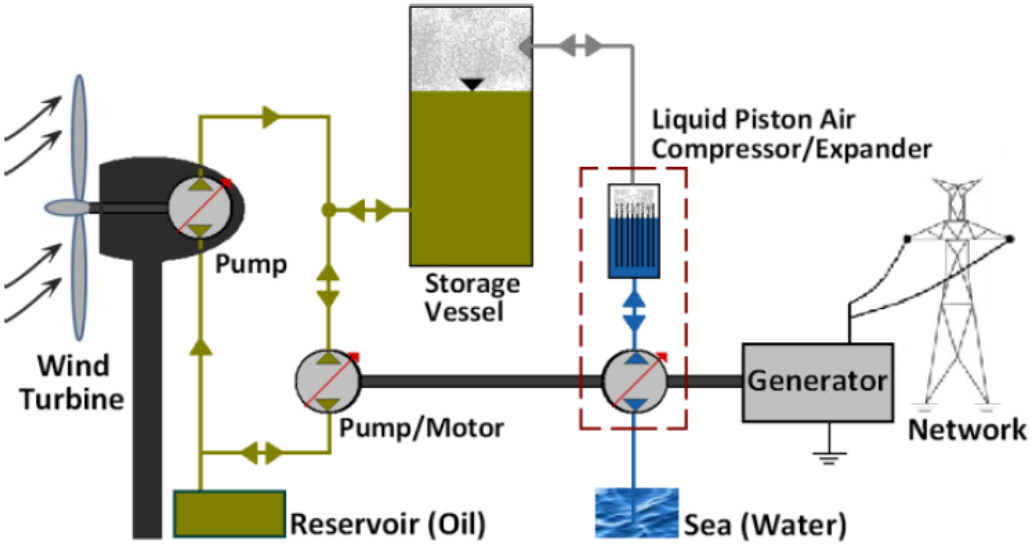

Figure1.1.A schematic of a proposed open accumulator compressed air energy storage concept coupled with offshore wind turbine (Adapted from [19])

The other mode is a high-power mode. Since a hydraulic pump/motor is more capable of absorbing/generating high power compared to an air compressor/expander. There are rare situations that transient high power should be released or absorbed. In this mode, pressure inside the accumulator is no longer maintained at a constant level, the mass of air remains the same but liquid is injected or discharged from the bottom of the storage vessel via the hydraulic pump/motor. The whole system behaves like a conventional hydraulic accumulator. In this mode, the open accumulator takes advantage of high power density of hydraulic fluid.

A conventional hydraulic accumulator usually consists of a pressure vessel with an enclosed inert gas chamber and an oil chamber, separated by a piston, diaphragm or a

bladder. The three most popular types of hydraulic accumulator configurations are shown in figure 1.2.

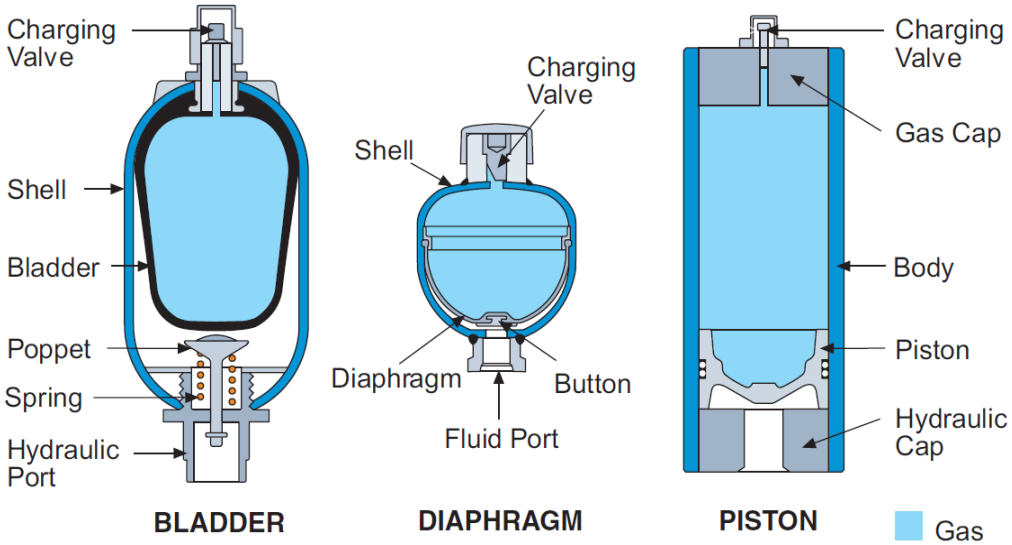

Figure 1.2: Typical bladder, diaphragm and piston accumulators (Adapted from [23])

The fixed volume inert gas chamber is pre-charged to a nominal pressure and energy is stored by pumping pressurized hydraulic oil into the oil chamber, thus shrinking the gas volume until the gas pressure is at the desired pressure. Energy is regenerated through expanding the compressed gas and discharging the stored oil back into a hydraulic circuit. This configuration is considered as a "closed" accumulator since the gas is always contained within the accumulator. During regeneration, the energy that could be extracted increases with expansion ratio. However, it is at the expense of increasing the total volume of the accumulator which is governed by the expanded air volume. Therefore, the energy density of a closed accumulator is fundamentally constrained. The optimal expansion ratio for a conventional accumulator that achieves the highest power density is only 2-3 [22] thus the closed accumulator suffers from a poor energy density which is at a magnitude of 10kJ/liter when stored to 35MPa, compared to 1MJ/liter for battery [22]. The open accumulator is an evolution from the conventional

hydraulic accumulator. While the air is being drawn and discharged into ambient, it does not require the accumulator to holds the expanded air. Meanwhile the pressure inside the vessel is a constant, thus the pressure ratio across the compressor/expander can be maintained at a much higher level compared to conventional accumulators. The energy density of an open accumulator is at least one order of magnitude higher than conventional hydraulic accumulators. Figure 1.3 shows a graphical comparison between the potential energy that could be derived from 'closed' and open accumulators:

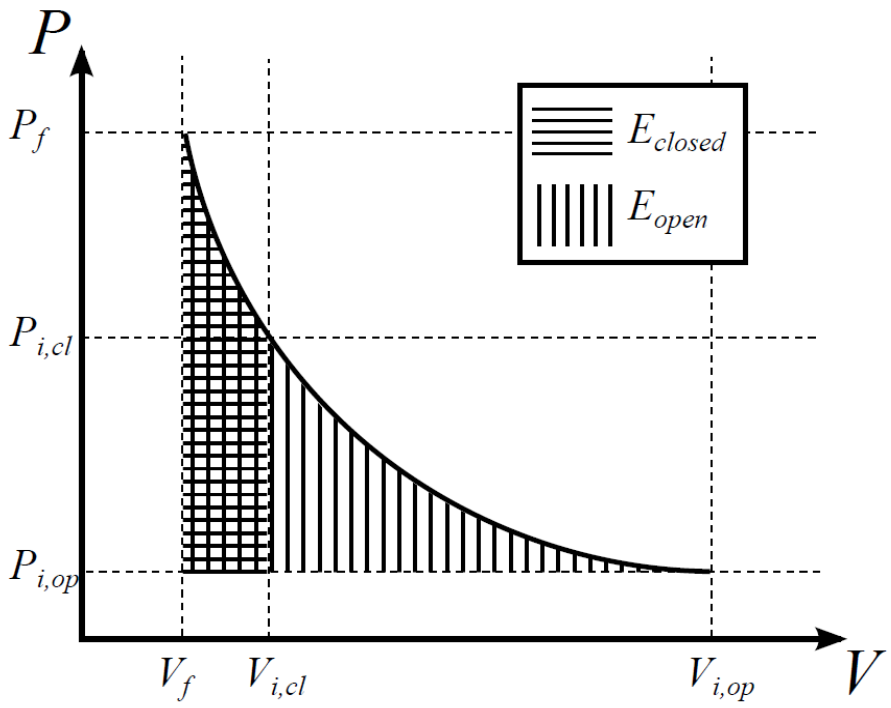

Figure 1.3: PV curve comparison between compression processes inside an open accumulator and closed accumulator. The volume for the open accumulator is V_f and the volume for close accumulator is $V_{i,cl}$. The total energy stored during a single stroke, from $(P_{i,op}, V_{i,op})$ to (P_f, V_f) is much greater than the energy stored for a closed, conventional accumulator from $(P_{i,cl}, V_{i,cl})$ to (P_f, V_f) (Adapted from [21])

A sample calculation from a previous study [12] shows it only needs a 509m^3 storage vessel at 35MPa to store the total energy generated from a 5 MW wind that is generating at an average of 3MW for 8 hours (86GJ), resulting in an energy density of

169kJ/liter. The volume of 509m^3 seems to be a large volume, however, given the fact that a 5MW turbine has a rotor diameter of 126m and hub height of 90m [16], there is plenty of room to integrate the storage vessel into the turbine structure.

The concept of open accumulator is very promising. However, to store and regenerate such a huge amount of energy is a major technical challenge. The major loss occurs during the compression and expansion processes of air at high pressure ratios. During air compression, air is not only pressurized but also heated, and the internal energy of the air increases. Unfortunately, the compressed air product will cool down to ambient temperature when stored for long enough time, thus decreasing the pressure and potential energy stored. During the expansion process, temperature of air decreases resulting in a lesser expanded volume across a certain pressure ratio thus decreasing the work output. However, if the air can be compressed and expanded isothermally, there will be no input work wasted to heat up the air and no output work reduction by cooling of the air.

Driven by the compactness and high efficiency requirements of the open accumulator, pioneering computational studies and analysis has been conducted by Hafvenstein [24], focusing on the development of a diaphragm air compressor. However, his work shows that the diaphragm compressor cannot meet the heat transfer rate requirements. Continuation work has been conducted by Rice [21], who has proposed two piston compressor designs and both of them have been experimentally proven effective under low pressure (lower than 100 psi) and small pressure ratios (less than 10). The first one is a conventional solid piston-in-cylinder compressor with high thermal capacity porous mesh material inserted in the air chamber to augment heat transfer with

optimized motion of the piston. The second design is a liquid piston with a copper minitube array as inserts. Both designs show significant decrease in peak air temperature during compression. Among those two approaches, the liquid piston with minitube array seems to have better performance and has the potential to be successful under high pressure condition. It seems the combination of liquid piston and porous media is a promising solution to increase gas compression/expansion efficiency. The remaining contents of this chapter review literature relevant to the liquid piston compression.

1.4 Liquid piston

The liquid piston is a concept using water column other than solid piston to compress or expand gases. It can be used in a pump or an engine. The earliest liquid piston application is originally designed and published by H.A. Humphrey [25] and is well known as the Humphrey pump, dating back to 1906. It is one of the earliest internal combustion engines. It runs on an Atkinson cycle. Force exerted by an explosion of a mixture of fuel and air acts directly on the surface of water thus forcing it to an elevated position and when gas pressure drops, a water valve is opened and water is sucked into the cylinder again. However, due to its poor efficiency it was not a very popular design. Further development involve Fluidyne Stirling engine, where working gas in a U-shape liquid column is heated with a heat source and causes the water lifting and suction. The major application of this technology is various kinds of solar pumps developed for developing countries [26]. However, the main disadvantage is its instability under changing loads [27]. It seems most previous works on liquid piston were focused on one of its functionalities, pumping water. However, Van de Ven and Li [28] discovered an alternative way of utilizing liquid piston, to directly compress a gas in a fixed volume

chamber. A simple liquid piston compression/expansion configuration is shown in figure 1.4, where liquid driven by a hydraulic pump/motor can be used to compress or expand gas into or out of an air reservoir.

The liquid piston under this configuration acts like a hydraulic to pneumatic transformer [28]. The mechanical reciprocating piston suffers the design trade-off between high leakage loss and high sealing friction [29]. Liquid piston, on the other hand, is completely air tight. Gases can be compressed or expanded at extremely high pressure without worrying about leakage loss. However, viscous loss is negligible when piston diameter is large but could become significant as the piston bore size gets smaller [28].

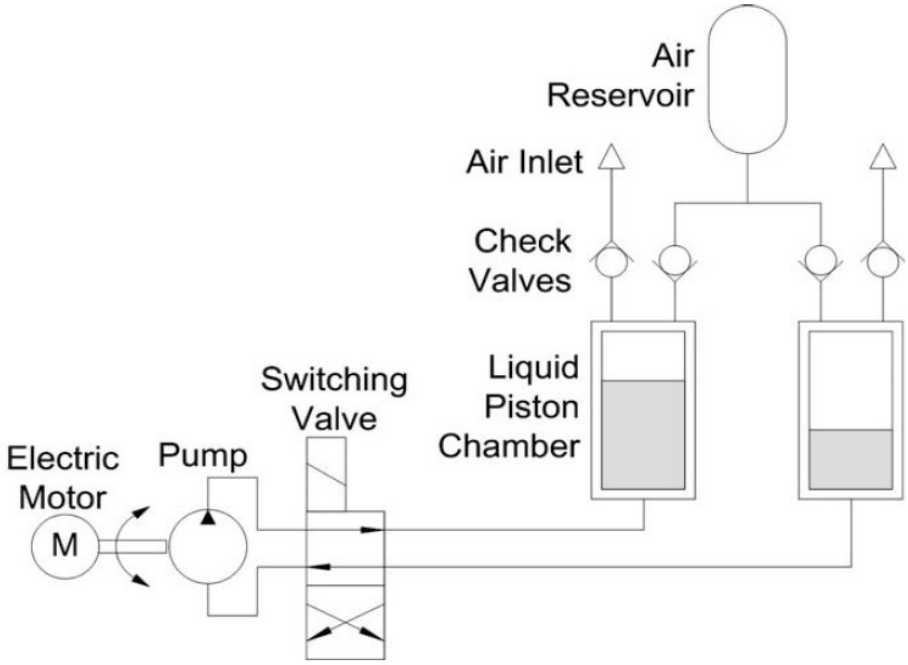

Figure 1.4: Liquid piston configuration where a hydraulic pump drives two liquid piston chambers using a switching valve. In this setup, one chamber is always filling while the other is emptying (Adapted from [28])

In addition, the liquid piston is capable of dramatically increasing the heat transfer rate inside the gas chamber. Heat transfer inside a reciprocating piston is quite

complicated due to the changing flow regime, roll-up vortices, port-induced swirls and rapidly changing heat flux [30]. It is even more complicated when considering the phase shift between the bulk gas and wall temperature [31]. Since the dominant heat transfer mode inside the chamber is convection and the bottleneck of increasing heat transfer rate inside of a solid piston is a low surface area to volume ratio (specific surface area), attempts have been made to increase this ratio by using smaller-bore-diameter cylinders and long strokes or larger bore diameters with shorter strokes. This would result in either a very large or a very small aspect ratio on the piston, which would make the piston not practical. Since the liquid piston is capable of conforming to an irregular shaped gas chamber, surface area to volume ratio inside the chamber can be radically increased using numerous small diameter cylinders, fins or any other variety of geometries [28]. Previous computational study conducted by Wong [32] shows a highest compression efficiency of 86.4% with a 3mm bore radius and a 5cm long cylinder under a compression ratio of 9. When numerical study from Van de Ven and Li [28] shows a liquid piston with a bore diameter of 9.0E-4 m and 50,000 cylinders can reach an efficiency of 83.3% at a compression ratio of 9.5 while similar size reciprocating piston operated under the same conditions only has an efficiency of 70%.

However, surface stability is the bottleneck that stops liquid piston from operating at high frequency stably. Previous studies performed by Taylor and Lewis [33,34] show that when two superposed fluids of different densities are accelerated in the direction perpendicular to the interface, the surface stability is governed by the acceleration direction and the densities of those two fluids. Taylor shows that if the acceleration of the denser liquid is larger than gravity, the interface between two liquids becomes unstable.

Air and liquid has a density ratio of nearly 1000. This limits the stable operating frequency of a liquid piston to be lower than 1Hz. None of the experiments conducted in this study exceeds this limit.

In the present thesis, a liquid piston is used to directly compress and expand the air over a wide range of power densities.

1.5 Porous medium inserts

To further boost the heat transfer rate, a liquid piston can be coupled with various porous inserts. Porous media with its high surface area to volume ratio, intense mixing of the fluid flow and large thermal conductivity has emerged as a promising solution for heat transfer augmentation strategies. Other studies found also that porous media are capable of increasing the radiation heat transfer between the gas medium with a weak emittance and the wall [35].

Sintered metal foam is a new type of porous media with an open-cell structure. Due to its light weight, high thermal conductivity, high strength and cost effective characteristics, open-celled metal foam has been rapidly introduced to different areas and is serving as compact and efficient heat exchangers, heat sinks for electronic devices [36], regenerators for thermal engines [37], condensers in cooling towers, etc. In this study, two types of aluminum metal foam manufactured by ERG Aerospace Corp [38] are tested as inserts used in a liquid piston compressor. Detailed properties of the foam are discussed in chapter 3. Inspired by a mircrofabricated segmented-involute-foil regenerator designed for a space Stirling engine [39, 40], Zhang et al. [41] designed a series of interrupted-plate heat exchangers specifically for a liquid piston. These heat exchangers not only dramatically increase the surface area to volume ratio but also

introduce new thermal boundary layers as flow passes through the interrupted plates. Two of the best performing designs are made using 3D printer. They are experimentally tested in this study.

It seems that the combination of liquid piston and porous inserts is a potential solution to an efficient and power dense compressor/expander process. This study is a continuation of Rice's work [21], but looking at higher pressure ratios (10 compared to 7) and more types of porous inserts. Each type of porous insert is tested experimentally and its performance is evaluated quantitatively at a wide range of power densities for both compression and expansion processes. The results in efficiency gain and drop in bulk air temperature rise are compared to baseline compression/expansion processes without any inserts.

1.6 Outline of thesis

This thesis is organized into three sections. The first section includes the first two chapters, the introduction and the system model. Chapter 1 introduces the purpose of this program and purpose of this thesis. In addition, it also gives background information about the open-accumulator and liquid piston. In chapter 2, basic principles of open accumulator CAES system are demonstrated visually and graphically. Governing equations are derived with appropriate assumptions.

The second section, consisting of chapter 3 through 6, describes and discusses the experimental setup, methods and results for compression and expansion experiments. Chapter 3 focuses on the compression processes while chapter 4 focuses on the expansion experiments. In chapter 5, results are presented and discussed for both experiments. Chapter 6 gives the conclusion and discussion of the lower pressure experiments.

The third section is the continuation part of the study, it consists of chapter 7 which summarized the pros and cons learnt from the low pressure system and describes a design process for a new system that is capable of achieving compression/expansion processes to much higher pressures and across much wider pressure ratios. Design requirements and specifications are presented and discussed. Detailed engineering drawings are also included in the Appendix.

Chapter 2

System model

2.1 Basic liquid piston principles:

The purpose of this chapter is to demonstrate the principle of the liquid piston and to develop the governing equations under appropriate assumptions. This is done for both compression and expansion processes with and without porous inserts in the liquid piston chamber. Simple governing equations for power density, compression and expansion efficiency under the Open-Accumulator architecture will be presented and compared to a conventional CAES system. Emphasis is placed on the principles by which the porous inserts improve the efficiency of the liquid piston air compressor in the open accumulator infrastructure while retaining the high power density. The basic principle of the liquid piston is described by the following section.

The initial state of a cylinder-type pressure chamber for a compression stroke has a mixture of air and water shown in figure 2.1. The air is located in the top region, assumed to be an ideal gas at initial temperature of T_0, initial pressure of P_0 and volume of V_0. Liquid water at room temperature is located at the bottom of the cylinder. The cylinder is assumed to be surrounded by ambient air at T_0. In order to compress the air, water is pumped into the bottom of the cylinder. During the compression process, work is done on the air by the liquid piston. This raises the temperature and pressure of air to a final state T_f , P_f and V_f. According to the first law of thermodynamics, the total change in internal energy, U , of the air is equal to the total amount of flow work W_{in} done on the

air minus the total amount of heat transfer, Q, from the air to surroundings, shown in equation 2.1:

$$\Delta U_{air} = \int_{V_0}^{V_f} P dV_{work\ input} - Q_{air\ to\ sink} \tag{2.1}$$

For the purpose of energy storage, the increase in pressure results in an increase in potential energy or the so called exergy of the air. Any work done to raise the internal energy of air during compression is wasted as the compressed air would eventually cool back to ambient temperature when stored in the accumulator. In order to minimize the increase in internal energy, heat transfer between the air and surroundings should be augmented. Since the primary heat transfer mode for this application is convection, the total amount of heat transfer is determined by the convective heat transfer coefficient, h, and total heat transfer surface area, A_T between air and surrounding. Porous inserts can be placed inside the compression chamber shown in figure 2.2 to significantly increase the heat transfer surface area, A_T. With much more surface area, under the same compression ratio, more heat transfer will occur, thus minimizing the increase in internal energy. The temperature of the final state would be much lower than the cases without any inserts. For this study, four different types of inserts, two aluminum metal foam geometries and two ABS plastic interrupted plate geometries are tested and compared at different compression times. Detailed properties for the inserts and experimental conditions will be discussed in Chapter 4.

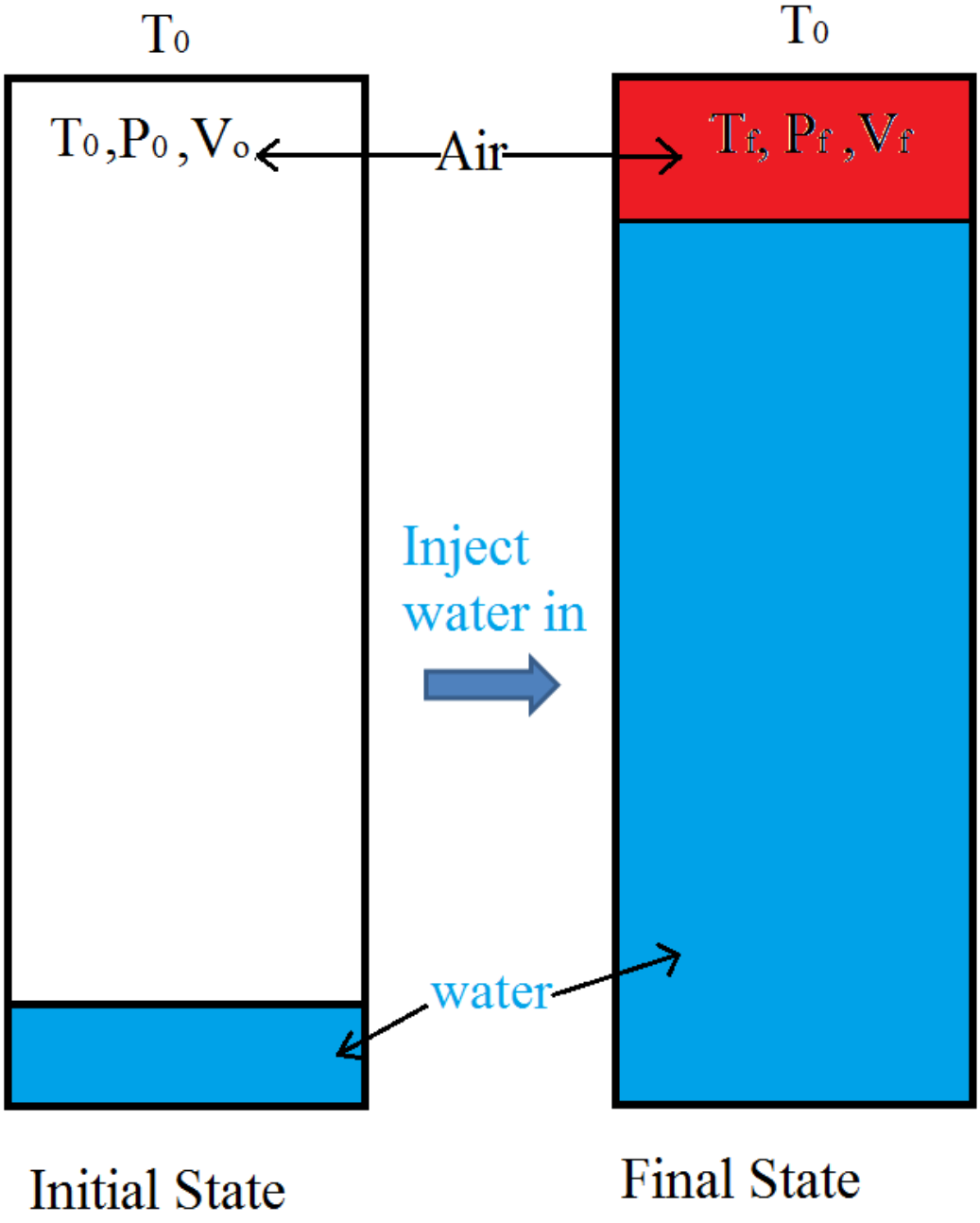

Figure 2.1: Principle of liquid piston compressor, with initial state T_0, P_0, V_0 at left to final state T_f, P_f, V_f (compressed) state at right. During the compression air is heated and heat transfer occurs between the heated air and surroundings.

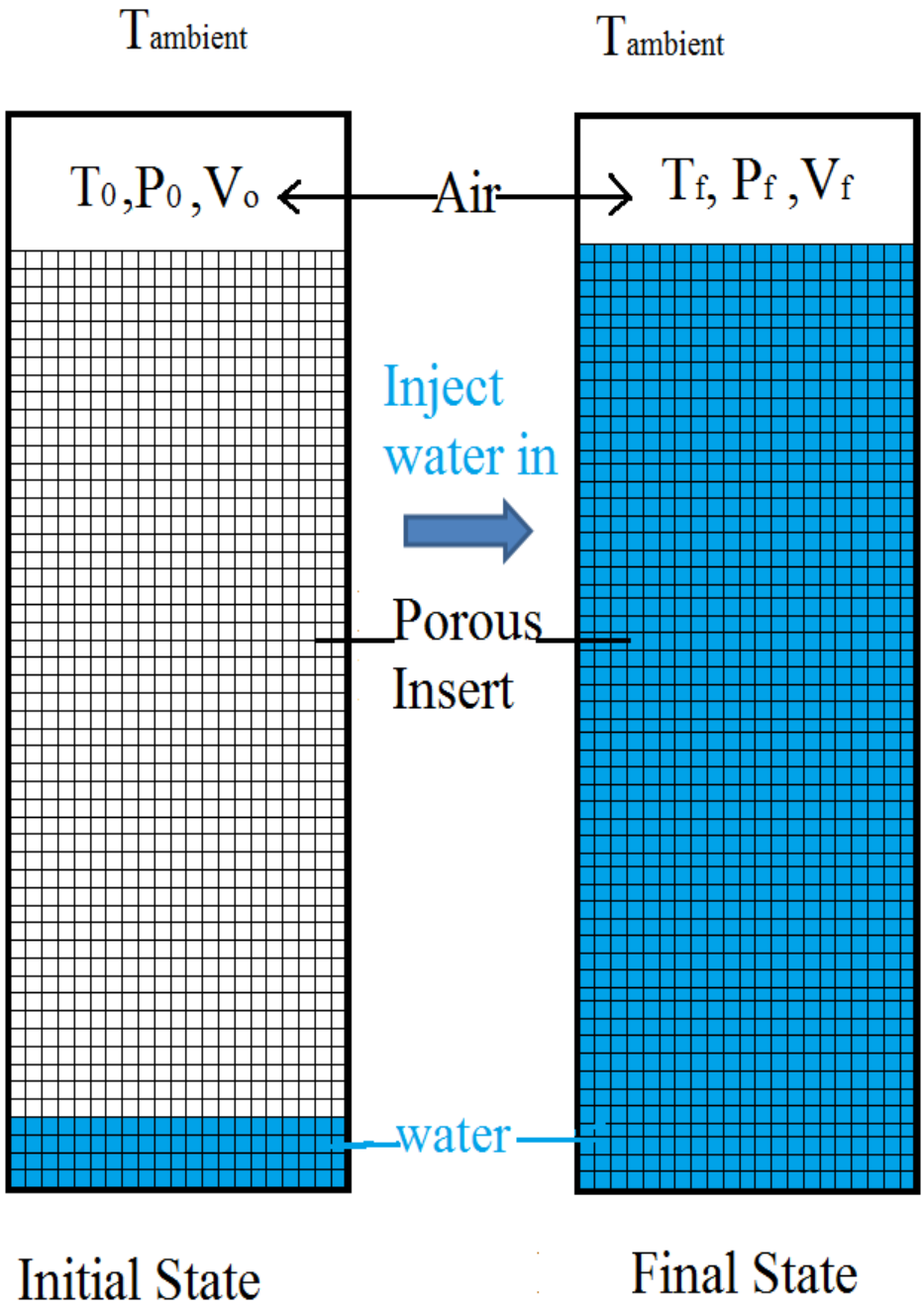

Figure 2.2: Principal of liquid piston compressor with porous inserts. Air with initial state T_0, P_0, V_0 at left to final state T_f, P_f, V_f (compressed) state at right. During the compression air is heated and the inserted material acts as a heat exchanger and a heat sink. Total amount of heat transfer between the air and ambient is increased. (The void on the top is just for convenience to show the initial and final states, porous inserts tested in this study are fully extended to the top cap of the chamber)

Under the regeneration stage, a liquid piston can be used to extract energy from the compressed air. Pressurized air at an initial state T_0, P_0, V_0 is stored in the upper section of a cylinder-type chamber in which water resides beneath (shown in the left side of figure 2.3). As the water beneath gets discharged into a water turbine, the air is expanded into its final state of T_f, P_f, V_f shown in right side of the figure 2.3. During the expansion process, both pressure and temperature of the air decrease as air is doing work upon the surroundings. According to the first law of thermodynamics, the change in internal energy, U, of air is equal to the total amount of heat transfer from surrounding into the air, Q, subtracted by the flow work output done on the surroundings, W_{out}, shown in equation 2.2:

$$\Delta U_{air} = Q_{source\ to\ air} - \int P dV_{work\ output} \qquad (2.2)$$

In order to get more work output with the same amount of air under the same expansion ratio, more heat transfer from the surrounding is needed. Just like the same principle for the compression process, porous inserts can be placed inside the expansion chamber shown in figure 2.4 to increase the total heat transfer surface area, A_T. With the presence of porous inserts, the final air temperature, T_f, will be higher than for cases without inserts and more work output can be extracted under the same expansion ratio.

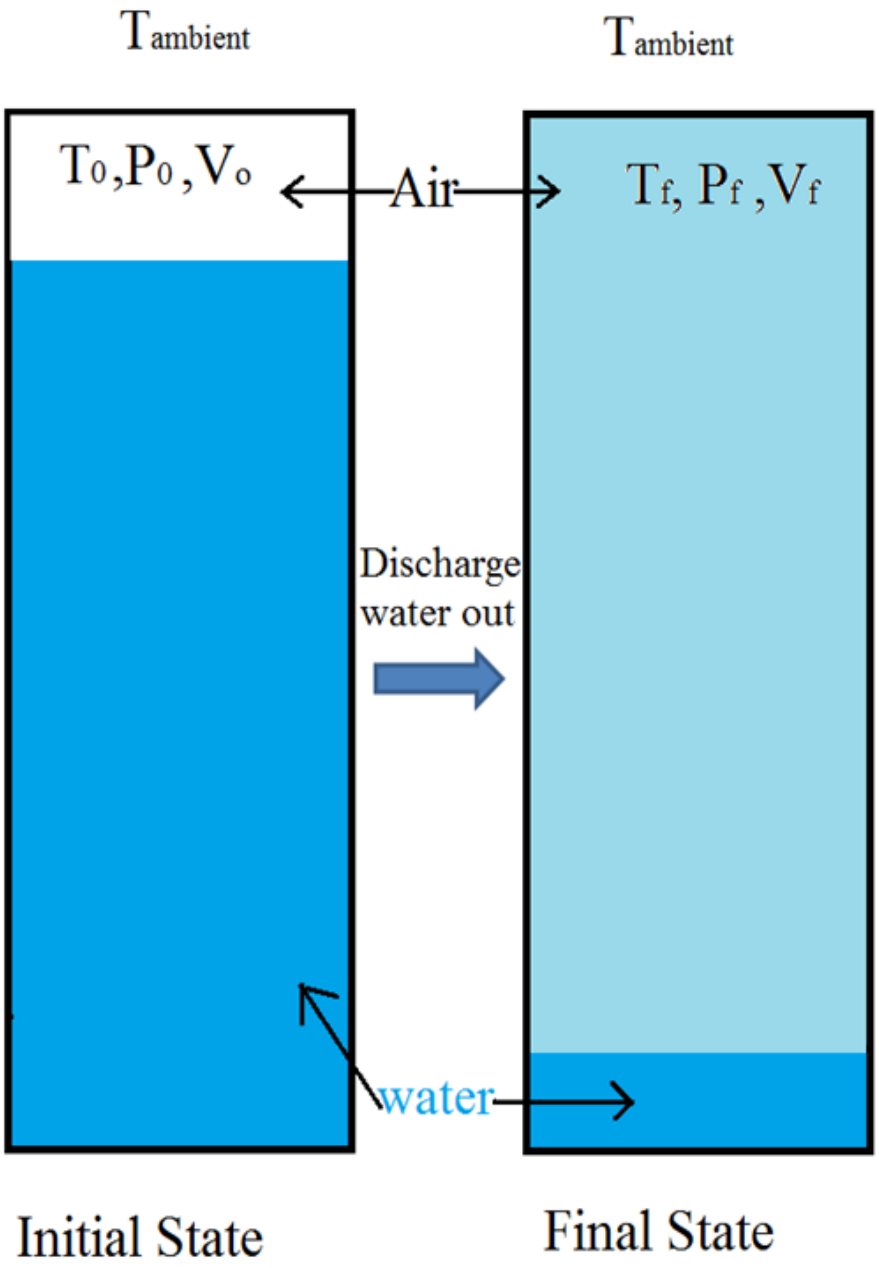

Figure 2.3: Principle of liquid piston expander with no porous inserts. Air with initial compressed state T_0, P_0, V_0 at left to final state T_f, P_f, V_f (expanded) state at right. During the expansion air is doing work on liquid-air inter- surface, temperature and pressure of air drops. Heat transfer occurs between the cooled air and surroundings

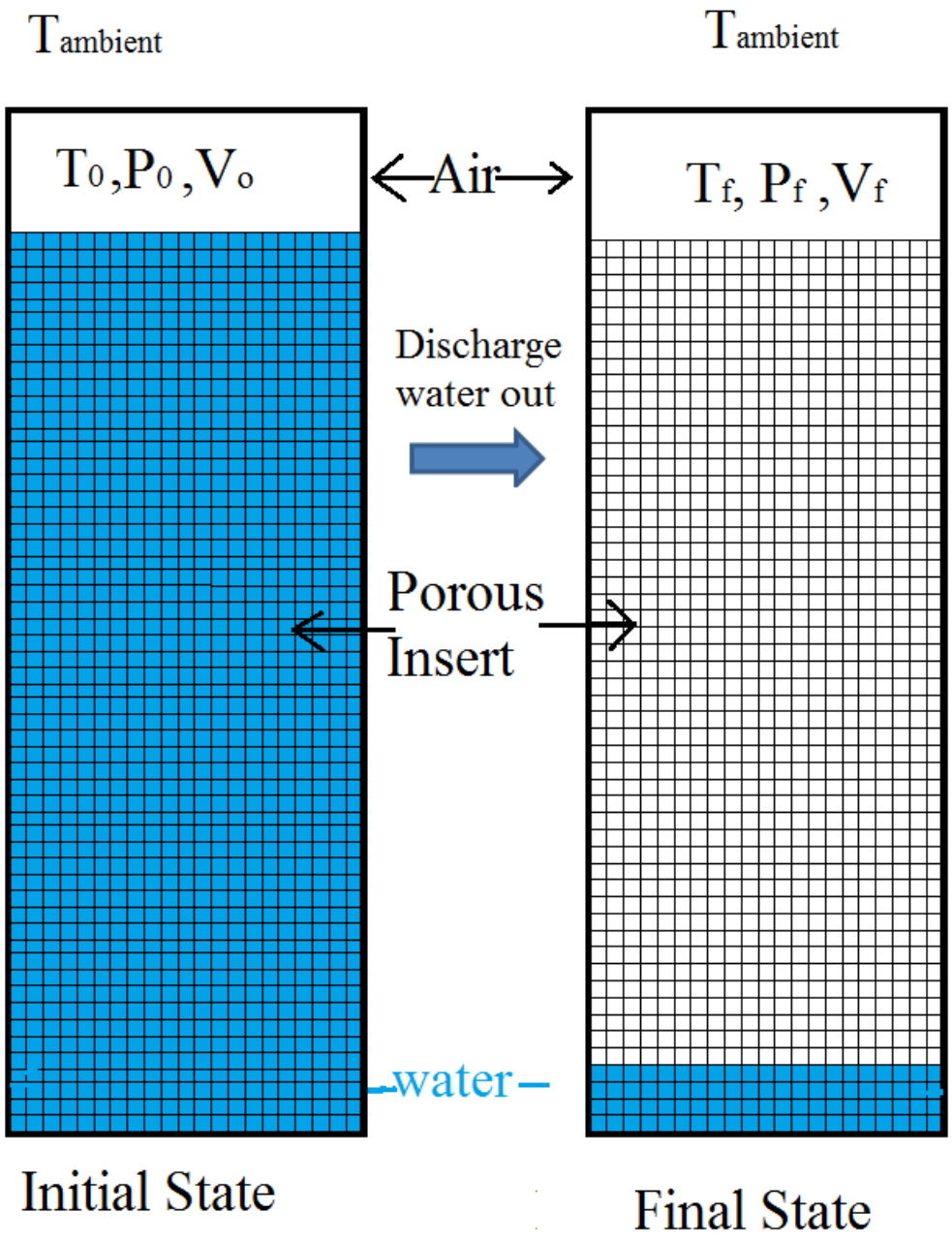

Figure 2.4: Principle of liquid piston expander with porous inserts. Air with initial state T_0, P_0, V_0 at left to final state T_f, P_f, V_f (compressed) state at right. Porous inserts acts as a heat sink and a heat exchanger. Total amount of heat transfer between the air and surroundings is augmented thus the final air temperature T_f and total work output W is higher than the cases without any insert

2.2 Figures of merit

In this section, example PV trajectory diagrams are presented to illustrate the compression and expansion process of open accumulator CAES using a liquid pistons. The shaded areas in the PV diagrams are used to represent the work input and output. Ideally, compression and expansion processes should be studied as a cycle. Due to some limitations in the experimental setup, compression and expansion processes could only be studied separately. Both the compression process and the expansion process are analyzed separately in the following P-V trajectory diagrams.

2.2.1 P-V trajectories for Open-Accumulator CAES system

For a liquid piston compression process in an open-accumulator CAES system, air at an initial state of T_0 , P_0, V_0 is compressed in a liquid piston through a PV trajectory $\zeta_c(P(t), V(t))$ to a second state of T_c , P_c, V_c with a compression ratio of $r = \frac{P_c}{P_0}$ as shown by the solid line in figure 2.5. After the compression, the heated compressed air product is ejected into the open accumulator and cooled isobarically to a smaller volume, V_{iso} , by adding liquid into the bottom of the accumulator until the air returns to a final stored state of T_0 , P_c, V_{iso}. The total amount of work input W_{in} to store the final air product can be calculated as:

$$W_{in} = \int_{v_0}^{v_c} (P(t) - P_0) dV + \left(1 - \frac{1}{r}\right)(P_c V_C - P_0 V_0) + (P_c - P_0) V_{iso} \qquad (2.3)$$

This equation is broken into three types of work input. The first term is the compression flow work, which is shown as the area shaded with horizontal lines under the compression trajectory $\zeta_c(t)$ in figure 2.5. The second term is the isobaric cooling work shown as the area shaded with the vertical lines bounded by isobaric line, P_c, and

isochoric lines, V_c, $and\ V_{iso}$. The third term is the pumping work required to push final product into the accumulator tank isobarically, which is represented by the area between isobaric lines P_c, and P_0 and the isochoric line, V_{iso}.

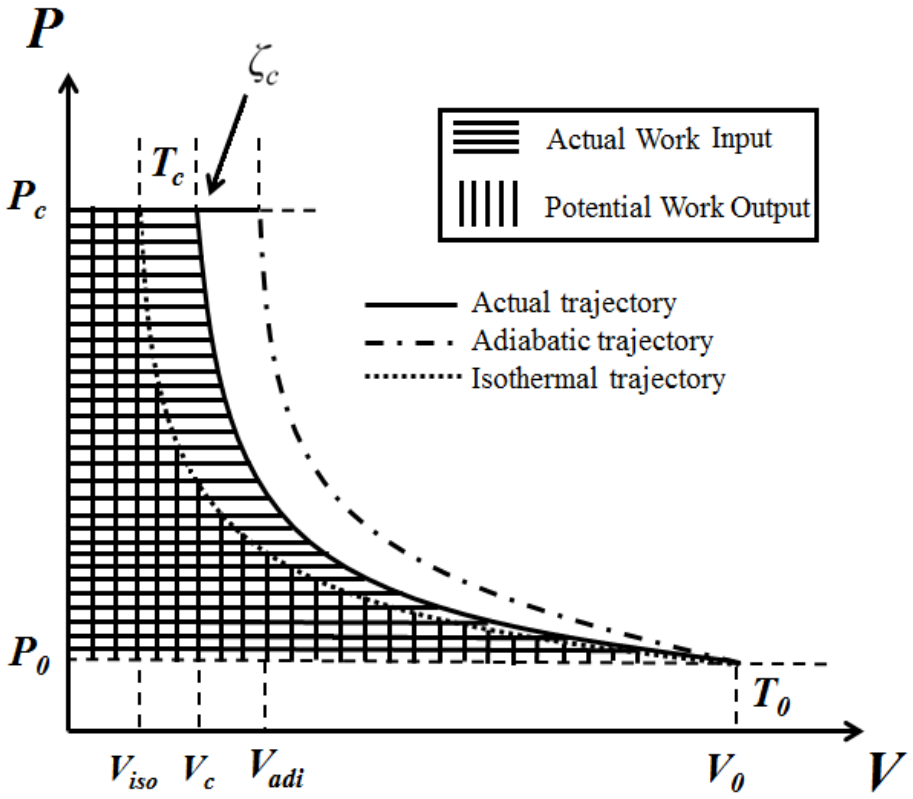

Figure 2.5: P-V curve showing compression trajectory ζ_c for a liquid piston in an open-accumulator system. The area shaded represents the actual flow work input required (horizontal lines) to compress air from P_0 to P_c and eject the final air product into the open-accumulator isobarically. Isothermal compression follows the dashed black trajectory. The total potential energy stored is the area under the thick dashed isothermal curve (vertical lines)

Once the air has been stored, the total potential energy E_P that could be extracted from the stored compressed air product is shown as the area shaded by the solid vertical lines. This can be calculated as:

$$E_P = (P_c - P_0)V_{iso} + P_0V_0\left[\ln(r) + \frac{1}{r} - 1\right] \tag{2.4}$$

This expression of potential work output can be broken into two terms. The first term is the motoring work from discharging the air from the storage tank isobarically. The second term is equivalent to the flow work that could be extracted from expanding the final compressed air product from P_c to P_0 isothermally. With the calculated work input and potential energy stored, the compression efficiency η_c can be defined as:

$$\eta_c = \frac{E_P}{W_{in}} = \frac{P_0 V_0 \left[\ln(r) + \frac{1}{r} - 1\right] + (P_c - P_0)V_{iso}}{\int_{v_0}^{v_c}(P_c(t) - P_0)dV + \left(1 - \frac{1}{r}\right)(P_c V_C - P_0 V_0) + (P_c - P_0)V_s} \quad (2.5)$$

As the compression trajectory ζ_c, approaches the isothermal trajectory, the area shaded by vertical lines gets closer in magnitude to the area shaded by the horizontal lines, and the compression efficiency increases. As ζ_c gets closer to the adiabatic trajectory, the difference between those two areas becomes larger and efficiency decreases. For a compression process with an initial pressure $P_0 = 1\,\text{atm}$, and a compression ratio of r=10, the efficiency of an adiabatic compression process is slightly above 70%.

The efficiency of a compression process not only depends on the compression ratio but is also dependent on the compression time. As compression time gets longer, allowing for more heat transfer, the compression efficiency increases. However, the longer the compression time is under the same compression ratio, the smaller the compression power. In this study, power density, ρ_c, is introduced to evaluate how fast the liquid piston compression can store energy using a given volume. The power density ρ_c is defined as the total stored energy, E_P, divided by the product of total compression time t_c and volume of the compression chamber V_0:

$$\rho_c = \frac{E_P}{t_c V_0} \quad (2.6)$$

In this study, the efficiencies of compression processes with and without porous insert at different power densities are evaluated and compared.

During the regeneration phase, the stored compressed air can be isobarically discharged out of the storage tank and then expanded through a liquid piston expansion chamber. For an expansion process starting at an initial state of T_0, P_c, V_0, the initial air product is ejected from the open-accumulator isobarically and expanded inside a liquid piston chamber through an expansion trajectory $\zeta_e\big(P(t), V(t)\big)$, to a final state of T_e, P_e, V_e with an expansion ratio $r = \frac{P_c}{P_e}$, as shown in figure 2.6. The actual flow work output W_{out} associated with the expansion trajectory $\zeta_e(t)$ can be calculated as:

$$W_{out} = \int_{v_0}^{v_e} (P(t) - P_{atm})dV + (P_c - P_{atm})V_0 \tag{2.7}$$

This expression of work output can be treated as two terms. The first term is the flow work extracted through trajectory ζ_e, shown as the area shaded by horizontal lines under ζ_e. The second term is the motoring work of the initial air product being discharged from the open-accumulator. This is shown as the area shaded by horizontal lines and bounded by isobaric line, P_c, P_{atm} and isochoric line V_0. The stored potential work output E_P is shown as the area shaded by horizontal lines and can be calculated as:

$$E_P = P_c V_0[\ln(r)] - [P_{atm}(V_{iso} - V_0)] + (P_c - P_{atm})V_0 \tag{2.8}$$

Where the first two terms represent the expansion flow work output of expanding the compressed air product from P_c to P_e isothermally and the third term is the ejection work output of discharging the compressed air product isobarically from the open accumulator.

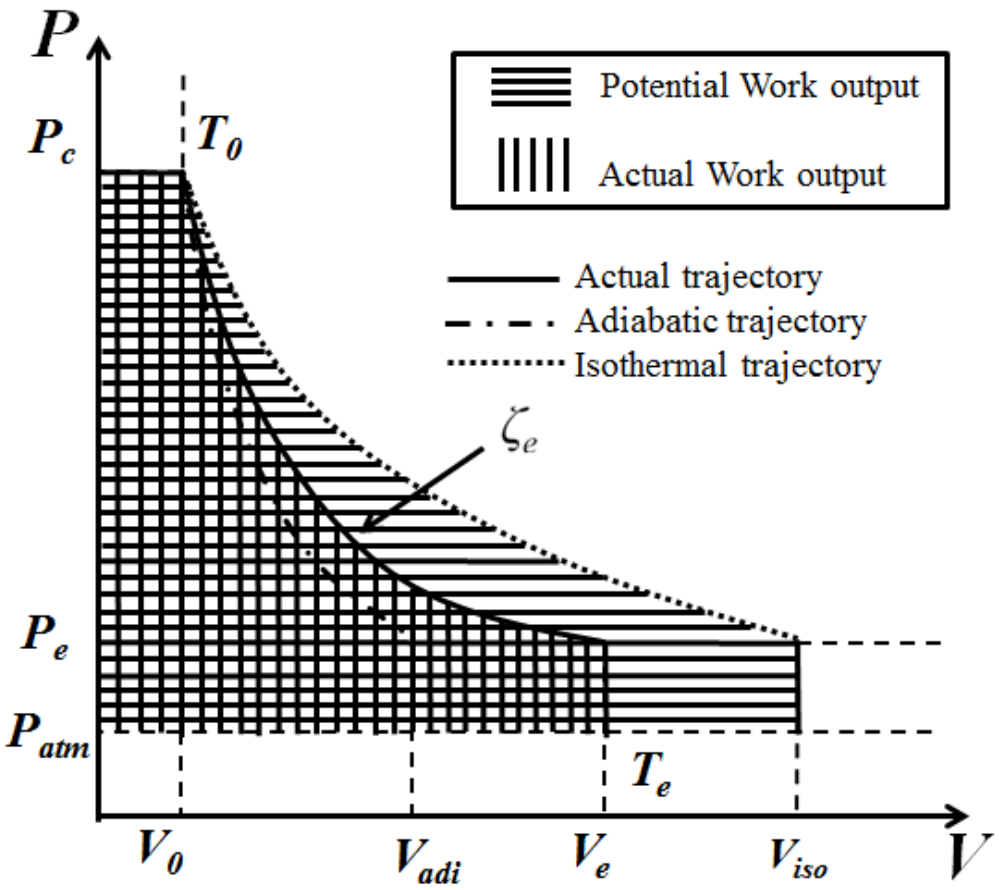

Figure 2.6: P-V curve showing expansion trajectory ζ_e for a liquid piston within an open-accumulator system. The area shaded by horizontal lines represents the potential work output available to eject the initial air product from accumulator isobarically and expand it isothermally from P_c to P_e. The actual work output from ζ_e is the shared area by vertical lines

The expansion efficiency η_e is defined as the total amount of flow work output during ejection and expansion of the air divided by the total amount of potential energy E_P:

$$\eta_e = \frac{W_{out}}{E_P} = \frac{\int_{v_0}^{v_e}(P(t) - P_{atm})dV + (P_c - P_{atm})V_0}{P_c V_0[\ln(r)] - [P_{atm}(V_{iso} - V_0)] + (P_c - P_{atm})V_0} \tag{2.9}$$

Similar to the compression process, the expansion power density ρ_e can be used to evaluate how fast the flow work can be extracted through a fixed volume expansion

chamber. It can be expressed as the total work output, W_{out}, divided by the product of expansion time t_e and the volume of the expansion chamber, V_E:

$$\rho_e = \frac{W_{out}}{t_e V_E} \tag{2.10}$$

For an expansion process with an initial pressure $P_0 = 10\ atm$, and an expansion ratio r=6, the efficiency of an adiabatic compression process is also slightly above 70%. For a complete compression expansion cycle in an Open-Accumulator system using the parameters given above, the minimum compression/expansion thermodynamic cycle efficiency is only about 50%. The poor thermodynamic efficiency would make the open accumulator CAES economically unattractive considering other loss hasn't been considered yet. However, the compression/expansion efficiency can be dramatically increased up to 96% under the same conditions with the help of porous inserts. This would significantly increase the economic feasibility of the open accumulator CAES system.

2.3 Governing Equations

The liquid piston compression and expansion process can be treated as an *air-surrounding heat sink system* described by the first law of thermodynamics. Equation 2.17 can be used to describe the compression process and equation 2.18 can be used to describe the expansion process.

$$dU_{air} = PdV_{work\ input} - \delta Q_{air\ to\ sink} \tag{2.11}$$

$$dU_{air} = \delta Q_{source\ to\ air} - PdV_{work\ output} \tag{2.12}$$

where dU_{air} is the change of internal energy of the air, δQ is the infinitesimal heat transfer between air and heat sink/source and PdV is an infinitesimal amount of work done by or on the air. In order to solve these differential equations, a general function (2.5) that relates air pressure, temperature, and volume is necessary.

$$\mathrm{f}(P, T, V) = 0 \tag{2.13}$$

In this section, appropriate assumptions will be listed to simply these equations into convenient forms.

2.3.1 Assumptions:

- Ideal dry air

The air inside the compression/expansion chamber is assumed to be ideal gas and can be described by equation 2.6:

$$PV = nRT \tag{2.14}$$

where P is absolute pressure, V is air volume, n is the amount of substance of the gas in moles, R is universal gas constant. This assumption is widely accepted for air at near-standard-atmosphere conditions and provides a necessary equation of state. However, when air temperature and pressure increases, air no longer strictly follows this correlation. For this study, air pressure and temperature changes drastically during the compression and expansion processes. Whether it is appropriate to use this assumption is questionable. The compressibility factor, Z, is used to evaluate the effectiveness of ideal gas assumption:

$$Z = \frac{PV}{mRT} \tag{2.15}$$

When Z equals one, the air is expected to behave as an ideal gas. The estimated temperature and pressure range of the air for this study and the associated experimentally determined Z is shown in Table 2.1:

Temp in K	P=1.0 bar	P=5.0 bar	P=10.0 bar	P=100.0 bar	P=200.0 bar	P=300.0 bar
T=250K	0.9992	0.9957	0.9911	0.9411	0.8549	1.0702
T=300K	0.9999	0.9987	0.9974	0.993	0.9713	1.1089
T=350K	1.0000	1.0002	1.0004	1.0183	1.0326	1.1303
T=400K	1.0002	1.0012	1.0025	1.0312	1.0635	1.1411
T=450K	1.0003	1.0016	1.0034	1.0374	1.0795	1.1463
T=500K	1.0003	1.002	1.0034	1.041	1.0913	1.1463

Table2.1. Detailed experimental values for Z at estimated pressure and temperature [42]

Since the pressure range for this study is roughly from 1 bar to 10 bar. From the table, the worst case deviation is only 0.89% when pressure is 10 bar and temperature is 250K. However, the experiments from this study never reach this state. The worst case during the rapid expansion is a temperature around 250 K and pressure around 5 bar, which leads to a deviation of 0.43%. Although the deviation could become more than 10% at high pressure region (higher than 200bar) the minor deviation is insignificant to the overall calculation of this study. Therefore, the ideal gas assumption is appropriate. Furthermore, the internal energy of an ideal gas can be described solely as a function of temperature:

$$du = nc_v dT \tag{2.16}$$

where: du is change in internal energy of the air, n is the quantity of air in moles, c_v is the specific heat of dry air at constant volume = 0.718 kJ/kg*K, dT is the change in bulk temperature of the air. This leads to another major assumption of the study.

- Uniform air temperature

In reality, the air temperature inside the liquid piston chamber during a compression process is not spatially uniform. Both thermocouple measurements [21] and simulation results [43] by Rice and Zhang on a similar system show that there is strong temperature gradient within the air during the compression process. However, it is an extremely difficult task to obtain an accurate real time air temperature field during the rapid compression/expansion process. This would require hundreds of finite thermocouples for measurements, previous studies by Rice [21] shows that the phases lag in thermocouple measurements is too big to capture the accurate peak temperature during the rapid compression even with a very thin Type-K thermocouple. Conventionally, the modeling of internal combustion engine tends to treat the in-cylinder temperature as a single bulk temperature [44]. Consider the substantial simplification of the problem offered by this assumption, and that the focus of this study is on the macroscopic behavior of the air in the chamber, it is appropriate to make this assumption for this thesis. However, the author is aware that temperature of air near the wall would be lower than the temperature near the core of the chamber during compression and vice versa during expansion.

- Isothermal inserts and chamber wall

The inserts used in this study include two types of interrupted plates made of ABS plastic, and two types of metal foams made of aluminum. Detailed information about all the inserts is given in Chapter 3. The temperature of the inserts used in this study is assumed to be uniform throughout the whole compression/expansion process. A back of the envelope estimation is performed to estimate the largest temperature change in the inserts under worst case scenario. The highest amount of heat transfer from the air to its

surroundings among all the experiments performed in this study is about 120 J, if all that energy transfer into a 5mm interrupted plates made by ABS plastic which has an mC_v product equal to 150J/K, the lowest among all inserts, the total change in temperature of that insert is less than 1 K. This is a very simplified approximation. In reality the bulk temperature change in the insert would be much lower than 1K since a big portion of the heat is absorbed by water. In addition, the Biot number is used to compare the thermal resistance at the surface of the insert to the thermal resistance inside the insert body:

$$Bi = \frac{hL_c}{k_b} \tag{2.17}$$

where: h is heat transfer coefficient, L_c is the characteristic length of the insert, and k_b is thermal conductivity of insert. L_c is commonly defined as the volume per surface area:

$$L_c = \frac{V_{body}}{A_{surface}} \tag{2.18}$$

It is widely accepted that when $Bi < 0.1$ the solid can be assumed to have a uniform temperature distribution [45]. The following table shows the required critical heat transfer coefficient h to satisfy a Biot number equal to 0.1 (to satisfy this requirement, h must be lower than the calculated critical values)

Table 2.2: Detailed Biot number calculation for all inserts

	Bi	L_c (m)	k_b(W/m-K)	Critical h (W/m^2-K)
2.5mm interrupted plate	0.1	0.00038	0.179	35.8
5.0mm interrupted plate	0.1	0.0005	0.179	35.8
10ppi metal foam	0.1	0.1408	250	177.6
40ppi metal foam	0.1	0.00578	250	4325.3

The estimated h for interrupted plates from 10 to 30 W/m^2-K and the estimated h for metal foams is below 20 W/m^2-K from experimental data, The Biot number for all the

experiments never reaches 0.1, so the lumped temperature assumption is appropriate for all inserts.

Meanwhile, the outer surface of the wall is exposed to ambient air and the inner surface is subject to heated air during compression and cooled air during expansion. The wall is made out of polycarbonate tube with a wall thickness of 0.32cm (1/8 inch), a length of 30cm and thermal conductivity of 0.175W/m-K. The characteristic length for the cylinder wall, L_c, is estimated to be 0.4 cm. Similar to inserts, the critical heat transfer coefficient, h, is equal to $\frac{Bi\, K_b}{L_C} = 4.375 \frac{W}{m^2 K}$. Unfortunately, in most experiments done in this study, the actual h is higher than the critical h, so it seems there is a temperature gradient within in the wall. However, a back of the envelop estimation shows that the mC_v product of the wall is about 385J/K, under the worst scenario, the total temperature change in the wall would be less than 0.3K. Since a complete modeling on the temperature distribution in the chamber wall and insert requires coupling addition partial differential equation causing it to be beyond the scope of this thesis. Thus, the wall, porous inserts and liquid air interface are all assumed to be isothermal. With this assumption, the bounding surface of the air inside the chamber becomes an infinite thermal capacity heat sink during compression and an infinite thermal capacity heat source during expansion.

- Ignore viscous, leakage loss and gravity work

A complete force balance on the system includes liquid piston pressure force on the air, viscous shear force on the wall and inserts, and gravity force of the air. During the compression of the air, the liquid piston does work on the air and during the expansion process, air does work on the piston, both processes are subjected viscous shear and

gravity forces. In order to simply the problem, only PV flow work is considered in this study. To support this assumption, a-back-of-the-envelope calculation is performed to estimate the order of magnitude of the all the work terms. PV work, is estimated to be around $(4x10^5 Pa)*(4x10^{-4}m^3)$ =160 J. For viscous shear work, the largest pressure drop occurs with the fastest compression experiments using 40ppi metal foam insert, the experimentally acquired pressure drop information for the same metal foams used in this study generated by Zhang et al, shown in figure 2.7 [46]:

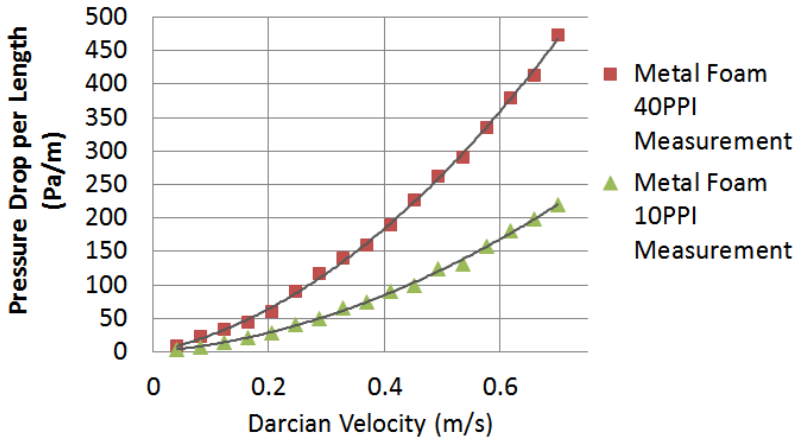

Fig.2.7. Pressure drop per length of metal foam vs. Darcian velocity (adapted from [46])

The fastest speed of air during compression/expansion is around 0.2m/s and the associated pressure drop per length is 60 Pa/m. The total length of the metal foam is 0.3 m and the total volume of air passing through the foam is about $5x10^{-4}$ m^3. The corresponding viscos loss due to pressure drop can be estimated as : $(60Pa/m)*(0.3m)*(5x10^{-4} m^3)=9x10^{-3}J$. The work done to overcome the air gravity can be estimated as: $(5x10^{-4}m^3)*(1.05kg/m^3)$ $*(9.8m/s^2)$ $*(0.3m)$ = $1.5x10^{-3}$ J. For simplification, only PV work should be considered as work input.

- Ignore leakage loss

Leakage could be a problem for a conventional piston compressor operating at a high pressure where, the design trade-off between gas leakage and high sealing friction remains a major technical challenge. For liquid piston compressors, the leakage through liquid piston is eliminated. Although, there is a static O-ring seal at the top cap, there is no sign of leaking been found during all experiments. Thus ignoring leakage loss is acceptable.

- Ignore solubility of air in water

Given the fact that liquid piston is used to compress and expand air in this study, the effects of solubility of air in water may affect the overall performance of the processes. A simple estimation of the mass ratio of air that could be dissolved in the water is performed in the following paragraphs.

The solubility of a gas in a liquid is governed by Henry's Law: "At a constant temperature, the amount of given gas that dissolves in a given type and volume of liquid is directly proportional to the partial pressure of that gas in equilibrium with that liquid." [47]:

$$p = k_H c \tag{2.19}$$

where: p is the partial pressure (atm) of the gas above the liquid, c is the concentration of the solution (mol/L) and k_H is a temperature dependent constant, with dimensions of $\frac{L.atm}{mol}$. The following analysis shows estimation of how much air could be dissolved in the liquid piston after a compression process and air is cooled to reach thermal equilibrium. For simplicity, ignoring all the inert gas in the air and assuming the air inside the chamber is solely composed by 21 % oxygen and 79% Nitrogen volume wise. The Henry constant for oxygen and nitrogen that can be dissolved in water at 298K is

769.2 $\frac{L.atm}{mol}$ and 1639.34 $\frac{L.atm}{mol}$ [48]. The size of the compression chamber is roughly 700 cc. Initially, the compression chamber is filled with air at STP and there is no water, at the final state, air is assumed to be maintained at 70cc and 10bar. Table 2.3 shows the detailed results on partial pressure, solubility, and ratio of gas dissolved before and after compression at equilibrium (assuming at the end state, additional air is supplied into the top plenum to maintain the pressure):

Table 2.3: Detailed analysis results on the change of dissolved gas after a compression process.

	Before	after	before	after
Gas at equilibrium	N_2	N_2	O_2	O_2
Partial pressure (atm)	0.79	7.90	0.21	2.10
K ($L.atm/mol$)	1.64E+03	1.64E+03	7.69E+02	7.69E+02
C(mol/L)	4.82E-04	4.82E-03	2.73E-04	2.73E-03
Water mass (g)	0.00	500.00	0.00	500.00
Solubility (g/L)	1.35E-02	1.35E-01	8.74E-03	8.74E-02
Mass dissolved (g)	0.00E+00	6.75E-02	0.00E+00	4.37E-02
Mass of gas (g)	6.34E-01	5.66E-01	1.92E-01	1.49E-01
Dissolved gas %	0	10.65%	0	22.71%

From this crude analysis, there is 10.65% nitrogen and 22.7% of oxygen can be dissolved into the liquid piston once final air product reaches equilibrium. It seems it's not appropriate to ignore the solubility effect. Fortunately, this analysis requires the final gas concentration reaches equilibrium. The diffusion process of oxygen and nitrogen into water is an extremely slow process, since the mass diffusion coefficient of oxygen and nitrogen into water at 1atm when water is 25C is 2.0E-6 cm2/s [49] and 1.88E-6 cm^2/s [50]. It takes an order of magnitude of 10^5 seconds (27.8 hours) for the final gas product to reach equilibrium. Since a complete model on gas solubility requires coupling another set of mass diffusion equations make it out of the scope of this study and most of our

experiments completed within seconds. It is reasonable to ignore this effect and focus on the thermal dynamic side of the problem.

- Newton's Law of Cooling

The primary heat transfer mode in the system described above is convection. Newton's law of cooling is used to describe the overall effect of convection:

$$q_{air\ to\ sink} = hA(T - T_{sink}) \tag{2.20}$$

$$q_{source\ to\ air} = hA(T_{source} - T) \tag{2.21}$$

where equation 2.37 is used to describe compression process and 2.38 is used to describe expansion process., q is the heat transfer rate between air and heat sink (or source), h is the heat transfer coefficient between air and its surroundings, A is available heat transfer surface area, T is the temperature of air and $T_{sink}$is the temperature of the heat sink (or source). In this study, the bounding surface of the air inside the chamber is assumed to be an infinite thermal capacity heat sink (or source) at room temperature. Using this and all the other assumptions listed before, equation 2.17 and 2.18 can be simplified to:

$$m_{air}c_v\dot{T} = P\dot{V} - hA(T - T_{sink}) \tag{2.22}$$

$$m_{air}c_v\dot{T} = hA(T_{source} - T) - P\dot{V} \tag{2.23}$$

$$PV = m_{air}R_{air}T \tag{2.24}$$

Where equation 2.39 describes the energy balance for a compression process and equation 2.40 describes the energy balance for an expansion process, equation 2.41 describes the temperature relation with pressure and volume for both processes. m_{air} is the mass of the air inside the chamber, R_{air} is gas constant for air, c_v specific heat for dry air, $T_{sink} = T_{sourece}$ = room temperature, T is bulk temperature of air, P and V are pressure and volume of air inside the compression/expansion chamber. In this study, P

and V are measured by experimental apparatus, and T can be calculated using ideal gas law equation once pressure and volume profile is known.

2.4 Modeling of heat transfer

Under the assumptions listed above, and using equation 2.40, 2.41, the instantaneous heat transfer coefficient h can be described as for compression processes:

$$h = \frac{P\dot{V} - m_{air}c_v\dot{T}}{A(T - T_{sink})} \tag{2.25}$$

For expansion processes:

$$h = \frac{P\dot{V} + m_{air}c_v\dot{T}}{A(T_{source} - T)} \tag{2.26}$$

where P, V, T, c_v, m_{air}, T_{source}, and T_{sink}, can be measured or calculated. However, heat transfer surface area, A, remains unknown and it is significantly different in cases with or without porous inserts and during the compression/expansion processes at different liquid piston heights.Modeling of the cases with inserts and cases without inserts should be separated. In addition, the position of the inserts inside the chamber is different during compression and expansion process, different strategies on modeling the surfaces area for compression and expansion should also be utilized.

2.4.1 Compression/expansion with empty chamber

For compression/expansion cases without porous insert, A includes instantaneous cylinder wall area, A_{wall}, top cap area $\frac{\pi D^2}{4}$ and base liquid piston area $\frac{\pi D^2}{4}$, for a given geometry of the chamber with a volume of $V_0 = 715\ cc$, an inner diameter of D=5.08cm and length total length L=35cm. Depending on the height of the air column, the instantaneous wall surface area can be estimated as:

$$A_{wall} = \frac{4V}{D} \tag{2.27}$$

where V is volume of air inside the chamber. The heat transfer surface area can be expressed as:

$$A = \frac{4V}{D} + \frac{\pi D^2}{2} \tag{2.28}$$

2.4.2 Compression with porous inserts

For compression case with porous inserts, A has to include the extra surface area introduced by the porous material. Given the fact that the metal foam used in this study has some inconsistency of the pore size and the interrupted plates has little fine ridges on the surface, it is impossible to get an accurate measurement in the surface area. Specific surface area S (m^2/m^3) from manufacturing design specifications is used to approximate the surface area introduced from the porous inserts:

$$A_{insert} = S * V_P \tag{2.29}$$

where A_{insert} is the heat transfer surface area introduced from porous insert, S is the designed specific surface area of the insert, detailed S values is shown in table 3.1. V_P is the volume of the inserts that is participating heat transfer with air. All the inserts used in this study is cylindrical shape with a diameter of 5cm. For all the compression tests, the total length of the inserts is about 30cm and the chamber is 35cm long. All inserts were pushed all the way up to the top cap, creating a 5cm long, $101cm^3$ cylindrical plenum between the bottom of the insert and the base of the chamber. Once the compression process starts, V_P decreases as the more water gets into the chamber after the water filled

up the 101 cm^3 plenum. Thus, V_P is function of the liquid volume V_l that enter the chamber and the porosity $\emptyset$ of the inserts:

$$V_P = 589\ cm^3 \quad for\ V_l \leq 101 cm^3 \tag{2.30}$$

$$V_P = \left[589 - \frac{(V_l - 101)}{\emptyset}\right] \quad for\ V_l \geq 101 cm^3 \tag{2.31}$$

The total amount of heat transfer area A for cases with porous inserts including the empty chamber surface area can be calculated as:

$$A = \frac{4V}{D} + \frac{\pi D^2}{2} + S * 589\ cm^3 \quad for\ V_l \leq 101 cm^3 \tag{2.32}$$

$$A = \frac{4V}{D} + \frac{\pi D^2}{2} + S * \left[589 - \frac{(V_l - 101)}{\emptyset}\right] \quad for\ V_l \geq 101 cm^3 \tag{2.33}$$

2.4.3 Expansion with porous inserts

During the expansion experiments with porous inserts, the inserts are pushed all the way to the bottom of the chamber thus creating a 5cm long and 101cm^3 size plenum at the top of the chamber. The inserts are initially submerged under the water, the volume of the inserts that participates in heat transfer is zero at beginning and gradually increases as the liquid expands out of the chamber. Thus, V_P during expansion can be expressed as function of the porosity, $\emptyset$, of the inserts and liquid volume V_l that exits the chamber:

$$V_P = \frac{V_l}{\emptyset} \tag{2.34}$$

The total amount of heat transfer area A for expansion experiments with porous inserts including the chamber surface area can be calculated as:

$$A = \frac{4V}{D} + \frac{\pi D^2}{2} + S * \frac{V_l}{\emptyset} \tag{2.35}$$

2.4.4 hA product

Using equations 2.28, 2.32, 2.33 and 2.35, and plugging them back to equations 2.25, 2.26, he heat transfer coefficient can be calculated. However, due to the large uncertainties in heat transfer area estimation and temperature calculation, there will be significant amount of uncertainty in *h*. Since the focus of this thesis is to study the overall bulk behavior of the gas, it would be wise to evaluate *hA* product together rather than *h* and *A* separately. Therefore, equation 2.25 and 2.26 can be converted into:

$$hA = \frac{P\dot{V} - m_{air}c_v\dot{T}}{(T - T_{sink})} \tag{2.36}$$

$$hA = \frac{P\dot{V} + m_{air}c_v\dot{T}}{(T_{source} - T)} \tag{2.37}$$

For compression processes averaged hA_{avg} product can be defined as:

$$hA_{avg} = \frac{\int_{V_0}^{V_f} P\dot{V} - m_{air}c_v\dot{T}dV}{\int_{V_0}^{V_f} T - T_{sink}dV} \tag{2.38}$$

For expansion processes averaged hA_{avg} product can be defined as:

$$hA_{avg} = \frac{\int_{V_0}^{V_f} P\dot{V} + m_{air}c_v\dot{T}dV}{\int_{V_0}^{V_f} T_{source} - TdV} \tag{2.39}$$

Since the amount of heat transfer will determine the efficiency of a compression/expansion process. It would be expected that processes with higher hA_{avg} would have higher efficiencies.

Chapter 3

Compression Experiments

3.1: Experimental setup:

A schematic of the liquid-piston compressor system is shown in figure 3.1. Water is circulated in a counter-clockwise direction.

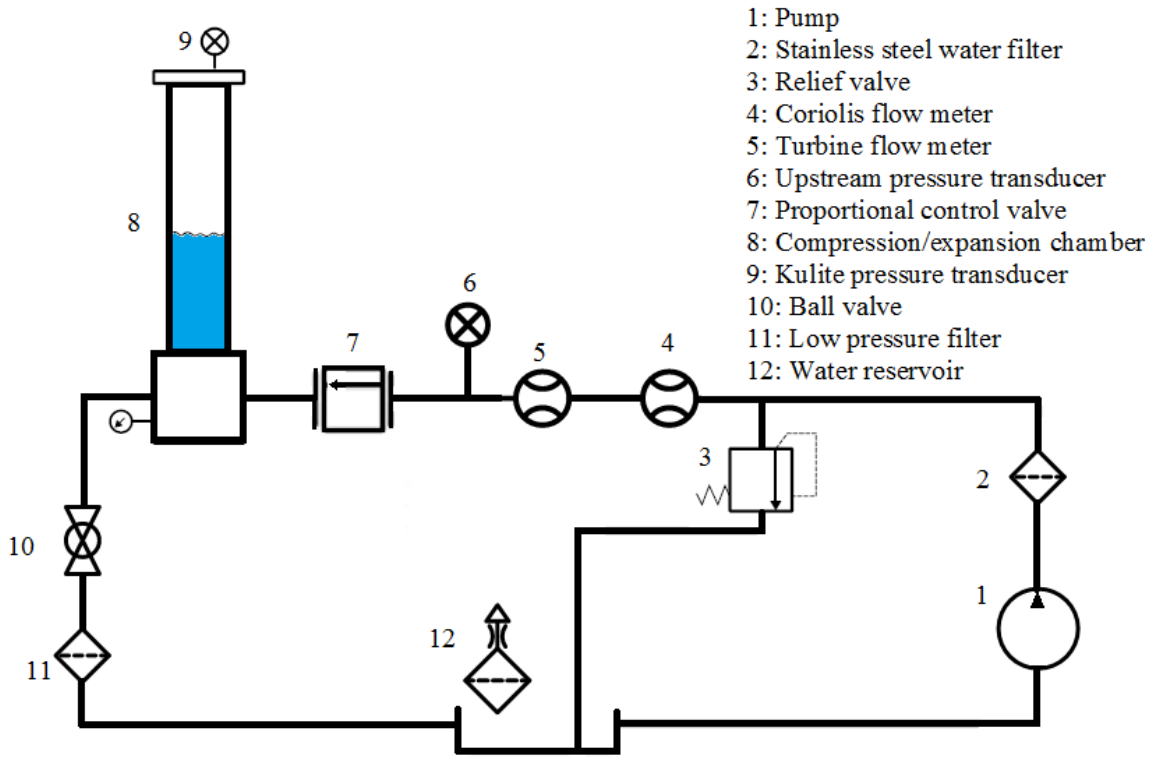

Figure 3.1 Flow loop of the compression experiment setup with labels

The pump used in this study is a D-10-I series Hydra-Cell positive displacement diaphragm pump (1) from Wanner Engineering Inc with a displacement of 117 revs/liter.

The pump is driven by a 1.5 hp Dayton 3N550 electric motor at 1740 rpm to provide the required water flow rate to compress air with a liquid piston inside the compression chamber. In order to remove the rust and impurities from the water, a stainless steel water filter (2) is installed after the exit of the pump. The pump is capable of producing pressures of 69 bar (1000 psi), but the compression chamber is only rated for 13.8 bar (200 psi). Therefore, a Danfoss Power Pack Valve, type VPH 15 E, which houses both a relief valve and a directional control valve (3) is used to regulate and maintain the upstream pressure at approximately 11.4 bar (165 psi). An Endress & Hauser Promass-80 Coriolis flow meter with a measuring ranges of 0-5GPM (later removed due to unavailability) and an Omega FTB-1412 turbine flow meter with a measuring ranges of 0.75-7.5GPM(5) are used to measure the water volume flow rate entering the compressor. The volume of air is computed by subtracting the amount of water that has entered the chamber from the initial volume, assuming that the water is incompressible and the compressor wall is rigid. An Aschroft G17M0142F2300 pressure transducer (6) is used to measure the pressure upstream of the solenoid control valve (7). This pressure is used in a feedback loop to control the solenoid control valve, thus regulating upstream pressure and controlling the flow rate. The control of this valve is done within MATLAB/Simulink using a customized Proportional Integrator (PI) controller. For these experiments, a uniform flow rate was desired; however, due the nature of the control valve, the flow rate is only approximately constant. Downstream of the control valve is the liquid-piston compression chamber (8) that is made of extruded polycarbonate tubing and two blocks of aluminum bolted together by four steel threaded tie-rods. The compression chamber shown in figure 3.2 has a length of 353 mm and an internal

diameter of 50.8 mm. It is marked with graduations so that the water level in the chamber can be read. A Kulite ETM-375 pressure transducer (9) is used to measure the pressure inside the chamber during the compression process. It is mounted on the top cap of the chamber. a After the compression process, a ball valve (10) downstream of the compression chamber is opened and water is expelled through another water filter (11) and into the resevoir. MATLAB/Simulink, in conjunction with xPC Target, is used for data acquisition, control and processing. A 16-bit PCI-DAS1602/16 multifunction analog and digital I/O board is used in the target computer to receive sensor signals and to control the solenoid valve. A sampling frequency of 4 kHz is selected to ensure that high frequency turbine meter signals (up to 1300 Hz) are accurately acquired.

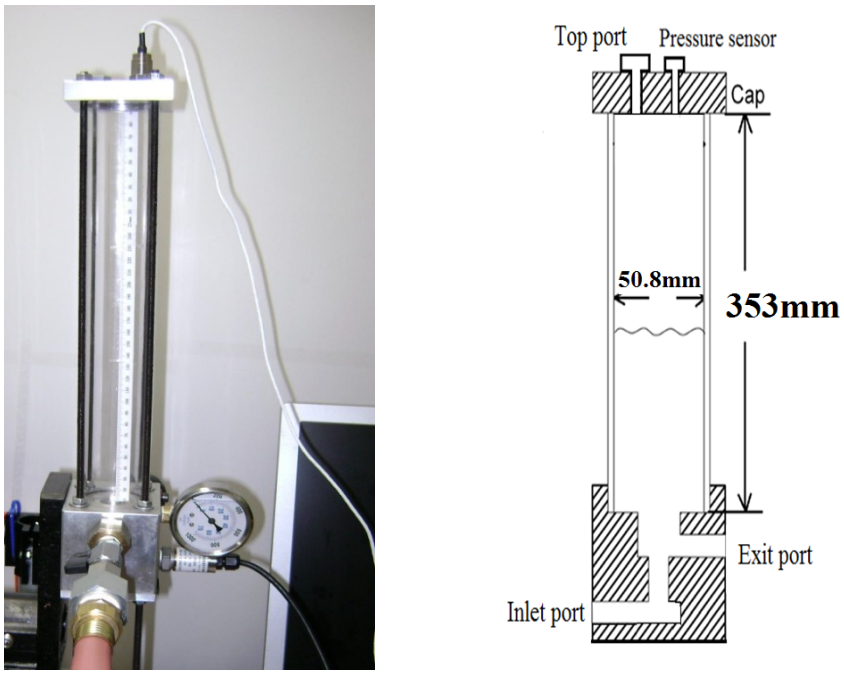

(a) (b)

Figure 3.2(a). : An actual photo of the compression chamber with a pressure sensor mounted on the top cap (b): A cross section sketch view of the compression chamber

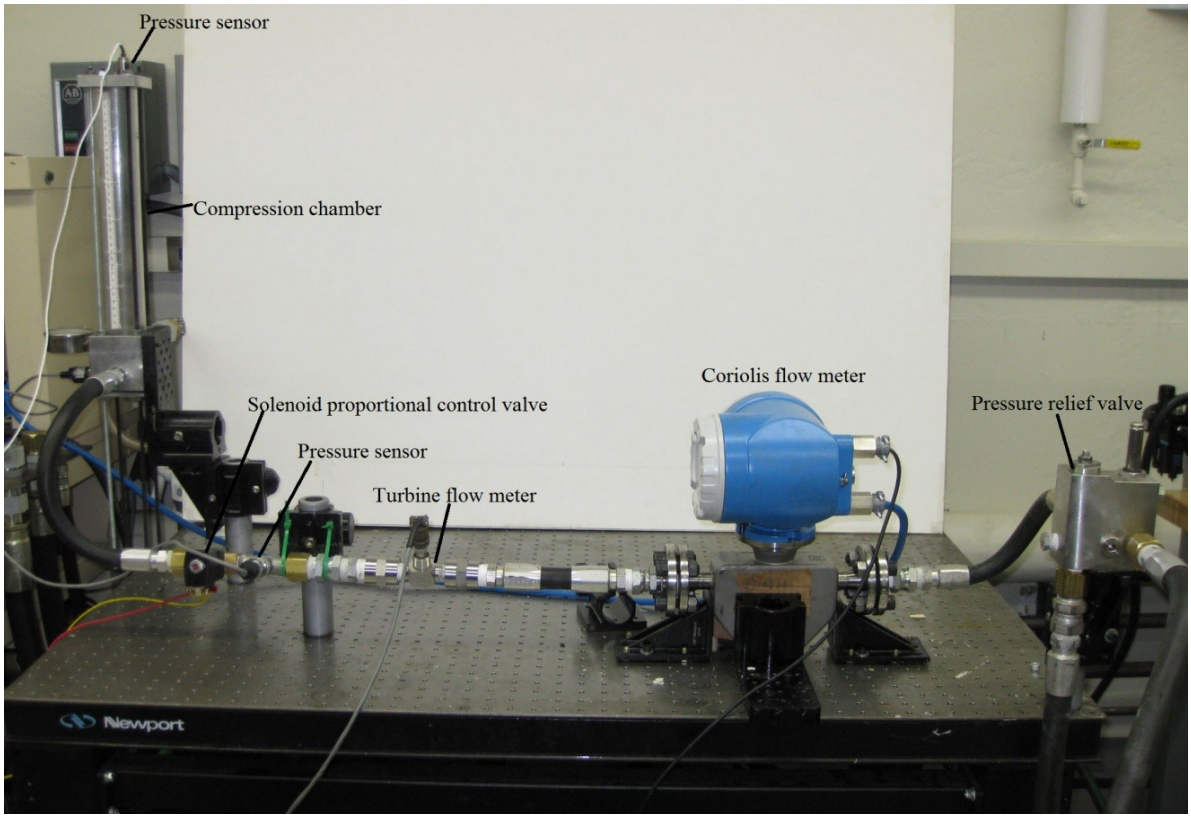

Figure 3.3 A picture of acutal compression experiment setup

3.1.1 Porous Inserts

As means for increasing the efficiency of the compression process, four different porous inserts are studied. Two of the inserts are Duocel® Aluminum metal foam manufactured by ERG [40]. This alluminum foam has a porous structure consisting of an isotropic network of interconnected solid metal struts fabicrated with a porosity of 93% and a high surface area to volume ratio. The two inserts have the same porosity, but different pore sizes, characterized by Pores Per Inch (PPI). The other two inserts are a series of interuppted parallel plates designed by Zhang et al. [41]. As seen in figure3.4, these inserts consist of many layers of parallel plates, each layer rotated 90 degrees from the upstream layer. These inserts are characterized by plate separation distances, 2.5mm

or 5.0 mm. They have charateristics of low density, high surface area to volume ratio and relatively low cost. Detailed insert properties are shown in Table 3.1 During the compression experiments, each insert is stacked to the same length of 30 cm and placed vertically to the top of the chamber as shown in figure 3.5.

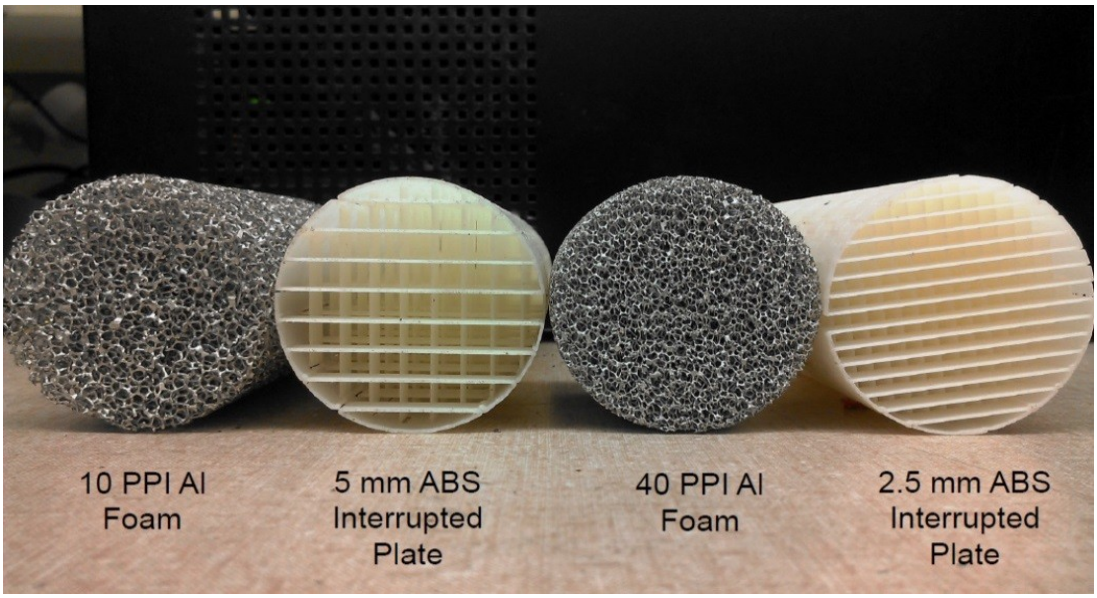

Figure 3.4. A picture of four types of porous inserts that have been tested in this study

Material	Porosity	Density	Type	PPI	Specific area	Conductivity	Specific heat
Aluminum	92-94%	2.7g/cc	Metal foam	40	1730/m	205 W/m-k	0.9 J/g-K
Aluminum	92-94%	2.7g/cc	Metal foam	10	710/m	205 W/m-k	0.9 J/g-K
ABS(plastic)	88%	1.05g/cc	Interrupted plates	4-5	370/m	0.153 W/m-k	1.97J/g-K
ABS(plastic)	81%	1.05g/cc	Interrupted plates	9-10	650/m	0.153 W/m-k	1.97J/g-K

Table 3.1. Detailed properties of the porous inserts used in this study.

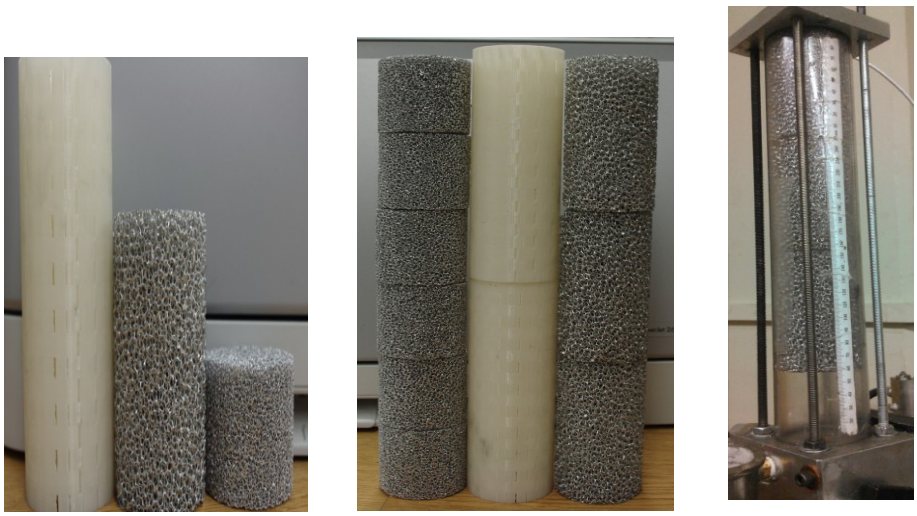

(a) (b) (c)

Figure 3.5. (a):A picture of single elements of the inserts (b):A picture of stacked inserts (c):A picture of Inserts insided chamber

3.2 Test Conditions and Methods

The purpose of the experiments is to quantitatively evaluate the effectiveness of the four different porous inserts used in a liquid compressor and compare these results to the cases without inserts. Initial testing consisted of several baseline tests, without inserts, to acquire the temperature, pressure and volume trajectories as well as compression efficiencies for the process over a range of compression times. Following the baseline compression tests, a series of experiments are performed for each of the four inserts under similar testing conditions. The results are compared in the form of normalized temperature profiles, pressure volume trajectories and efficiency vs. power density curves.

In all the compression experiments, air at ambient temperature is compressed from an initial pressure of one atmosphere to a final pressure slightly above ten atmospheres through a constant volume trajectory.

3.2.1 Compression test procedure

Prior to running a compression test, the pump and lines are flushed of any residual water and primed with fresh water. The water level in the compression chamber is set to a specific level and all valves are closed. Initial air temperature is recorded from a thermometer in the lab and initial pressure is recorded using barometric pressure provided by the department's online barometric pressure server. The initial volume is known since the water is always placed at a set level. Once the real time simulation starts, the control valve is immediately opened. The integrated volume flow rate is used as feedback to determine when to close the control valve. A pre-specified quantity is selected to compress to a compression ratio of slightly larger than 10. Once the desired quantity of liquid is reached, Simulink sends a signal to close the valve. From the measured air pressure and volume, the bulk temperature of the air inside the compression chamber is calculated by modified equation 2.24:

$$T(t) = \frac{1}{m_{air}\, R_{air}} P_{(t)} V_{(t)} \tag{3.1}$$

where the mass of air in the chamber m_{air} can be calculated from the measured initial conditions:

$$m_{air} = \frac{P_0 V_0}{R_{air} T_o} \tag{3.2}$$

where

P_0 is ambient pressure obtained from a barometer

T_o is ambient temperature measured by the thermometer in the lab

V_0 is the inital air volume as measured by a caliper

R is ideal gas constant for dry air $= 287\ \mathrm{J\,kg^{-1}\,K^{-1}}$

$P_{(t)}$ is measured pressure data from the Kulite pressure sensor

$V_{(t)}$ is calculated air volume inside the chamber, using inital air volume subtracted by the liquid volume exited the chamber measured flow meter

T(t) is computed air volume temperature inside the chamber

3.2.2 Data reduction

Prior to data processing, raw data are saved. Data reduction begins by applying a 100 data points (0.025 seconds in real time) moving average on the pressure measurement to remove high frequency noise from the pressure measurement. Air volume is calculated by subtracting the measured volume of liquid that has entered the chamber from initial air volume, V_0. As shown in the uncertainty analysis section, errors in air volume can be reduced by using a correction factor, CF.

$$CF = \frac{V_0 - V_f}{V_T} \tag{3.3}$$

where:

V_0 is the inital air volume as measured by a graduated cylinder

V_f is the final volume after compression

V_T is the total amount of liquid added into the chamber measured by the Turbine meter

The initial air volume is easily determined since the initial water level is consistent and the volume occupied by porous inserts is known; however, there is no direct way to measure the final volume of the air , V_f, because of the presence of the porous inserts. A concept of using the equilibrium pressure when thermal equilibrium is reached is introduced. After compression is completed and the system has come into thermal equilibrium with the ambient air, pressure no longer changes and reaches an

equilibrium pressure, P_{eq},. Since the final equilibrium temperature, T_{eq} is known to be T_o, the ambient temperature, the final air volume can be calculated by the ideal gas law:

$$\frac{T_{eq}}{P_{eq}V_{eq}} = \frac{T_o}{P_0V_0} \tag{3.4}$$

$$V_{eq} = V_f = \frac{T_{eq}}{P_{eq}\frac{T_0}{P_0V_0}} = \frac{\mathrm{P_0V_0}}{\mathrm{P_{eq}}} \tag{3.5}$$

The original cumulative volume as measured by the flowmeter is scaled by this correction factor to get a more accurate air volume measurement. The reasons behind this method are explained in the uncertainty analysis section. For consistency, all of the data is processed to the pressure ratio of 10 using the 100 data point (0.025s) moving averaged pressure measurement, corrected volume trajectory using the correction factor, CF, and calculated temperature profile using equation 3.1. The work input W_{in}, stored energy, E_p, and efficiency η_c are calculated using equations 2.3, 2.4, 2.5 developed in chapter 2 and when integration is necessary, MATLAB's built-in trapezoidal numerical integration function is utilized.

3.3 Uncertainty analysis

For the compression experiments five different cases are considered: a baseline case without inserts and four cases corresponding to the four different inserts. For the baseline case the initial air volume, V_0, is 715 cm^3 with an uncertainty of ± 2 cm^3. For the insert cases the initial volumes for the 2.5mm, 5mm, 10PPI, and 40PPI inserts are 608 cm^3, 645 cm^3, 670 cm^3, and 670 cm^3 respectively, each with an uncertainty of ± 2.8 cm^3. These uncertainties are expressed in percent in table 3.2. Pressure is measured with a Kulite ETM-375 pressure transducer. The typical uncertainty for this instrument is 0.1%

of full scale. Flow is measured with an Omega FTB-1412 turbine flow-meter. This instrument has a stated accuracy of ± 1% of reading in the upper 70% of measuring range. However, by accounting for the slightly non-linear behavior of the flow-meter using the manufacturer's calibration sheet, this accuracy can be improved to ± 0.6% of reading within the upper 70% of the measuring range. The volume of air is found by subtracting the amount of water, V_T, that has been added to the chamber from the initial air volume V_0. To better explain why the correction factor, CF, is used, considering the baseline case, neglecting the error in initial volume and assuming that the air is compressed isothermally from 715 cm^3 to 71.5 cm^3. The percent error in initial volume is 0.28% and the percent error in final air volume is 5.4% if the turbine meter alone is used without any correction. There is a 0.6% error in the 643.5 cm^3 volume of water that is added to the chamber. This error is reduced by using the correction factor based on equilibrium temperature and final pressure as previously described. Using the method proposed by Kline and McClintock [51] the percent uncertainty in V_{eq} is found to be 1.81% as opposed to 5.4% when the turbine meter alone is used. Because of the volume trajectory and final volume is a function of compression efficiency, the uncertainty for V_{eq} is also trajectory dependent. In Table 3.2 the uncertainties for V_{eq} are calculated for the ideal cases with isothermal trajectory as well as the worst scenarios with adiabatic trajectories.

After correcting with CF, the percent error in air volume is assumed to vary linearly from the initial volume to the final volume. Armed with this information a numerical sensitivity analysis is carried out in MATLAB. For each trajectory the percent error in work input is calculated, accounting only for the error in volume. This is

justifiable since the errors in volume are more significant that the errors in pressure and the pressure error is considered to be stochastic, thus integrating out. The results for each insert and trajectory are shown in Table 3.2. After obtaining an expression for the uncertainty in work input, the uncertainty in efficiency is found by again using the method proposed by Kline and McClintock.

Table 3.2: detailed uncertainty analysis results for compression experiments with different inserts.

	Baseline	**2.5 mm**	**5.0 mm**	**10 ppi**	**40 ppi**
V0 in cm^3	715	608	645	670	670
% Error in V0	0.28%	0.46%	0.43%	0.42%	0.42%
% Error in V_{eq} (Isothermal Trajectory)	1.81%	1.85%	1.84%	1.84%	1.84%
% Error in V_{eq} (Adiabatic Trajectory)	1.90%	1.94%	1.93%	1.93%	1.93%
% Error in Work Input (Isothermal Trajectory)	0.98%	1.27%	1.21%	1.19%	1.19%
Error in Efficiency (Isothermal Trajectory)	2.08%	2.20%	2.17%	2.15%	2.15%
%Error in Work Input (Adiabatic Trajectory)	1.00%	1.26%	1.23%	1.20%	1.20%
Error in Efficiency (Adiabatic Trajectory)	1.45%	1.57%	1.55%	1.54%	1.54%

For the baseline case the uncertainty in efficiency ranges from ± 1.45% for adiabatic process to ± 2.08% for isothermal process. Since the average efficiency for the no insert cases is about 82%, the average uncertainty in efficiency is ±1.5% by interpolating between adiabatic (70.7%) and isothermal (100%) efficiencies. The actual uncertainty for each case is calculated using the same interpolation method. For all insert cases the uncertainty in efficiency ranges between ±1.54% to ± 2.2%. For typical experimental efficiencies, the uncertainty becomes ±1.7%.

Chapter 4

Expansion Experiments

4.1: Expansion experimental setup:

During the regeneration stage of a CAES system, high pressure compressed air is expanded through the liquid piston and pushes liquid through a motor to generate electricity. The purpose of the expansion experiment setup is to simulate this expansion process and characterize the gain in efficiency of using various porous inserts at different power densities. A schematic of the experimental setup is shown in figure 4.1.

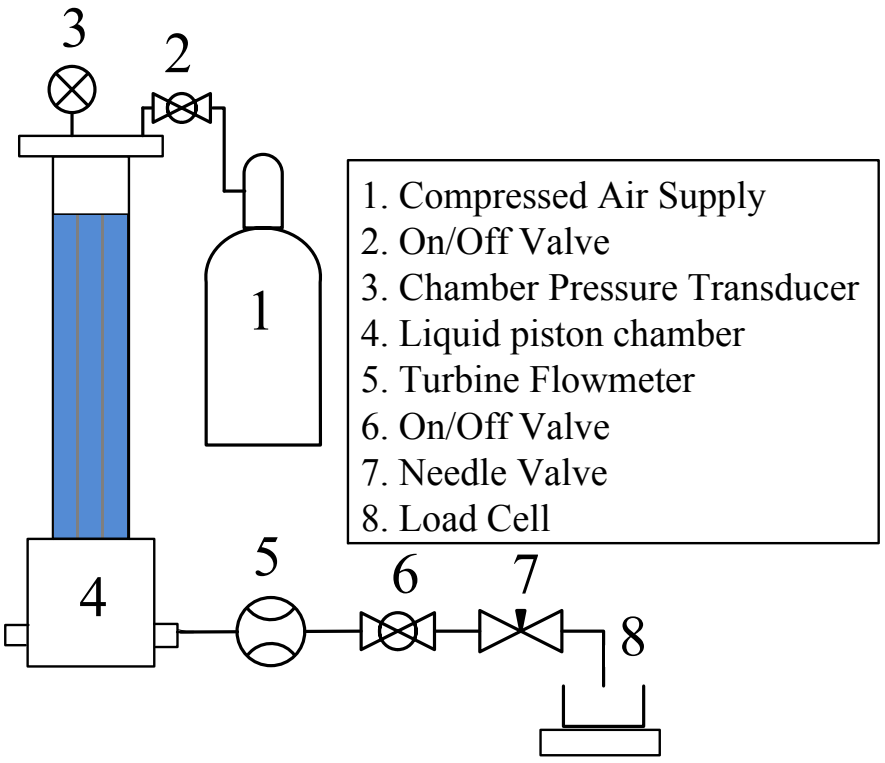

Figure 4.1 Flow loop of the expansion experimental setup and labels on each component

A pressure regulated compressed air tank (1) is used as high pressure air source to provide the initial pressurized air. For safety concern, the pressure regulator on the tank is set at 12.5bar (182psi). An on/off ball valve (2) is placed on top of the expansion chamber (4) to block the air flow from the pressurized tank during the expansion. The expansion chamber is the same chamber as used in the compression experiments. A Kulite ET-375 pressure transducer (3) is used to measure the pressure change in the chamber during the expansion process. An Omega FTB-1412 turbine flow-meter (5) is located in the discharge liquid line downstream of the chamber. It is connected by a 12 inch long straight stainless steel pipe (L/D ratio of 24) placed horizontally to prepare the liquid for entering the turbine meter. Another ball valve (6) is installed after the turbine meter, followed by a needle valve (7) that is used to control the flow rate of the liquid discharging from the chamber. Downstream of the needle valve, water passes through a 1.2m (4 foot) long plastic tube to a water reservoir sitting on a custom-made weigh scale which is built around a Transducer Techniques MLP-50 load cell (8). Mass of the water $m(t)$ exiting the chamber is measured and converted into volume of liquid $V(t)$ assuming constant water density. Pressure and volume signals are collected by the same DAQ system for the compression test. The actual setup of the expansion system is shown in figure 4.2.

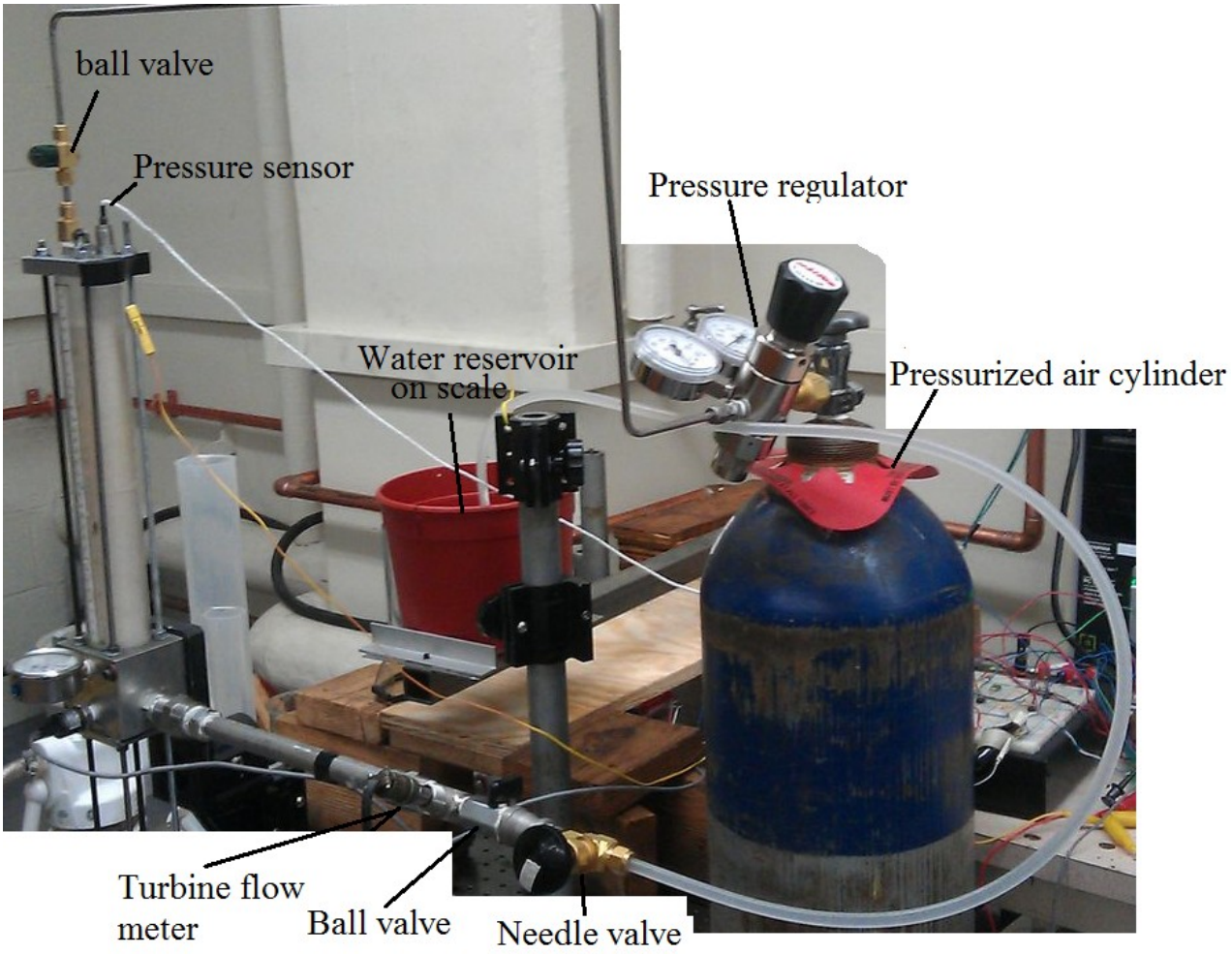

Figure 4.2: A picture of actual expansion experimental setup

4.2 Test Conditions and Methods

The objective of the expansion experiments is to compare the expansion efficiency without inserts to cases with interrupted plate inserts. Extensive initial testing is done with the four inserts mentioned at Chapter 3. After working with metal foams, the authors feel that only interrupted plates are worth further investigation in expansion experiments due to the large amount of water holdup in the metal foams. The 40 PPI aluminum metal foam traps water up to 90% of its own volume. The 10PPI traps water up to 60% of its own volume. On the other hand, the 5mm interrupted plate traps only 5%

of its own volume, and 2.5mm plate traps only 7-8% of its own volume. The network of interconnected solid metal struts creates little spherical chambers inside the foam that hold water due to surface tension. In contrast, the interrupted plate has straight square channels that are less likely to trap water. For the open accumulator CAES system, entrained water in porous inserts is a significant problem. It not only occupies volume that otherwise would be used for compression and expansion of air, it also reduces the amount of surface area for heat transfer. Loss in volume for compression and expansion reduces the power density of the chamber and the drop in surface area reduces compression/expansion efficiency. Initially, 6 sets of experiments are conducted without inserts. Following these baseline experiments, 7 sets of experiments are performed for each insert at different expansion times.

In contrast to the constant volume trajectories used in compression experiments, the volume trajectory is not uniform in all the expansion experiments. The expansion trajectories are determined by a fixed orifice area. The number of the turns on the needle valve is been used as a parameter to determine expansion flow rate by setting different flow resistances at downstream of the chamber.

4.2.1 Expansion tests procedure

For the baseline cases without any inserts, before any data collection, a number of steps of preparation are performed to get accurate and repeatable data. Initially the ball valve after the turbine meter is closed. A port on the top cap of the expansion chamber is opened and a funnel is used to preload the chamber with tap water up to an approximate initial water volume of 615 cc to get initial air volume around 100cc. An initial volume of 100cc is selected as a compromise between achieving high expansion ratios with high

uncertainty in V_0 and low expansion ratios with low uncertainty in V_0. Based on initial volume and fixed geometry of the expansion chamber, an expansion ratio of 6 is selected. Once the chamber is loaded to the designated height, the top port is sealed with an ORB-4 fitting and pressure regulator of the high pressure compressed air cylinder is set to 12.5 bar (182 psi). After, the expansion chamber is sealed and loaded, the ball valve connecting the chamber and the pressurized cylinder is opened to charge the expansion chamber to 12.5 bar (182 psi). The ball valve is closed once the chamber is fully charged. Later, initial estimation of air volume V_0 inside the chamber is measured by the graduation marks along the cylinder wall when the water air interface is stabilized. Because of the rapid charging, compressed air inside the chamber is slightly heated. Before starting the experiment, air is allowed to come to thermal equilibrium. The needle valve after the ball valve is used to control the expansion time. Due to the nature of the needle valve and expansion process, the flow rate is proportional to the square root of the pressure drop across the needle valve. Hence, unlike the compression experiments where flow rate can be controlled in real time by a control valve, the flow rates during the expansion experiments decreases as pressure decreases during the expansion process. Nevertheless, the orifice opening setting can be used to vary the expansion time and hence the expansion power density.

The DAQ system is turned on to acquire pressure $P(t)$, liquid flow rate $V(t)$ as measured by turbine meter and mass of liquid $m(t)$ flowing into reservoir as measured by the load cell. Two seconds after the DAQ system is on, the ball valve after the turbine meter is swiftly opened until the liquid level inside the chamber drops to a pre-determined height that would satisfy an expansion ratio slightly higher than 6. For

expansion times shorter than 4 seconds, the integral of the turbine meter flow rate is used to calculate the expanding air volume inside the chamber. For expansion times longer than 4 seconds, the volume of air inside the chamber is calculated based on the weight $\mathrm{m(t)}$ of the liquid exiting the chamber, assuming constant liquid density. During the post processing, weight $\mathrm{m(t)}$ is converted volume $\mathrm{V_{exit}(t)}$. Initial pressure, $\mathrm{P_0}$, is calculated by averaging the $\mathrm{P(t)}$ measurement at the first two seconds before ball valve is turned on. Initial temperature, $\mathrm{T_0}$, is measured by a thermometer.

4.2.2 Data reduction

Data processing and plotting are carried out using methods similar to the data reduction process in compression experiments. Significant differences are described below. Due to the rapid change in the flow rate at the beginning of expansion, both flow rate measurement devices are not reliable. For this reason, an adiabatic trajectory is assumed during the initial region using equation 4.1. Very quickly, the adiabatic trajectory and the measured trajectory come to agreement; at this point it is assumed that the measured flow rate is correct. Each process is carefully processed and the adiabatic trajectory is switched to the measured flow rate when they first agree, after the starting point.

$$V_{adi}(t) = \left(\frac{P_0 {V_0}^{1.4}}{P(t)}\right)^{\frac{1}{1.4}} \tag{4.1}$$

Because, the ball valve is opened and closed manually, it is impossible to have precise control on the ending of the expansion. All the expansion data are only processed only down to an expansion ratio of 6, for consistency, in contrast to the pressure ratio of

10 in the compression experiments. Once pressure and volume profiles are obtained, temperature inside the chamber is calculated using the ideal gas law:

$$T(t) = \frac{T_o}{P_0 V_0} P_{(t)} V_{(t)} \tag{4.2}$$

The quantity of air in the chamber is calculated from the measured initial conditions:

$$m_{air} = \frac{P_0 V_0}{R T_o} \tag{4.3}$$

Initially, V_0 is estimated by reading graduations on the expansion chamber. However, small error in initial volume leads to a large discrepancy in final temperature. In order to better characterize initial volume, V_0 , the concept of thermal equilibrium is again invoked and V_0 can be calculated from the following equations:

$$\frac{T(t)}{T_0} = \frac{P(t)}{P_0} \frac{V(t)}{V_0} \tag{4.4}$$

At final equilibrium, $T(t)$ returns to T_0 and $P(t)$ increases to P_{eq}. At the end of expansion, after the ball valve is closed, $V(t)$ is constant and equals to $V_0 + V_{exit}(end)$. With this in mind, V_0 is solved using the equation below:

$$V_0 = V_{exit}(end) * \frac{{P_{eq}}/{P_0}}{1 - {P_{eq}}/{P_0}} \tag{4.5}$$

This technique is used to correct V_0 because, as the uncertainty analysis shows it is more accurate than reading off the graduation marks. The detailed error calculation is shown in the following section. Similar to compression tests, with the calculated temperature profile $T(t)$, pressure volume trajectory $P(t), V(t)$ the total potential energy E_P that could be extracted from the stored compressed air product, the actual PV work output

W_{out} and efficiency η_e are calculated using equations 2.4 2.5 2.6 developed in chapter 2. As in the compression data processing, MATLAB's built-in numerical integration function is used when integration is necessary.

4.3 Uncertainty analysis

For the expansion experiments, three cases are considered: a baseline case without inserts, the 2.5mm spaced interrupted ABS plates case, and 5.0 mm spaced interrupted ABS plates case. The initial air volume is estimated using graduations that are on the outside of the expansion chamber and later corrected using an equilibrium assumption. Pressure is measured using a Kulite ETM-375 pressure transducer with a stated accuracy of ± 0.1% of full scale. Two methods are used to measure the volume of water that has left the chamber: an Omega FTB-1412 turbine flow meter and a custom made scale that utilizes a Transducer Techniques MLP-50 load cell. The turbine flow meter has an accuracy of ± 0.6% in the recommended flow range when the manufacturer's calibration curve is used. The load cell has an uncertainty ± 0.5% of reading at steady state. For slower cases, where the flow rate drops below the range of the turbine meter, the load cell is preferred. For faster cases, where the load cell has more oscillation due to the rapid exiting water jet and the turbine meter stays in its rated range, the turbine meter is preferred.

The uncertainty in efficiency and work output is trajectory dependent. For simplicity, two extremes are considered: isothermal and adiabatic trajectories. Actual experimental cases will fall between these two extremes. For both trajectories a general error propagation equation (4.6), as developed by Kline and McClinktock [51] is used.

$$\delta F(x_1, x_2, x_3 \ldots) = \sqrt{\sum_{i=1,2,3\ldots} \left(\frac{\partial F}{\partial x_i}\delta x_i\right)^2} \qquad (4.6)$$

where F is some function of variables x_i and δx_i is the uncertainty in variable x_i. The uncertainties in final volume, V_f, work output, and efficiency are found and reported in Table 4.1 for both volume measurement methods and both isothermal and adiabatic trajectories.

Table4.1. Detailed uncertainty analysis for expansion experiments

% error	**Cases Using Turbine meter**	**Cases using Load cell**
% Error in V_0 (Isothermal Trajectory)	1.23%	1.18%
% Error in V_0 (Adiabatic Trajectory)	0.97%	0.91%
% Error in V_f (Isothermal Trajectory)	0.54%	0.46%
% Error in V_f (Adiabatic Trajectory)	0.51%	0.44%
%Error in Work Output (Isothermal Trajectory)	1.24%	1.19%
%Error in Work Output (Adiabatic Trajectory)	0.52%	0.47%
Error at 100% Efficiency (Isothermal Trajectory)	1.20%	1.16%
Error at 90% efficiency	0.89%	0.85%
Error at 80% efficiency	0.58%	0.54%
Error at 74.3% Efficiency (Adiabatic Trajectory)	0.39%	0.36%
%Error in Power density (Isothermal Trajectory)	1.36%	1.29%
%Error in Power density (Adiabatic Trajectory)	0.80%	0.75%

A linear interpolation is used to determine the typical uncertainty for trajectories that are 90% and 80% efficient. Since the initial volume, V_0, is calculated through equation 4.5,

the percentage error for V_0 is constant for all cases with or without inserts. Unlike the compression experiments V_0 has different uncertainties for cases with different inserts. The volume, V_0, for expansion experiments remains a constant value and the same uncertainty, this lead to the same percentage error in efficiency calculation for all three different insert cases. Similar to the compressed experiments, the uncertainties in final volume, work output and expansion efficiency are also depends on the expansion trajectory. In table 4.1, detailed uncertainties for both adiabatic and isothermal expansion processes are calculated.

Chapter 5

Results & Discussion

5.1 Compression results without inserts

Detailed individual sample data processing and results for a compression experiment without inserts are shown in Appendix C.1. In this section, compression results without inserts are all shown in summary plots. A total of 11 constant flow rate experiments without inserts are performed to establish a baseline at a fixed compression ratio of 10. Compression times ranges from 2 seconds to 60 seconds and power densities ranges from 3.8kW/m^3 to 182kW/m^3. The compression efficiency is plotted against power density in figure 5.1. The general trend is clear, as power density increases, efficiency decreases. In order to achieve isothermal compression, input power must be balanced by heat flux from the air to the heat sink, such that the change in internal energy is zero. As power density increases, heat flux cannot keep up with input power so an increase in internal energy is inevitable. For a fixed compression ratio, fixed compressor volume and the same initial pressure, power density is inversely proportional to compression time. During the compression experiments, the highest bulk temperature of the air could reach temperature higher than 450 K. In order to compare the temperature rises relative to initial temperature between compression processes with different compression times in a single plot, dimensionless temperature is defined as the ratio of instantaneous bulk temperature to initial temperature. The corresponding dimensionless

temperature profile is shown in figure 5.2. Where y-axis is dimensionless temperature and x-axis is normalized compression time or air volume.

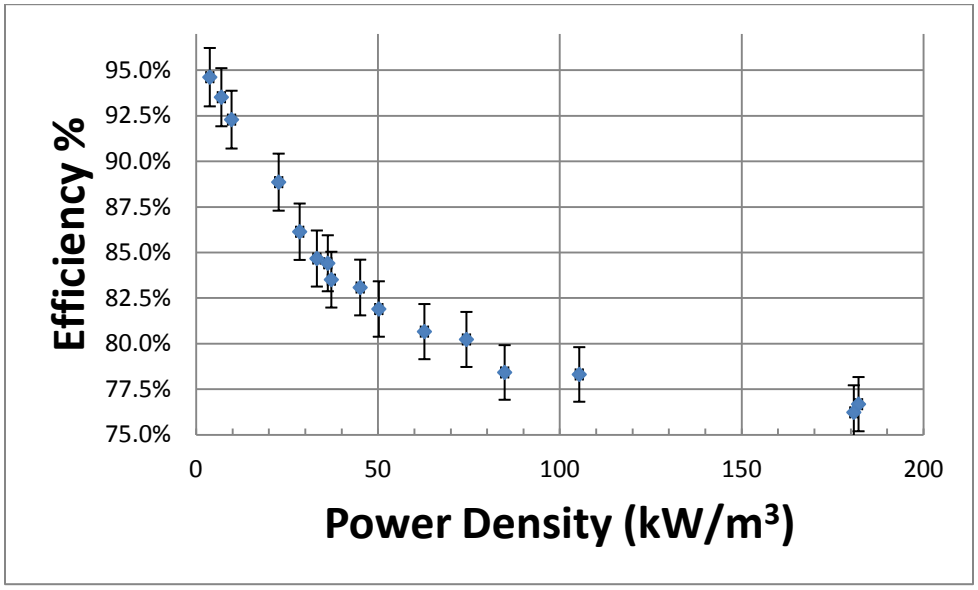

Figure 5.1: Baseline compression efficiency vs. power density for cases without an insert

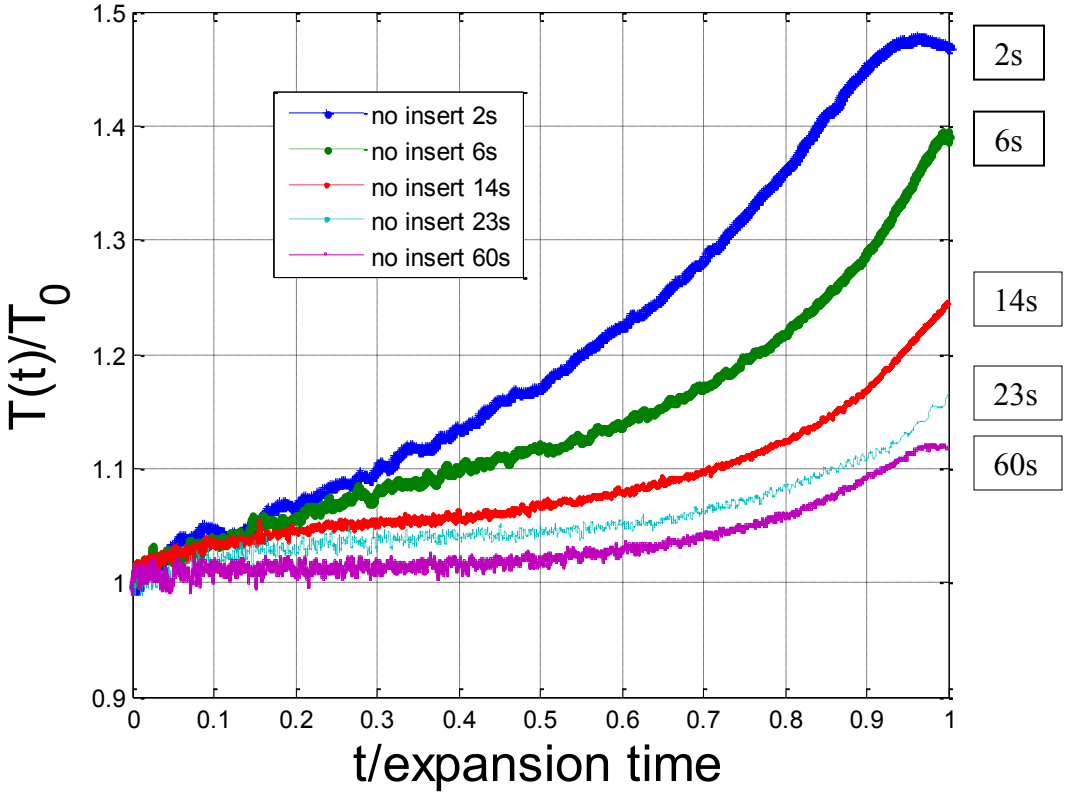

(a)

Figure 5.2: Dimensionless temperature profile vs. normalized compression time for five compression experiments at different compression time

As shown in the figure a shorter compression time leads to higher temperature rise. In addition, another observation worth noting occurs near the end of a rapid compression process, temperature of the air is so high that it substantially accelerates the evaporation process at the liquid air interfaces. The humidity of air is significantly increased, while the wall temperature remains constant, vapor in the air starts to condensate on the cool polycarbonate cylinder wall. Tiny water droplets formed a thin layer of water film after compression. The evaporation of liquid actually increased the heat transfer between air and surroundings. That explains the decreases in temperature near the end of compression process with a compression time of 2s, in figure 5.2. However, by looking as the dimensionless temperature profile, it is still hard to imagine how efficient or inefficient the processes are. In figure 5.3, normalized pressure volume trajectories of 5 selected compression processes with different compression times are plotted against the normalized isothermal and adiabatic trajectory. As compression time is decreased from 60s to 2s, the trajectory deviates from the near-isothermal trajectory and approaches the adiabatic trajectory shown in figure 5.3. Based on the compression efficiency defined for open-accumulator CAES system, using the experimental conditions defined before. The worst case is an adiabatic process which has an efficiency of 70.7%. From figure 5.1, the lowest efficiency case is 76%, which is not acceptable for a CAES application since other system losses are not considered yet, the overall efficiency could be a disaster. Although the highest efficiency is 94%, this comes at the cost of very low power density which is also undesirable. For a CAES application, an ideal compressor would maintain high efficiency without lowering power density. By adding porous inserts

to the compression chamber, this ideal can be approached. In the next section, the results for cases with four different types of porous inserts are presented and compared.

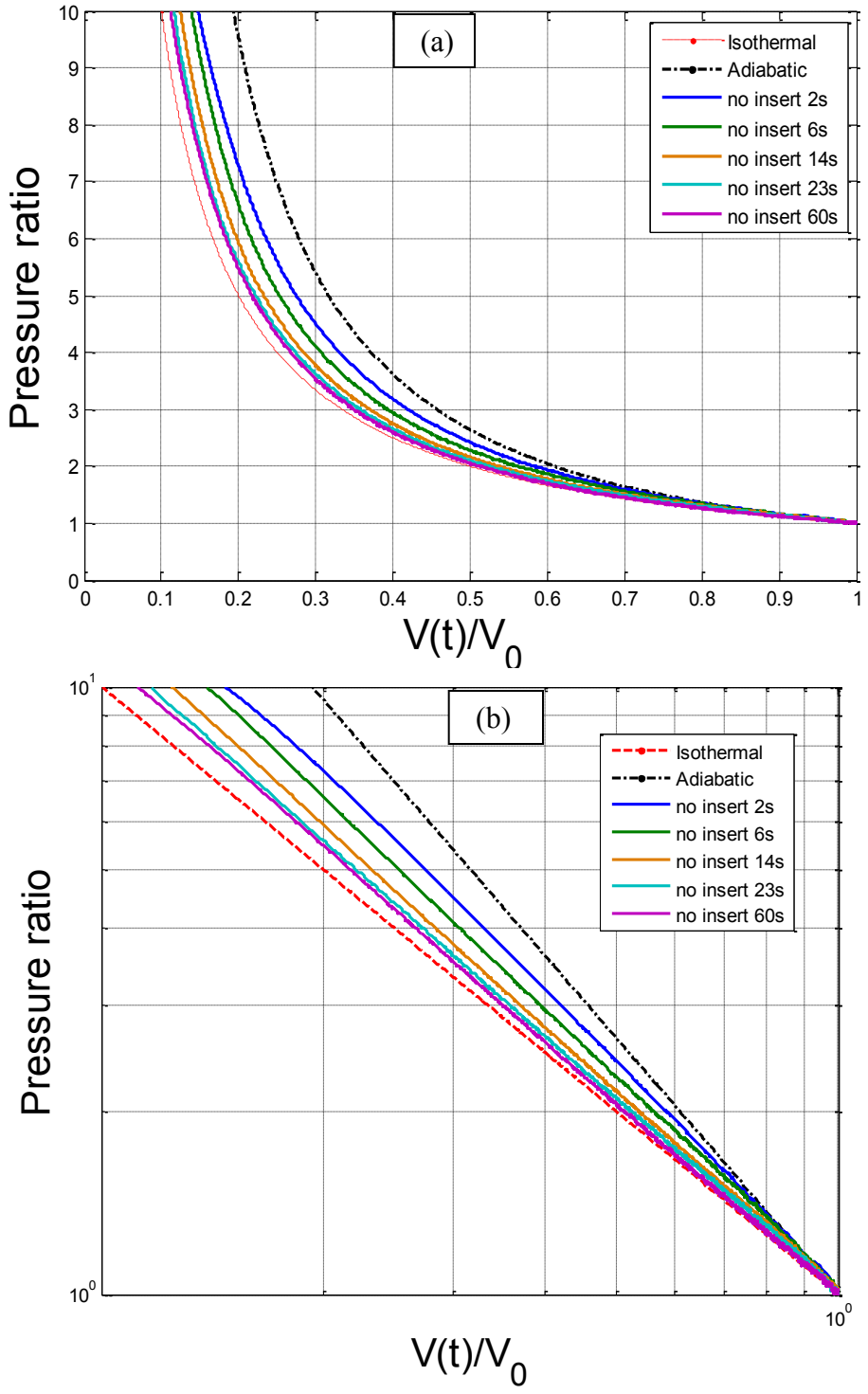

Figure 5.3: (a) Normalized pressure-volume trajectories for five baseline cases without inserts at different compression times compared to isothermal and adiabatic compression trajectory (b) Normalized PV trajectory in log scale

5.2 Compression results with porous inserts

Detailed individual sample pressure, volume profile, efficiency and power density results for a compression experiment with inserts please refer to Appendix C.2. In this section, compression results with porous inserts are all shown in summary plots. Seven to eleven constant flow experiments are run for each insert. The compression times for these experiments ranges from 1.4 seconds to 6.5 seconds which corresponds to power density ranges of 29.4kW/m^3 to 154kW/m^3. Efficiencies for all of these runs are dramatically improved compared to cases without an insert, all above 90%. The results are plotted against power density in figure 5.4. Like the set of experiments with no insert, a similar trend is observed where efficiency decreases as power density increases. As the reader may notice, there is a substantial amount of scatter in the data; however, this scatter is in line with what uncertainty calculations suggest. This scatter is also present in the no insert case, but appears less significant since the efficiency changes by 10% over the range as opposed to the 4-6% change in efficiency seen for the insert cases.

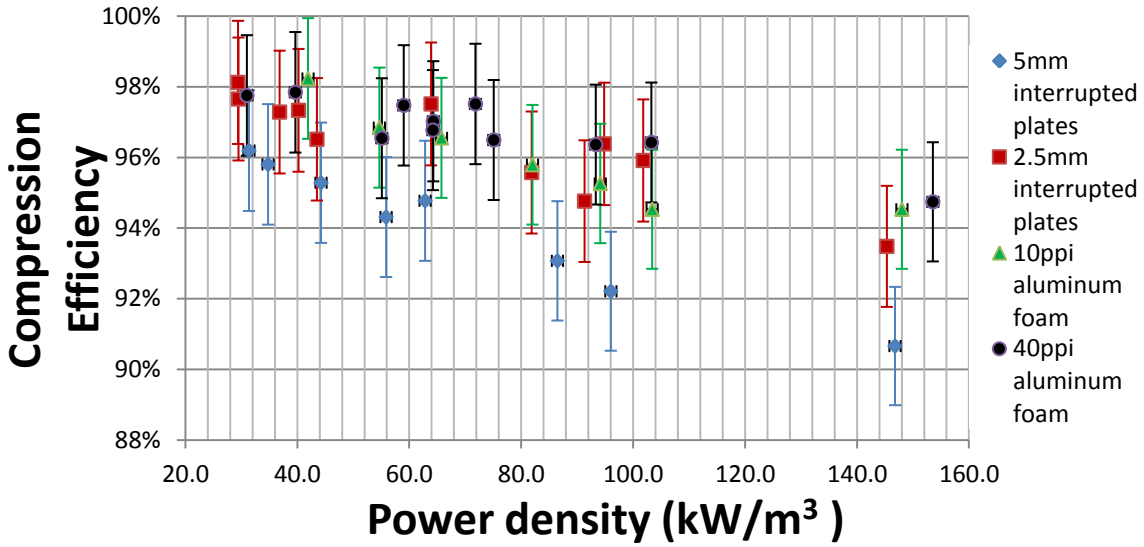

Figure 5.4: Efficiency vs. power density with error bars for four porous inserts at compression ratio of 10

In Figure 5.5 the efficiency vs. power density data for the compression tests with porous inserts are plotted and compared together against the baseline cases without any inserts:

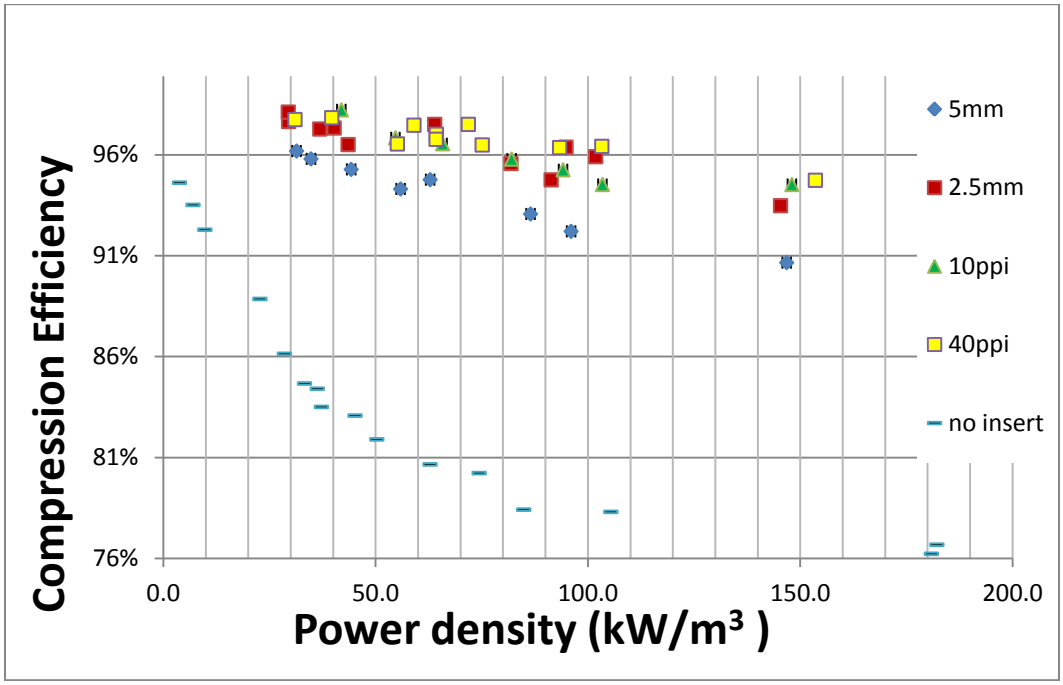

(a)

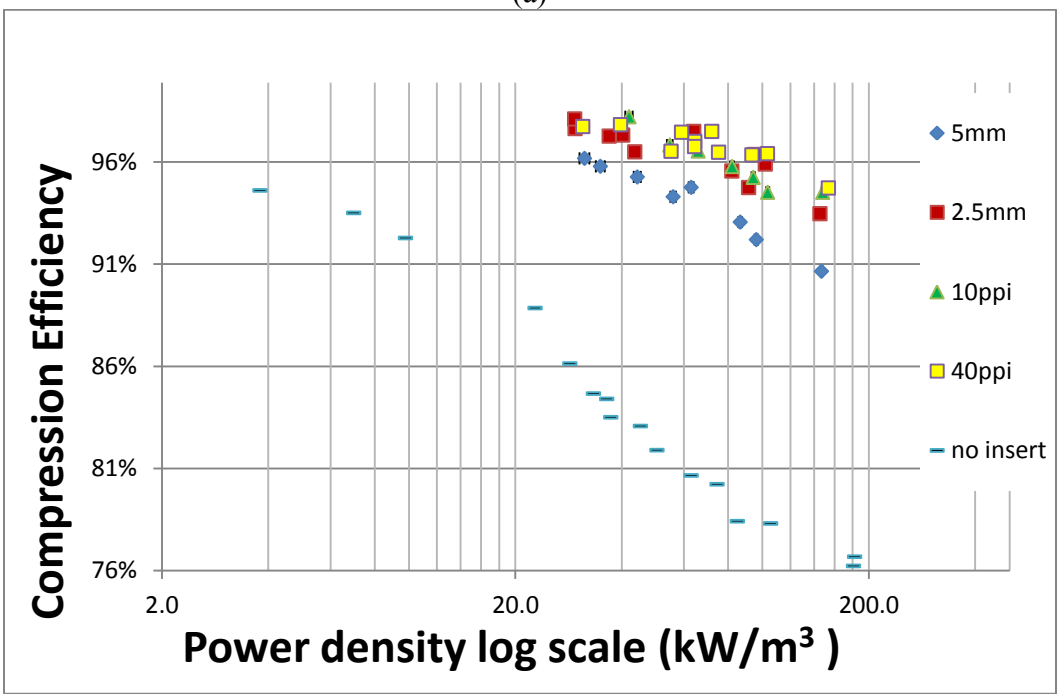

(b)

Figure 5.5: (a) Efficiency vs. power density for all compression experiments at compression ratio of 10 (b) Efficiency vs. power density in log scale for all compression experiments at compression ratio of 10

From the figure above, the gain in efficiency is obvious. However, it is hard to differentiate which inserts are more effective at a constant power density by just looking at these congested data points. Dimensionless temperature profiles and normalized PV diagrams could be used as visual representation of the performance characteristics of the each individual insert under a constant power density. In figure 5.6, dimensionless temperature of all four types of inserts with a compression time of two seconds is plotted against the normalized compression time. Apparently, the bulk temperature of the air does not rise as high and as quickly as the case without an insert at the same compression time. The 5mm plate has the highest temperature rise, and the 40ppi case has the lowest temperature rise. Interestingly, the performance levels of the 2.5mm plate cases and 10ppi plate cases are very close. In figure 5.7, normalized pressure-volume trajectories for all insert cases at a compression time of 2s are plotted against isothermal and adiabatic trajectories.

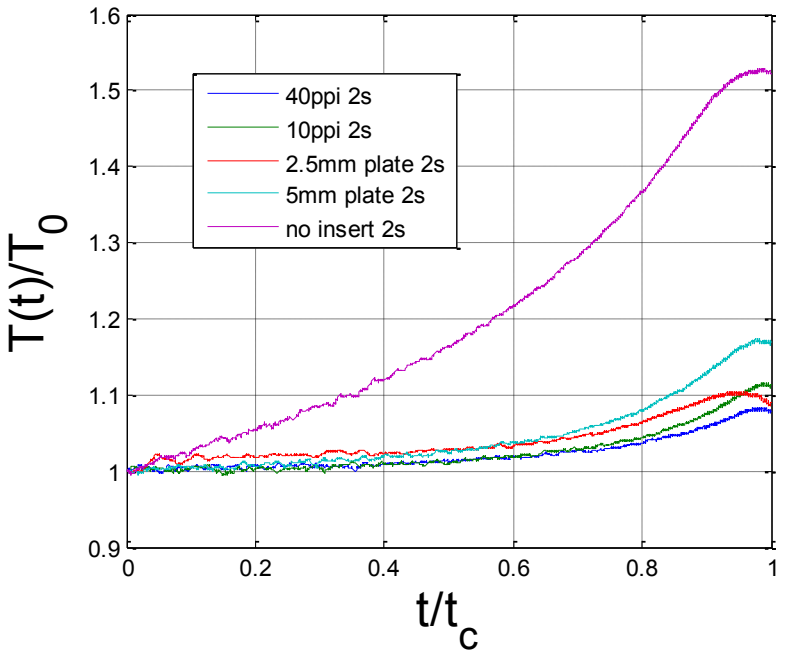

Figure 5.6: Dimensionless temperature profile vs. normalized compression time for five compression experiments with different porous inserts at different compression times

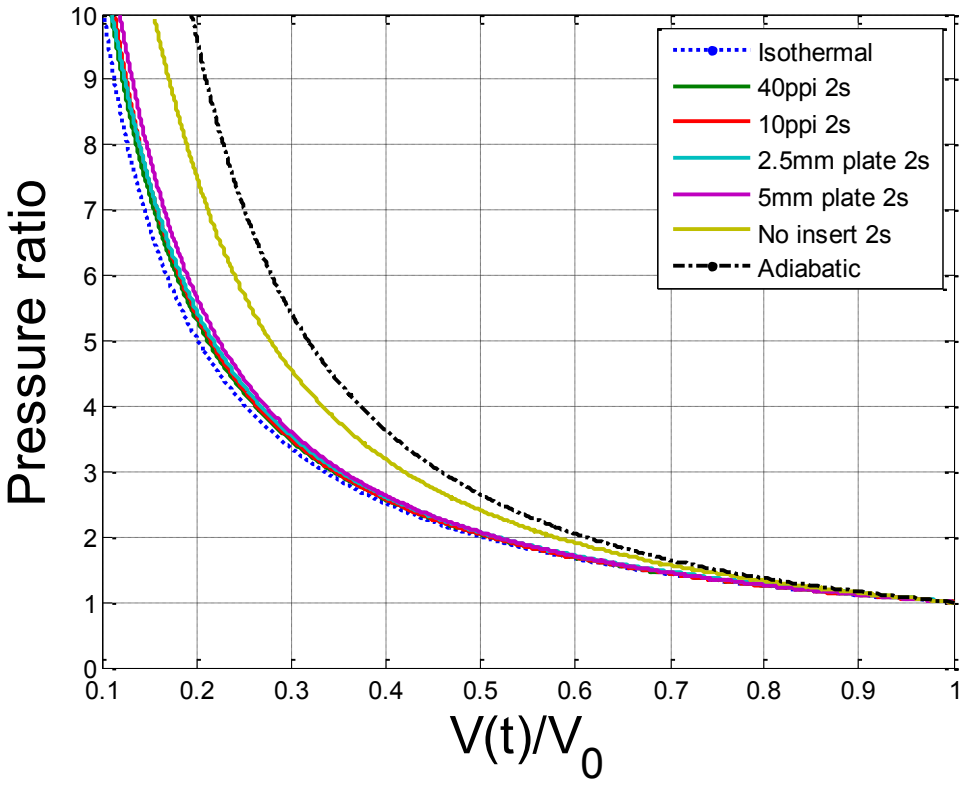

(a)

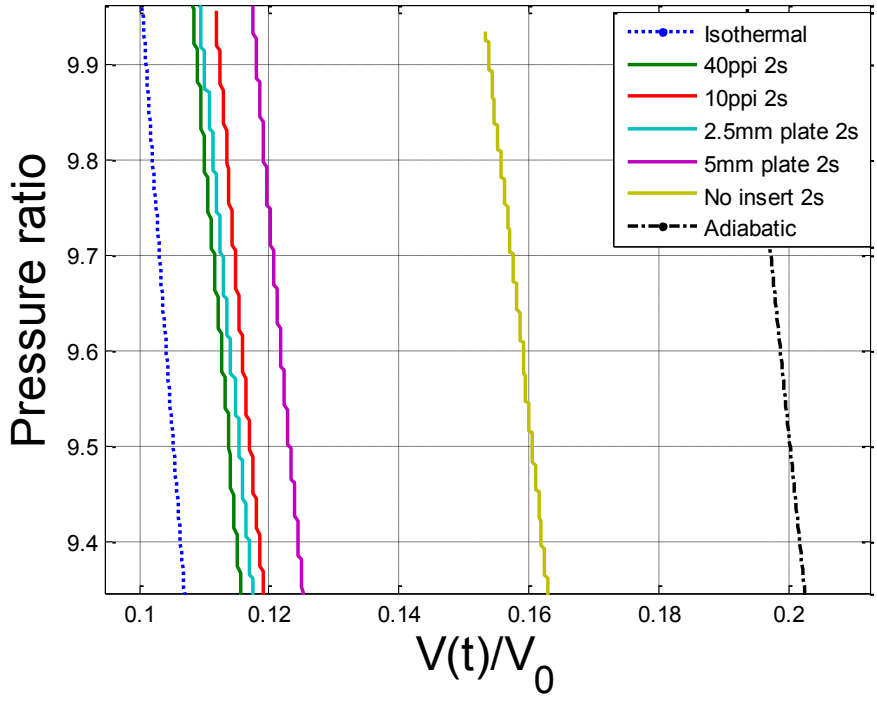

(b)

Figure 5.7: (a) Normalized pressure-volume trajectories for all inserts at compression time of 2s compared to isothermal and adiabatic compression trajectory (b) zoomed in view of (a) near the end of compression process. The order of efficiencies are listed on top of (b)

The PV trajectories for all compression processes with porous inserts are very close to isothermal line and in figure 5.7(b) a zoomed-in view near the end of the process is shown to identify which insert has the best performance. It seems that 40ppi metal foam is the leader and 5mm interrupted plate ranks the last. Cases with 10ppi metal foam and 2.5mm plates reside in the middle. It seems that the performance is directly related to the surface area available for heat transfer. The 40 PPI has the most surface area and the highest efficiencies while the 5mm has the lowest amount of surface area and has the lowest efficiency, when compared to the other insert cases. The initial surface areas for the four inserts and the no insert case are compared in figure 5.8.

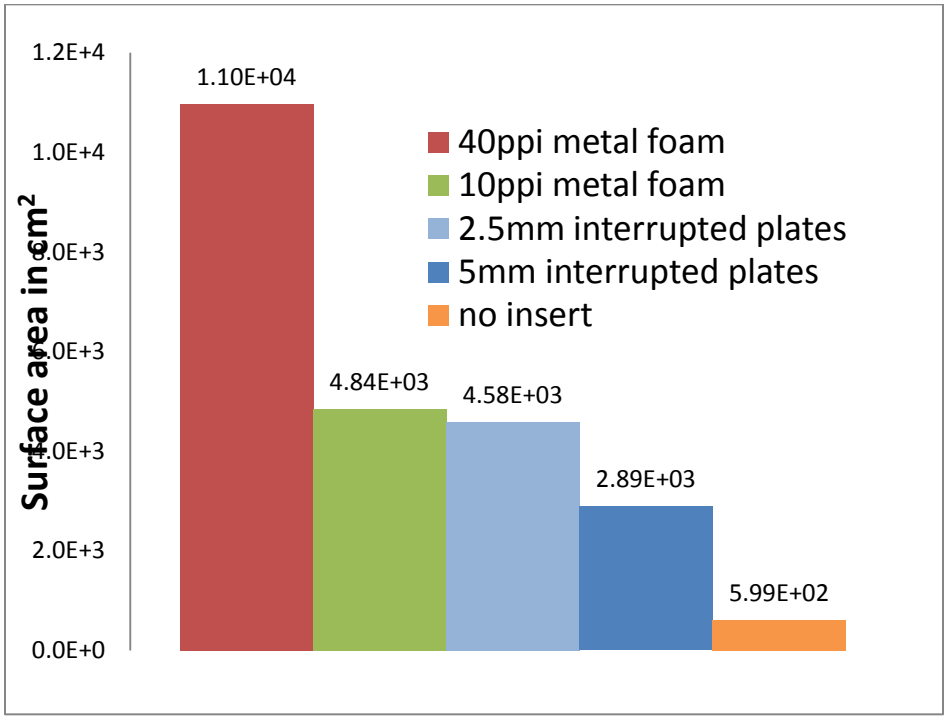

Figure 5.8: Initial heat transfer surface area comparison for four inserts and no inserts case

Because the efficiency of the compression process seems to be largely driven by the total amount of available heat transfer area, a new concept of power density per specific area is introduced. This parameter is found by dividing the power density by the

specific area of the insert. Essentially, it is the average power stored during the compression process divided by the total amount of heat transfer surface area available at the onset of compression. The unit of this parameter is W/m^2. When efficiency is plotted verse this parameter, as shown in Figure 5.9, the data roughly collapses to one curve. This trend suggests that compression efficiency can be increased by either decreasing power or by increasing the amount of surface area available for heat transfer. For instance, the efficiency of a 1kW compressor with an initial area of 1 m^2 of available heat transfer surface area can be increased from below 80% to about 95% by adding 10 m^2 of heat transfer area. This is easily achievable with the inserts that were examined in this study.

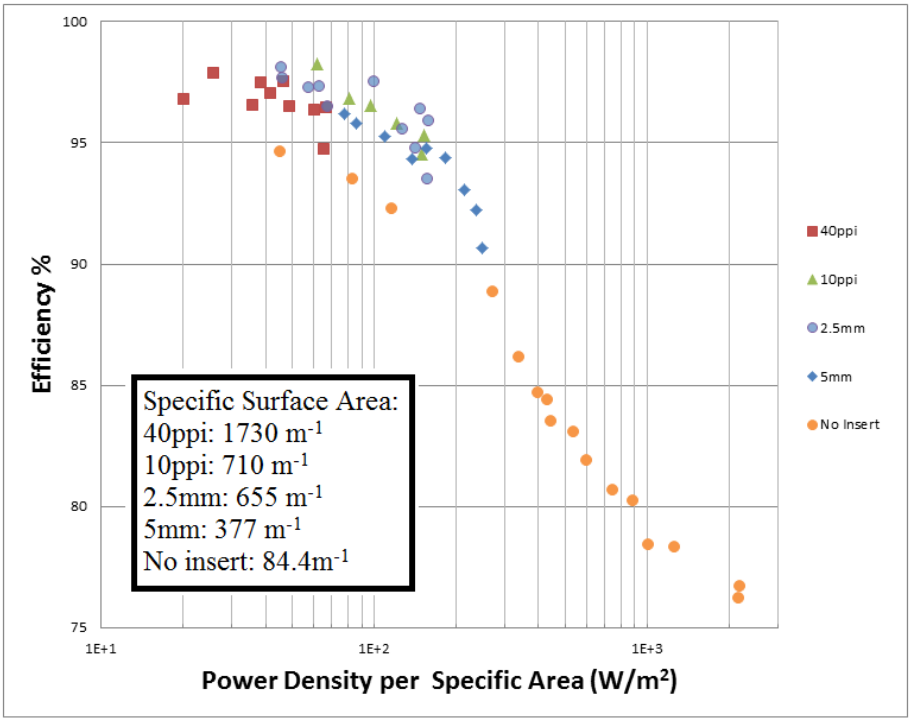

Figure 5.9 Compression Efficiency vs. Power Density normalized by initial total heat transfer area at compression ratio=10

The reader will also notice that the effectiveness of adding heat transfer area decreases as efficiency increases. When power density per specific area is reduced to very low values, the rate of efficiency improvement approaches zero. In fact if the surface

area is increased to a certain level, the pressure drop due to viscous shear will overwhelm the gain in heat transfer. Since it is the averaged *hA* product (defined in equation 2.38) that governs the total amount of heat transfer and the heat transfer coefficient, *h*, is a function of the pore size, it decreases as heat transfer area increases. This trend can be observed in figure 5.10 where efficiency is plotted against averaged heat transfer coefficient, *h*, at a constant power density of 100kW/m^3. However, the gain in adding more surface area diminishes as pore size gets smaller and heat transfer coefficient decreases. Further study should be conducted to find the optimum *hA* product that would allow for maximum heat transfer.

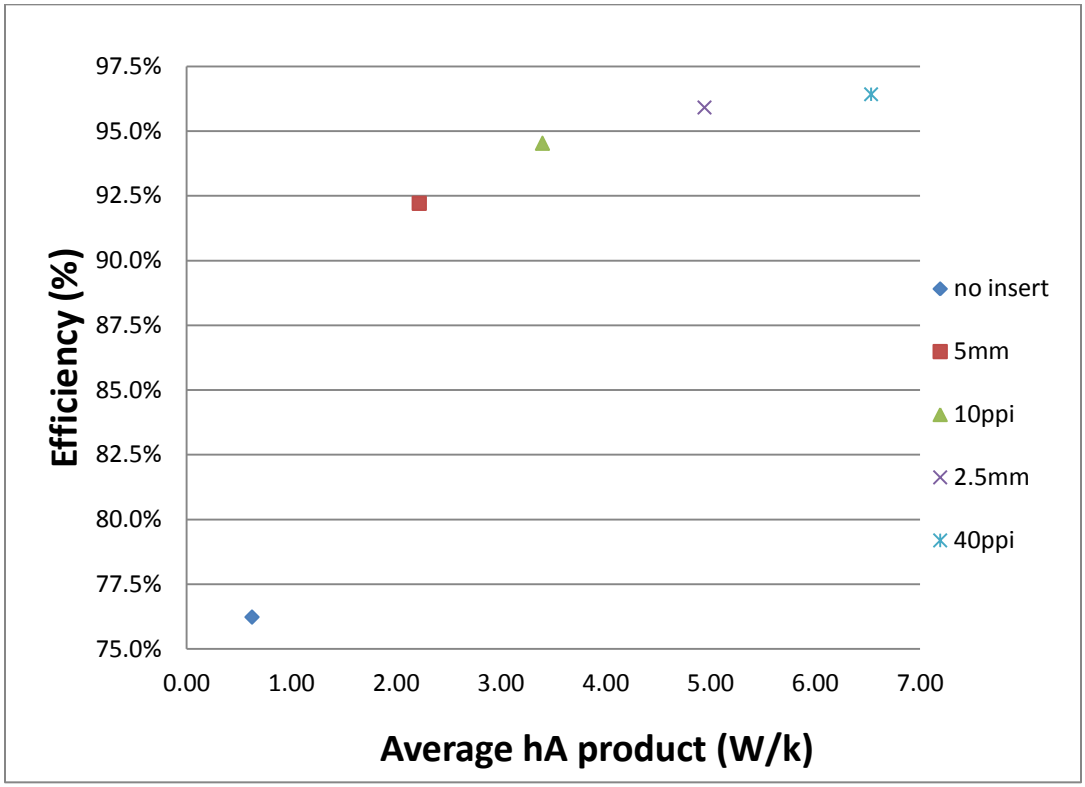

Figure 5.10: Efficiency vs. averaged *hA* product defined in equation 2.38 for compression processes around 100kW/m^3

5.3 Expansion results

Expansion experiments are conducted with flow trajectories determined by a constant orifice. Detailed individual pressure, volume profile, PV trajectory, efficiency and power density results for an expansion experiment please refer to Appendix C.3. In this section, expansion results with and without porous inserts are also shown in summary plots. The flow rate of the expansion process is controlled by a number of turns on the needle valve creating different orifice areas thus different flow rates for each expansion process. The flow rate across the needle valve is proportional to the square root of the pressure drop across the needle valve. The sample flow rate profiles for the expansion experiments are shown in figure 5.11. A total number of 6 experiments without inserts are performed to establish a baseline at a fixed expansion ratio of 6.

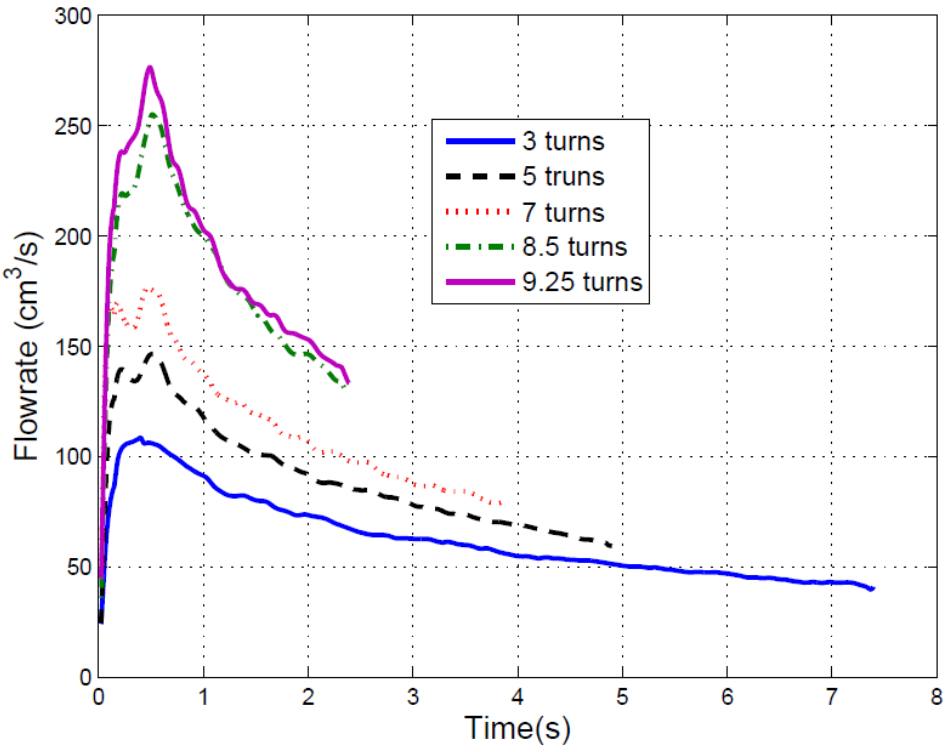

Figure 5.11: Sample flow rates profile for expansion experiments

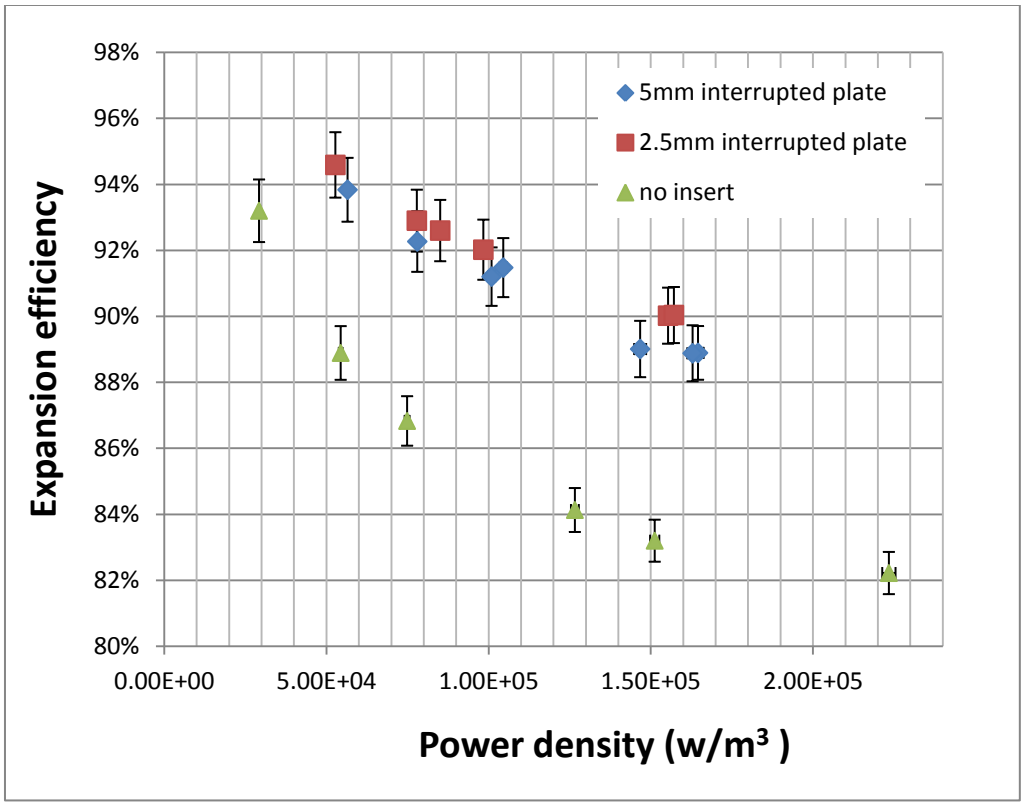

Figure 5.12: Expansion efficiency vs. power density at expansion ratio of 6 for baseline case and two different inserts

Expansion times range from 2 seconds to 16 seconds and corresponding power density ranges of 29kW/m^3 to 223kW/m^3. Additionally, 2.5mm and 5mm interrupted plates are tested at the similar testing conditions. The efficiencies from these sets of experiments are plotted against corresponding power densities in figure 5.12:

The general trend is the same as for the compression experiments. As power density increases, efficiency decreases. At a certain power density, the insert cases have much higher efficiencies. These trends are expected due to the increase in available heat transfer area as discussed in previous chapters. The efficiency for expansion processes seems higher than the compression results at the same power density because the expansion ratio is only 6 other than 10 in compression experiments. Also, the initial air product in expansion experiments has a higher pressure compressed to the final air

product produced in compressed experiments. In addition, the flow rate profile of the expansion processes are lot different than the compression processes, since the flow rate is controlled by a needle valve, it is not constant. The goal of adding porous inserts is to reducing the drop in temperature as opposed to reduce the temperature rise in compression experiments. As shown in figure 5.13 at approximately the same expansion rate, both the 2.5mm and 5mm inserts dramatically decrease the temperature drop. The same temperature profiles are plotted against volume in figure 5.14. It should be noted that although processed to the same expansion ratio, the final volumes of each process are highly trajectory dependent. As an expansion process approaches an isothermal trajectory, the final volume ratio approaches the expansion pressure ratio shown in figure 5.14.

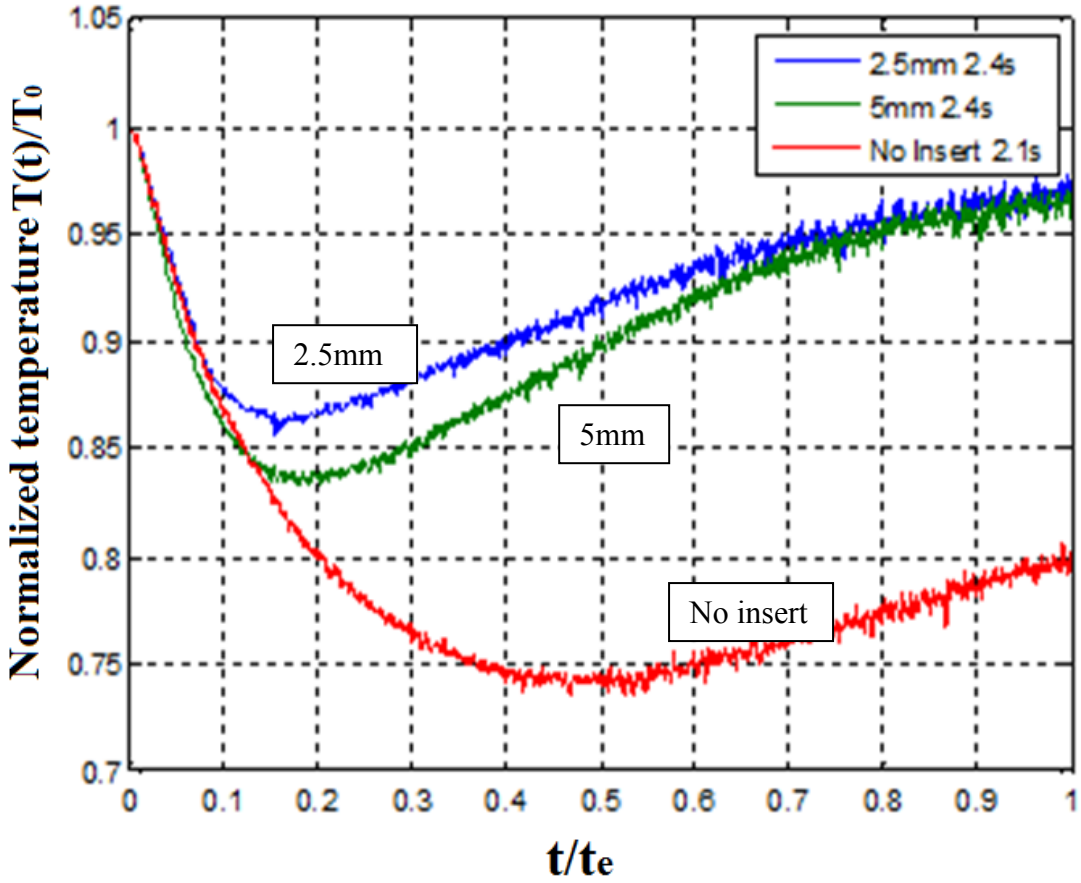

Figure 5.13: dimensionless temperature profile vs. dimensionless expansion time for three different cases at similar expansion time

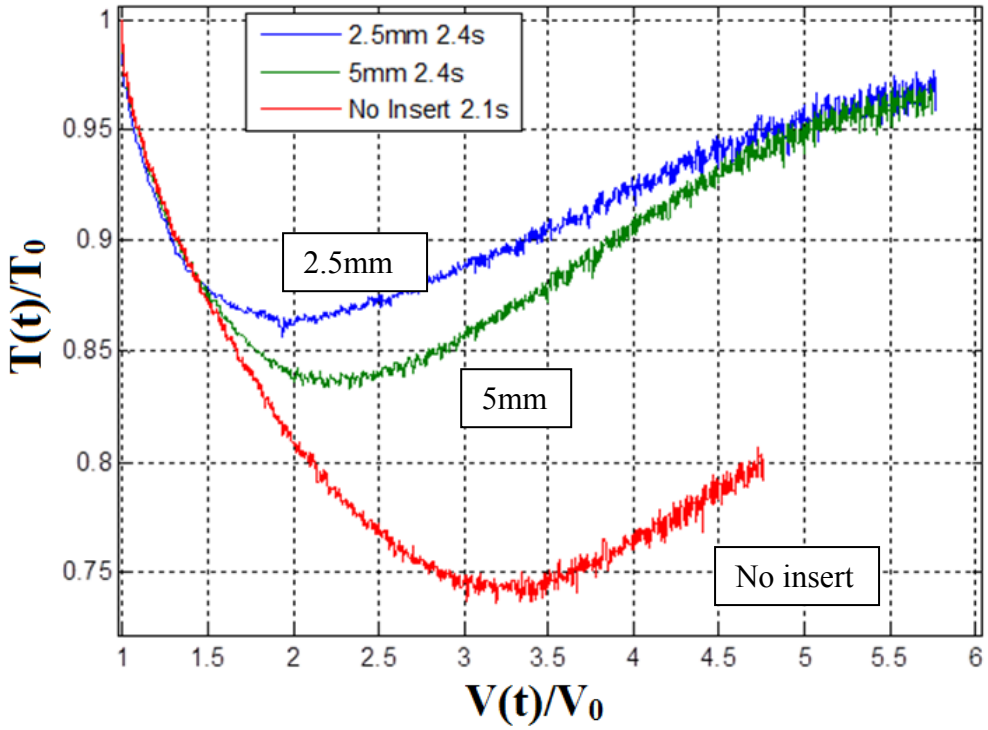

Figure 5.14: dimensionless temperature profile vs. volume ratio for three different cases at similar expansion time

In figure 5.15, the P-V trajectories for two interrupted plates and a baseline case are compared to isothermal and adiabatic trajectories. All three experimental trajectories are close to adiabatic at the beginning of the process and approach isothermal near the end. This phenomenon is due to a combination of reasons. First of all, the flow rate of the expansion process is fast at the beginning and slows down during the expansion process. Additionally, the exposed insert surface area is zero at the onset of expansion. As the expansion process proceeds, the expansion rate decreases and additional surface area becomes available for heat transfer. The combined effects of small heat transfer area and rapid expansion rate at the onset of expansion results in near-adiabatic trajectory at the beginning, as shown in figure 5.15. This adiabatic behavior causes the sudden drop in temperature shown in figure 5.14, which leads to the rapid decrease in internal energy as

shown in figure 5.16. As the expansion progresses, the flow rate slows and heat transfer area is dramatically increased. This explains why the experimental trajectory approaches the isothermal curve at the end of expansion. From conservation of energy, the change in internal energy is equal to the amount of heat transfer into the system minus the amount of work that has been extracted from the system. A balance of these three forms of energy is shown for a typical expansion process using 2.5mm inserts in figure 5.16

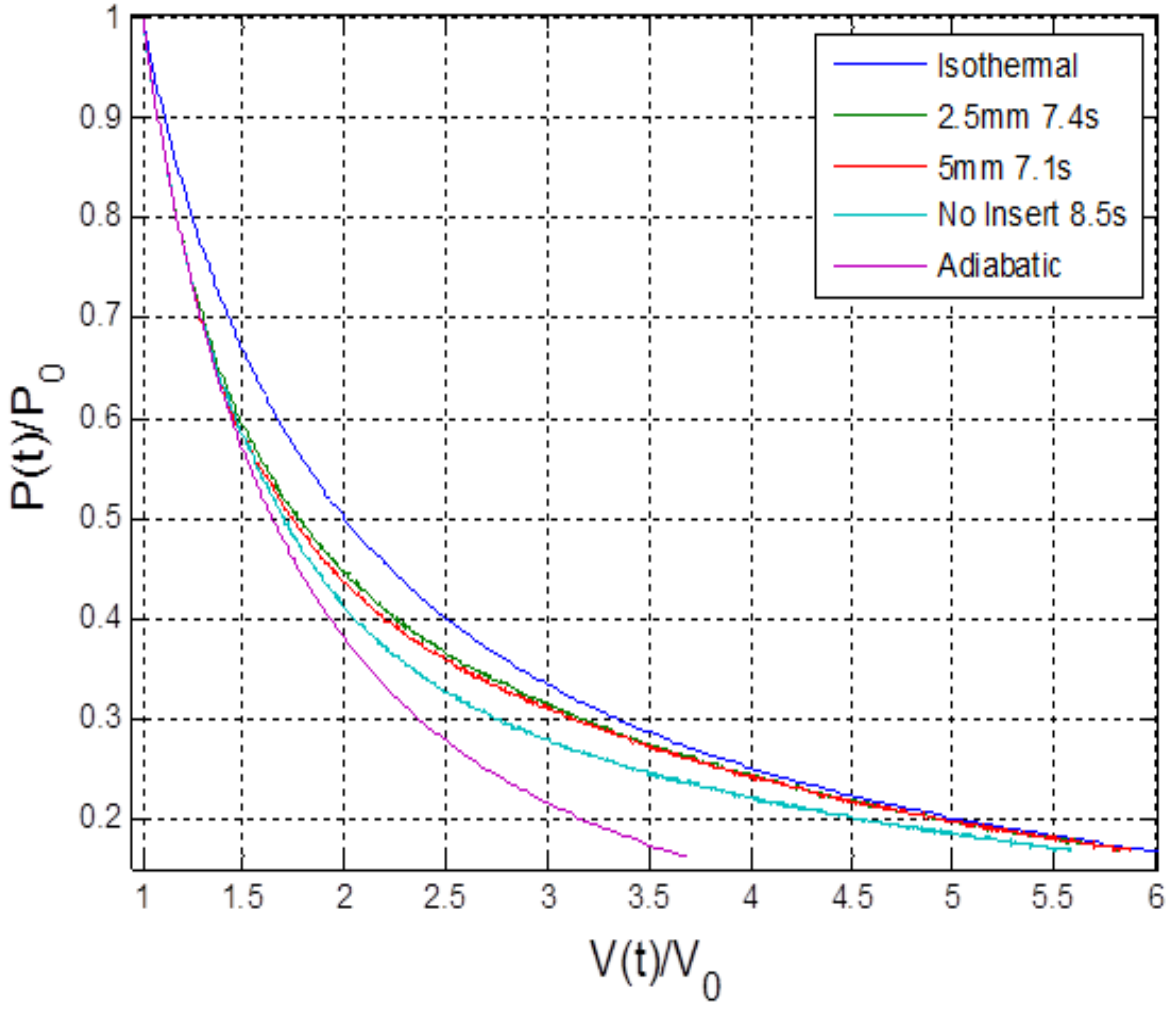

Figure 5.15: Dimensionless pressure volume trajectories for comparing two different inserts against baseline at approximately the expansion time

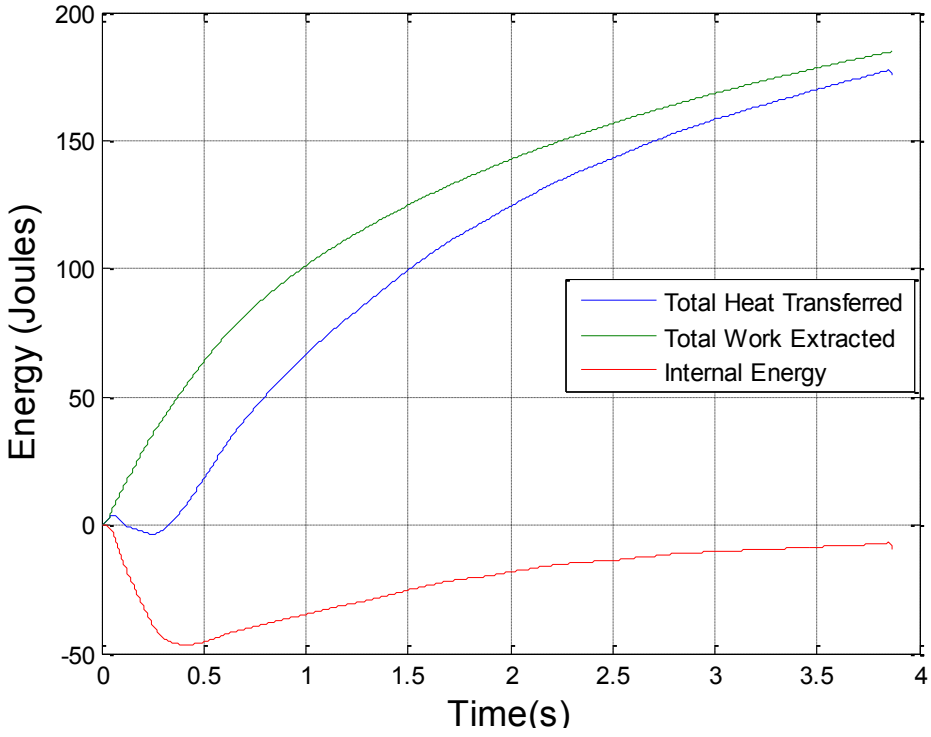

Figure 5.16: Typical energy balance profiles for an expansion process with 3.8 second expansion time with 2.5mm insert

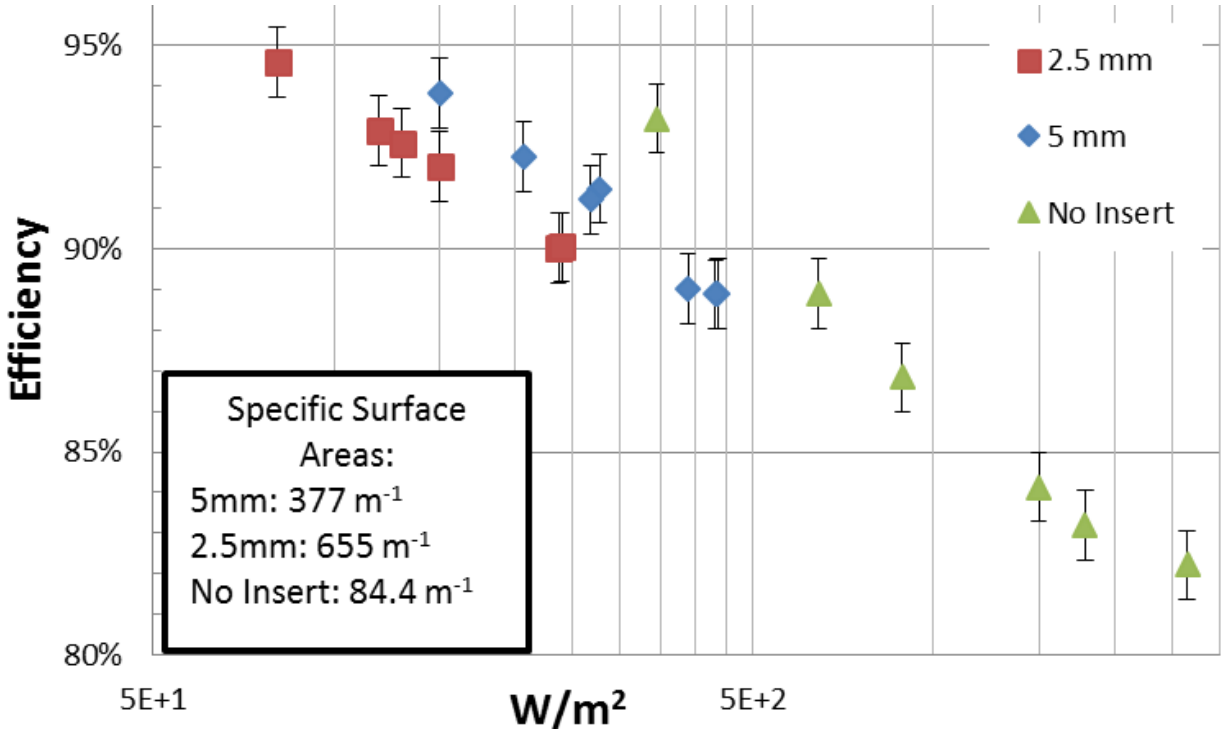

Figure 5.17: Efficiency vs. average power density per specific heat transfer area for an expansion ratio of 6

The addition of porous inserts improves the performance of an expansion process. This is primarily due to the large amount of surface area that is added, promoting heat transfer. Similar to the compression process, the efficiency of an expansion process seems to depend on both power and surface area available for heat transfer, in order to account for both effects, power density per specific area is introduced (or average power per area). In figure 5.17, efficiency is plotted against power density per specific area for all of the experimental expansion data taken. The specific surface areas used in each case are also shown.

Again, the general trend is the same as in the compression experiments, with the same insert, the smaller the power density per specific area, the larger the efficiency. The reader may notice that the data do not collapse perfectly. Under the same power density per specific area, the no insert cases appear to have higher efficiency than the cases with inserts. The first possible explanation is that the actual surface area participating during expansion is different than the designed surface area. This would be true if, for instance, water remained entrained in the pores of the insert. The entrained water prevents the air from being in contact with the surface area inside that pore thus reduces the effective heat transfer area. This effect aggravates as pore size decreases. This would also explain why under a given power density per specific area, the 2.5mm insert has a lower efficiency than 5mm insert. Perhaps another major reason is that the convective heat transfer coefficient, h, is different. If one assumes that the area used in the normalization is in fact the actual area that participates in heat transfer during the experiments, then figure 5.17 suggests that no insert cases have the highest h, followed by the 5mm then 2.5mm cases.

Chapter 6:

Conclusion and Discussion

The objective of this thesis study is to improve the thermal efficiency of a liquid piston air compressor/expander that could be used in an Open-Accumulator CAES system, without sacrificing power density. The heat transfer between the air and surroundings during a compression or expansion process is found to be the key parameter to improve efficiency. Porous inserts are used to increase the surface area, thus increasing the heat transfer rate. The improvement in efficiency is significant. Four types of porous media have been tested along with the empty chambers without any inserts. Two types of aluminum metal foam, 10ppi and 40ppi, and two types of ABS interrupted plates, 2.5mm and 5mm are tested. The compression experiments are conducted at constant flow rates with a power density ranging from 3.8kW/m^3 to 182kW/m^3 and a compression ratio of 10. Expansion experiments are carried out at power densities of 29kW/m^3 to 223kW/m^3 with an expansion ratio of 6 using trajectories that are determined by fixed orifice. Compared to cases without porous inserts, compression efficiency is improved from 78% up to more than 96% using 40ppi metal foam at 100 kW/m^3 power density. In the expansion experiments, efficiency has been increased from 83% to 90% when a 2.5mm interrupted plate is used at a power density of 150kW/m^3. The boost in efficiency that inserts provide increases as power density increases. This is seen in both compression and expansion experiments, but the effect is more prominent in the compression processes due to larger

pressure ratio. For the compression cases, the increase in efficiency ranges from approximately 10% at low power densities to approximately 18% at high power densities.

However, the author found that although the 40ppi has the best performance in increasing heat transfer rate, it also can trap water up to 90% of its own volume inside tiny spherical cavities which make it undesirable to be used with a reciprocating liquid compressor/expander in a CAES system. 2.5mm plates have similar capability in increasing compression/expansion efficiency (only 1% lower than 40ppi), but does not trap nearly as much water compared to aluminum foams. An uncertainty analysis is performed for both compression and expansion tests showing a maximum of ±2.2% error in the compression efficiency and ±1.2% error in expansion efficiency calculations.

Unfortunately, the volume trajectories used in this study are limited by the capability of the experimental setup. The author believe that by adopting optimized AIA (Adiabatic Isothermal Adiabatic) trajectories (In a fast-slow-fast pattern of flow rate) for compression and expansion processes developed by Rice [21] can significantly increase the power density of a compression/expansion process at the same efficiency (more than 20%), or increase the efficiency at the same power density. Further study on the experimental validation is necessary and recommended.

Porous inserts were found to be excellent candidates for applications requiring high compression ratios and high efficiencies without sacrificing power density in an open-accumulator CAES system. Future work should be done on investigating the combined effects of coupling porous inserts with other efficiency enhancing measures such as optimized compression chamber geometry, liquid sprays [52], and optimized compression/expansion trajectories [20].

This study focuses only on compression/expansion processes under low pressures (up to10 bar). In an Open-Accumulator CAES system, air is expected to be compressed or expanded at pressures higher than 20.7MPa (3000psi). Compressing air to this kind of high pressure consumes much more work input. Thus requires much higher heat transfer rates to the surroundings to reach near-isothermal compression. To expand the air from 20.7 MPa would also require stronger heat transfer rates from the heat source to avoid temperature drops and achieve near-isothermal expansion. Whether the porous insert is capable of boosting heat transfer rates high enough to reach efficiencies higher than 95% is unknown. Unfortunately, the current experimental setup is not capable of simulating compression or expansion process that is higher than 10bar. In order to investigate the performance of porous inserts at a much higher pressure conditions and a much wider compression/expansion ratios a new experimental setup should be designed and built. In the following chapter, the author describes a design process of a high-pressure compression/expansion system that could be used in future studies on this topic.

Chapter 7

Continuation

(Design of high pressure compression/expansion system)

7.1 Objectives

The purpose of this chapter is to summarize what we have learnt from the low pressure compression/expansion system and describe the design process for a high pressure compression/expansion system. The new system will allow much greater pressures, and have an improved volume measurement method, smoother control of flow rate, a much greater range of compression/expansion ratios, an additional active cooling system with spray nozzles, and greater ease of use. Such improvements in capabilities would allow for more thorough and accurate characterizations of the performance of both the porous inserts and the spray cooling through a wider and more realistic range of power densities.

7.2 Summary of pros and cons of current lower pressure system

The current low pressure system is based on a simple design using a water pump to provide flow, a solenoid operated control valve to alter the flow rate in compression experiments, a needle valve to create constant orifice in expansion experiments, a pressure transducer to measure the pressure and a flow meter to measure the change in

volume. Most components were bought off the shelf or acquired through donations. The only customized part is the expansion/compression chamber. The design goals of the current system were robustness, ease of operation and low cost. Unfortunately, the design intent was not fully realized, and there are some disadvantages of the current system. Since the aluminum cap of the chamber is secured by four tie-rods it is time consuming to screw and unscrew the four tie-rod nuts every time an operator wants to place or remove porous inserts. Meanwhile, the diameter of the polycarbonate tube is not wide enough to allow for installation of a spray nozzle, pressure transducer and shop air charging port on the top cap simultaneously. Another problem of the current system is its inability to precisely control the flow rate through a solenoid proportional control valve. Most water proportional control valves work at a certain pressure range and pressure drop, in contrast to the current system's wide pressure range and diminishing pressure drop. The default controller from the factory did not work. A customized control scheme was developed that utilizes a PI controller in MATLAB Simulink to directly drive the solenoid pins on the valve. An op-amp circuit has been developed to amplify a pulse width modulated signal from the DAQ system.

The largest frustration of the current system is the volume measurement. There were three types of volume measurement tools tested: Coriolis flow meter, turbine flow meter and load cell, none of them worked ideally for all of our experiments. The Coriolis meter has an adequate measuring range from 0 to 5GPM but has an approximately 80 ms lag in response time. The turbine meter responds instantly but has a limited measuring range from 0.75GPM to 7.5GPM. In the expansion experiment, the load cell has a good measuring range and rapid response but suffers from large fluctuation in readings due to

the momentum of the impinging water jet entering the measurement volume during rapid expansion. Although solutions were developed for all of the current system's deficiencies, the new system will be operated at much higher pressures (up to 20.7 MPa). If the current design had simply been scaled up, most of the problems would have been aggravated. It became apparent that a total system redesign was necessary.

7.3 New System Design requirements

The fundamental goal of the new system is to achieve more thorough and accurate characterization of the performance of the porous inserts and water spray across a much wider compression/expansion ratio. It was necessary to set some high level design requirements. The compression/expansion chamber would need to withstand 20.7MPa (3000 psi) of cyclically-loaded internal pressure and be resistive to water. Additionally, the system needed to be capable of achieving any compression/expansion ratio between 0 and 200. To simulate the second stage compression process, it is desired that the chamber could be pre-charged with pressurized air up to 6.89 bar (100 psi) before compression. Furthermore, the system should be able to complete a full stroke within 2 seconds. Moreover, an active cooling system with spray nozzle should be able to be integrated with the compression/expansion chamber. Perhaps most critically, the volume measurement should be robust and accurate within financial limitations. Other considerations should include safety, overall cost and ease of use.

7.4 System design and principle:

With the design requirements and experience gained from the low pressure system. A new system is prepared. Flow chart of the proposed new system is demonstrated in figure

7.1, with labeling on each component. During the compression process, a hydraulic oil cylinder is used to drive the rod end of a stainless steel hydraulic water cylinder that is filled with water. This would expel the water into the stainless steel compression/expansion chamber. For the expansion process, pressurized air in the chamber will be allowed to expand and push the liquid in the chamber back into the stainless steel water cylinder. A significant difference of the proposed high pressure system compared to the current lower pressure system is the power source. Instead of a water pump, a hydraulic power unit model number 505.20 from MTS with a working pressure of 21MPa and a maximum flow rate of 20GPM will be used to supply the hydraulic flow.

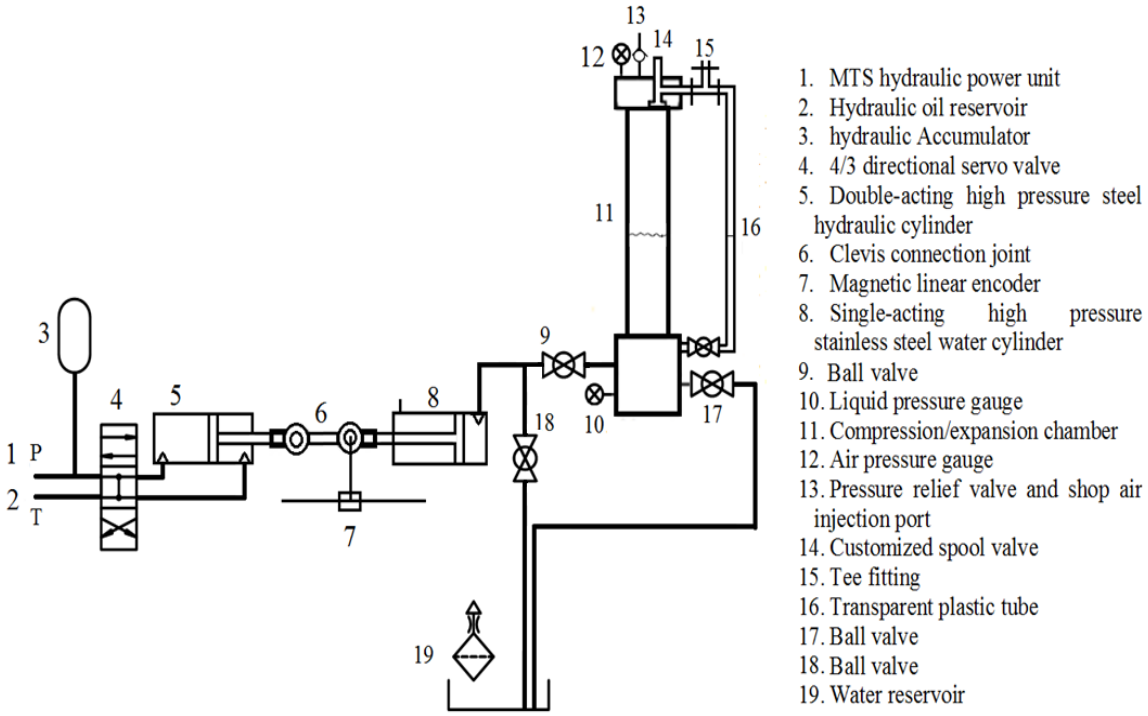

Figure 7.1: Proposed flow circuit of the high pressure compression/expansion system

The power unit feeds into a 4-port, 3-position servo valve that drives a double-acting, high-pressure hydraulic cylinder. A hydraulic accumulator could be installed

between the servo valve and the power supply unit to give a boost in flow rate to allow for higher speed in compression processes. With this configuration, the speed and position of the rod end of the hydraulic cylinder can be controlled. Additionally, another single-acting high pressure stainless steel water cylinder is connected to the rod end of the hydraulic cylinder through a clevis pin joint. The water cylinder will be preloaded with water using the exiting port connected to the base inlet of the customized compression/expansion chamber. Water will be displaced into the chamber as the center rod of the water cylinder is pushed by the hydraulic cylinder rod. In order to measure how much water is ejected into the compression chamber, a linear magnetic encoder will be attached to the rod end of the water cylinder. The location of the rod end will be monitored and digitized so the position of the rod will be recorded. Assuming the stainless steel water cylinder is rigid and water is incompressible, the water volume that exits the cylinder will be a function of the changing position of the rod end and, therefore, will be known. Detailed information about the magnetic encoder will be discussed in a later section of this chapter.

A check valve is placed between the exiting port of the water cylinder and the inlet port of the compression/expansion chamber to avoid backflow of water once the compression process is completed. Air will be compressed and expanded inside the chamber. The design of the chamber is significantly different than the current chamber, as will be discussed in the following section. After the chamber, a ball valve is used to manually control the water return to the water reservoir. Meanwhile, the water cylinder is connected with the water reservoir through another check valve. During the recharging phase of the water cylinder, the servo valve can change the direction of movement of the

hydraulic cylinder and pull the rod of the water cylinder to create low pressure in the water cylinder and draw the water from water reservoir.

7. 5 Design of the high pressure liquid piston chamber

The compression/expansion chamber assembly is the most critical component of the whole system. It was a major technical challenge to design the chamber to meet the performance requirements while staying within the financial constraint. In order to withstand the cyclical 20.7MPa (3000 psi) internal pressure load and meet the corrosion resistance requirement, the chamber material was chosen to be 304-stainless steel. For ease of manufacturing, an off the shelf stainless steel tubing was chosen to be the chamber body. The wall thickness was determined by standard hoop-stress calculations for pressure vessels with a safety factor of 4. In order to install all the necessary equipment on the top cap, a minimum of 7.62mm (3 inches) for the diameter of the tubing was required. The stainless steel tubing is secured by 6 high-strength, threaded steel tie-rods with a stainless steel cap and base shown in figure 7.2.

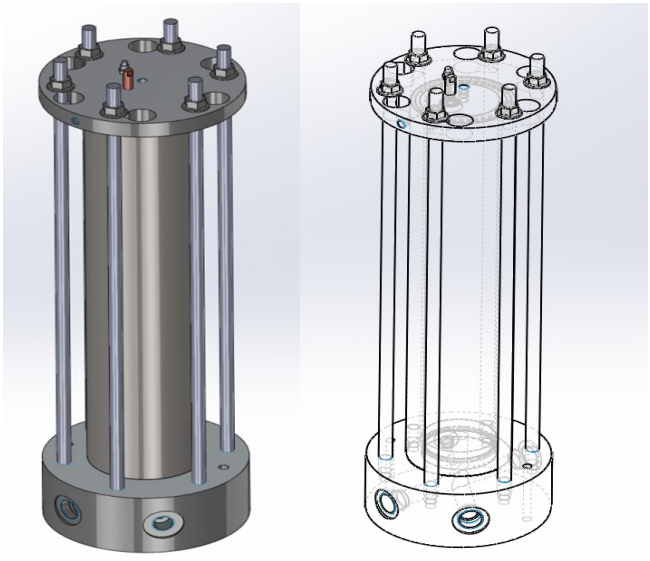

Figure 7.2: 3D model and wireframe sketch of the high pressure compression/expansion chamber. See appendix for detailed drawings

In order to perform efficiency calculations, initial air volume must be known. Unfortunately, since the whole chamber is made out of stainless steel, there is no trivial way for an operator to observe the water level inside the chamber once the cap is closed. Additionally, in order to study a more complete range of compression ratios, an operator should be able to perform a compression process at a variety of initial pressures. Because of this, it was necessary to develop a novel method of pre-charging the chamber while still being able to capture the initial height of the water column. This lead to the design of the most unique component of the chamber, which is the spool valve shown in figure 7.3. The spool valve has a threaded center rod with two O-ring grooves. A primary, high-pressure O-ring is placed in the face seal groove on the base surface of the spool and a smaller, secondary O-ring is put in the side groove in the center rod.

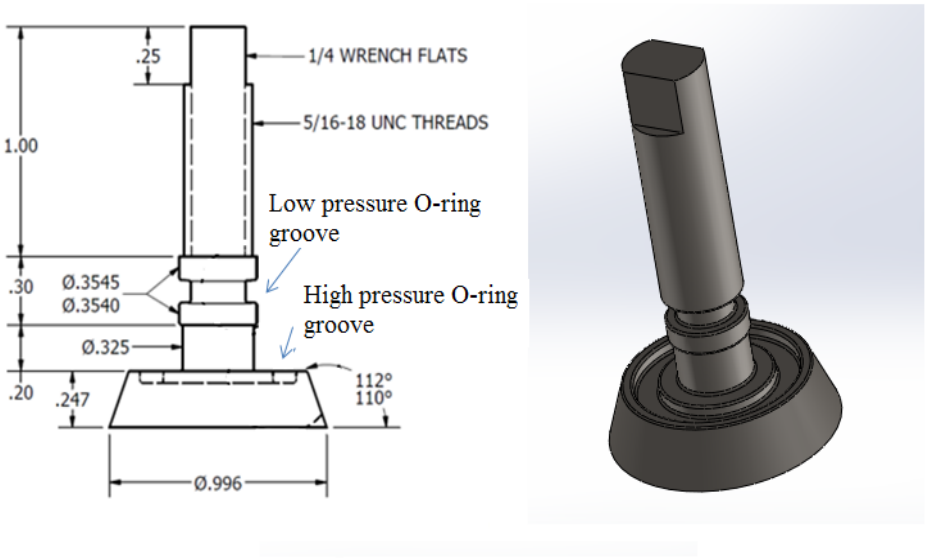

Figure 7.3: wireframe sketch and the 3D image of the customized spool valve (dimensions are in inches)

During the initial charging phase, shown in figure 7.4, the spool valve will be unseated and the high pressure O-ring will be disengaged. This would allow pressurized air from the charging port to flow into the chamber while the secondary O-ring blocks the

air from escaping through the top cap. Meanwhile, a tee will be installed at the charging port and a transparent plastic tube, shown as component # 16 in figure7.1, will connect the tee and a port at the base of the chamber. With this configuration, the pressure inside the plastic tube would be the same as the pressure inside the chamber and the water level inside the chamber would be the same as what is observed through the transparent tube. Knowing the height of the water level could lead to a calculation of initial water volume. The other port on the tee will be served as the pressurized air charging port.

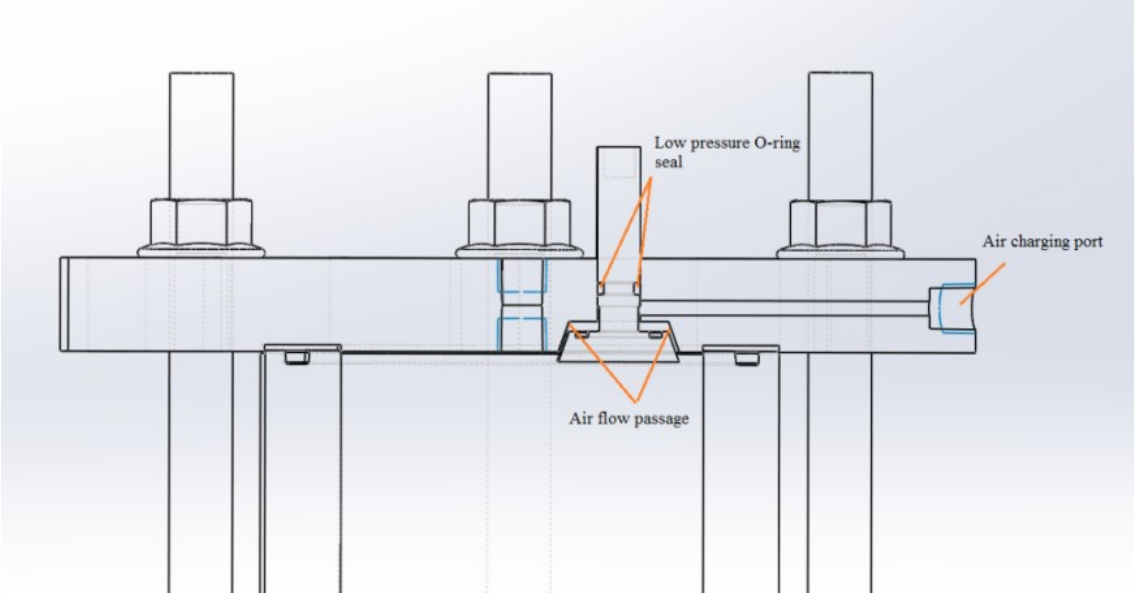

Figure 7.4: A wireframe section view on the top cap showing the position of the spool valve during the initial charging process when it is unseated and the high pressure O-ring seal disengage and allowing charging air flow into the chamber from the air charging port

Once the charging phase is completed, the spool valve will be tightened by a wing nut shown in figure 7.6 and the primary O-ring will engage and seal the top cap shown in figure 7.5. The high pressure O-ring is capable of sealing air up to 5000 psi of internal pressure.

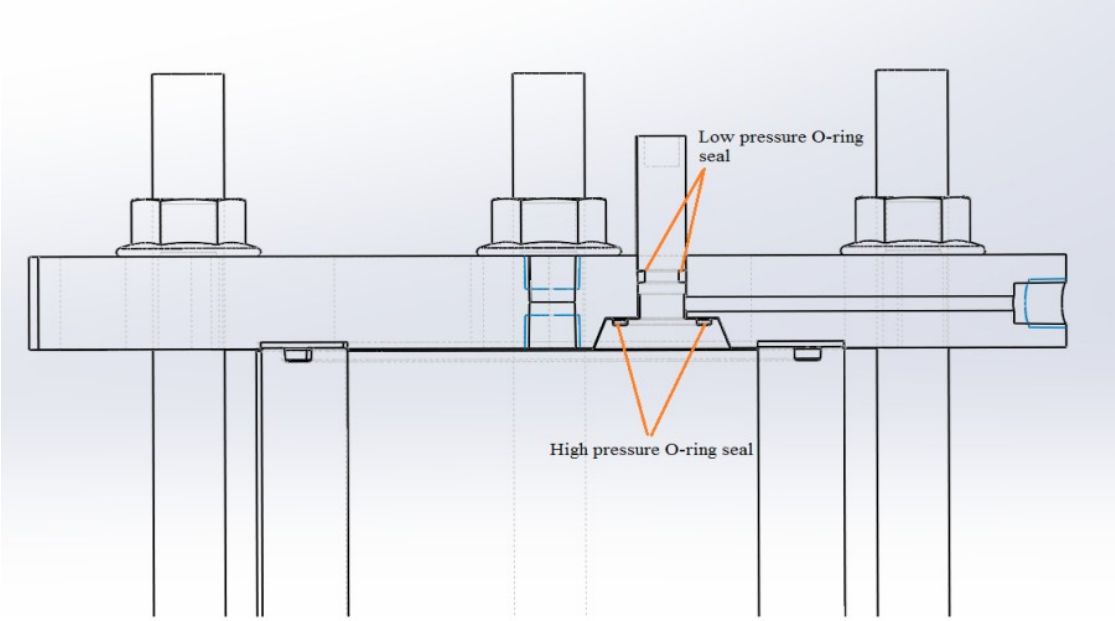

Figure 7.5: A wireframe section view on the top cap showing the position of the spool valve during the compression process when it is seated and secured. High pressure O-ring will seal the top cap avoiding any leakage air

Figure 7.6: Picture of the top cap of the chamber showing the customized spool valve is tightened and secured by a wing nut against the top cap. The cap is secured by tie-rods, hex-nuts and customized dampers.

Meanwhile, in order to improve ease of use, a unique quick-release mechanism is designed for the top cap. Since the chamber is bolted by 6 tie-rods it would be very inefficient to screw/unscrew 6 nuts every time an operator wants to open the cap. In addition to a small through-hole for each tie rod, a larger through-hole for the each hex-nut is drilled and a connected by a passage sweep. If an operator wants to open the top cap, as long as the 6 nuts are slightly loosened, the top cap can be twisted clockwise and the operator can lift the cap, with the tie-rods and the hex-nuts passing through the large through hole.

For detailed engineering drawings and bill of materials please go to Appendix E

7.6 Volume measurement

The largest error source of the low pressure system is the volume measurement. The writer did not have good experience with the both turbine meter and load cell. The new system will be operated at a much higher pressure range and larger flow rate range. The cost of a robust, rapid response and high accuracy flow meter that would work for our operating range would be out of the financial limitation. A new concept of measuring the volume inside the compressor is necessary. Given the fact that the stainless steel hydraulic cylinder displaces liquid volume proportional to the stroke length and the deformation of the cylinder under high pressure is relatively small. A linear encoder, which is a transducer paired with a scale that encodes position can be used to monitor the position of the cylinder rod. A Magnetic Linear Encoder v1.2 made by MakerBot® is selected due to its high resolution, down to 15 microns, and rapid sampling frequency of 57 kHz. The encoder will be attached at the clevis rod end of the stainless steel cylinder and a sliding rail glued with magnetic linear tape will be installed in parallel beside the

cylinder allowing the encoder to slide freely along with the movement of the cylinder rod. With this tool and careful calibration, the uncertainties in volume measurement would be reduced dramatically.

7.7 High pressure system design summary

The purpose of Chapter 7 is to summarize what we have learnt from the low pressure compression/expansion system and describe the design process for a high pressure compression/expansion system. The new system will allow much greater pressures, have an improved volume measurement method, provide smoother control of flow rate and a much greater range of compression/expansion ratios, accommodate an additional active cooling system with spray nozzle, and offer greater ease of use. Such improvements in capabilities would allow for more thorough and accurate characterizations of the performance of both the porous inserts and the spray cooling through a wider and more realistic range of power densities.

Reference:

[1] US Energy Information Administration, Electric Power Monthly, January 2013.

[2] American Wind Energy Association, Fourth Quarter 2012 Market Report, January 2013

[3] DOE. 20% wind energy by 2030. Washington, D.C.: Department of Energy; 2008.

[4] Electric Reliability Council of Texas (ERCOT), News Release, March 2013.

[5] Green, J., Bowen, A., Fingersh, L. J., and Wan, Y., "Electrical Collection and Transmission for Offshore Wind Power," National Renewable Energy Laboratory Report NREL/CP-500-41135, 2007

[6] K.C. Divya, Jacob Østergaard, Battery energy storage technology for power systems—An overview, Electric Power Systems Research, Volume 79, Issue 4, April 2009

[7] Kyle Bradbury. Energy Storage Technology Review. Technical report, Duke University, 2010

[8] Haisheng Chen, Thang Ngoc Cong, Wei Yang, Chunqing Tan, Yongliang Li, Yulong Ding, Progress in electrical energy storage system: A critical review, Progress in Natural Science, Volume 19, Issue 3, 10 March 2009

[9] Ioannis Hadjipaschalis, Andreas Poullikkas, and Venizelos Efthimiou. Overview of current and future energy storage technologies for electric power applications. Renewable and Sustainable Energy Reviews, 13.6 (2009):1513-1522.

[10] Belén Zalba, José Ma Marín, Luisa F. Cabeza, Harald Mehling, Review on

thermal energy storage with phase change: materials, heat transfer analysis and applications, Applied Thermal Engineering, Volume 23, Issue 3, February 2003

[11] K.C. Divya and Jacob Ostergaard. Battery energy storage technology for power systems and overview. Electric Power Systems Research, 79.4 (2009): 511-520.

[12] P. Y. Li, E. Loth, T. W. Simon, J. D. Van de Ven, and S. E. Crane, "Compressed Air Energy Storage for Offshore Wind Turbines," 2011 International Fluid Power Exhibition (IFPE), Las Vegas, NV, March, 2011

[13] NREL, wind powering America; 2008. Available from: http://www.eere. energy.gov/windandhydro/windpoweringamerica/wind_maps.asp.

[14] Vattenfall. Horns rev offshore wind farm. Available from: http://www.power-technology.com/projects/hornsreefwind/

[15] Junginger, Martin, André Faaij, and Wim C. Turkenburg. "Cost reduction prospects for offshore wind farms." Wind engineering 28.1 (2004): 97-118

[16] J. Jonkman, S. Butterfield, W. Musial, G. Scott Definition of a 5-MW reference wind turbine for offshore system development NREL/TP-500-38060 National Renewable Energy Laboratory, Golden, CO (2007)

[17] "Snyder, Brian, and Mark J. Kaiser. "Ecological and economic cost-benefit analysis of offshore wind energy." Renewable Energy 34.6 (2009): 1567-1578.

[18] "Offshore Wind Energy: Ready to Power a Sustainable Europe, Final Report", Concerted Action on Offshore Wind Energy in Europe, December 2001, NNE5-1999-562.

[19] Saadat, M.; Li, P.Y. "Modeling and control of a novel compressed air energy storage system for offshore wind turbine", American Control Conference (ACC), 2012, On page(s): 3032 - 3037, Volume: Issue: , 27-29 June 2012

[20] F. Shirazi, M. Saadat, B. Yan, P.Y. Li and T. W. Simon, "Iterative Optimal and Adaptive Control of a Near Isothermal Liquid Piston Air Compressor in a Compressed Air Energy Storage System", 2013 ACC IEEE Control System Society Conference, Paper No.1702, Washington D.C., June 2013.

[21] Andrew Rice, Heat transfer enhancement in a cylindrical compression chamber by way of porous inserts and the optimization of compression and expansion trajectories for varying heat transfer capabilities. Master's thesis, University of Minnesota, December 2011.

[22] P. Y. Li, J. D. Van de Ven and C. Sancken, "Open Accumulator Concept for Compact Fluid Power Energy Storage", ASME-IMECE 2007-42580, Seattle, WA, November, 2007.

[23] Parker Hannifin Corp. Hydraulic Accumulators Introduction. Catalog HY10-1630/US.2003

[24] David Hafvenstein. Thermodynamics and heat transfer models of an open accumulator. Master's thesis, University of Minnesota, December 2009.

[25] Humphrey H.A. An internal-combustion pump and other applications of a new principle. Proc Inst Mech Eng 1909;1123.

[26] Spencer LC. A comprehensive review of small solar-powered heat engines. Part I. A history of solar powered devices up to 1950. Sol Energy 1989;43(4):191–6.

[27] Agustín M. Delgado-Torres, Solar thermal heat engines for water pumping: An

update, Renewable and Sustainable Energy Reviews, Volume 13, Issue 2, February 2009, Pages 462-472

[28] James D. Van de Ven, Perry Y. Li, Liquid piston gas compression, Applied Energy, Volume 86, Issue 10, October 2009

[29] Heywood JB. Internal combustion engine fundamentals. New York: McGraw-Hill, Inc.; 1988.

[30] Gary Borman, Kazuie Nishiwaki, Internal-combustion engine heat transfer, Progress in Energy and Combustion Science, Volume 13, Issue 1, 1987

[31] Kornhauser AA. Gas-wall heat transfer during compression and expansion. PhD thesis, Massachusetts Institute of Technology, Cambridge, MA; 1989.

[32] Wong, Lak Kin. Computational Fluid Dynamics Analysis on the Liquid Piston Gas Compression. Master's thesis. WORCESTER POLYTECHNIC INSTITUTE, 2011.

[33] Taylor, G, "The Instability of Liquid Surfaces when Accelerated in a Direction Perpendicular to their Planes. I," Proceedings of the Royal Society of London. Series A, Mathematical and Physical Sciences, Vol. 201, No. 1065, 1950, pp. 192-196.

[34] Lewis, D.J., "The Instability of Liquid Surfaces when Accelerated in a Direction Perpendicular to their Planes. II," Proceedings of the Royal Society of London. Series A, Mathematical and Physical Sciences, Vol. 202, No. 1068, 1950, pp. 81-96

[35] J.M. Zhang, W.H. Sutton, F.C. Lai, Enhancement of heat transfer using porous convection-to-radiation converter for laminar flow in a circular duct, International

Journal of Heat and Mass Transfer, Volume 40, Issue 1, October 1996, Pages 39-48

[36] Lu, T. J., A. G. Evans, and J. W. Hutchinson. "The effects of material properties on heat dissipation in high power electronics." Journal of Electronic Packaging, 120 (1998): 280.

[37] K.C. Leong, L.W. Jin, Characteristics of oscillating flow through a channel filled with open-cell metal foam, International Journal of Heat and Fluid Flow, Volume 27, Issue 1, February 2006

[38] ERG Aerospace Corp. "Duocel® Aluminum Foam." Web http://www.ergaerospace.com/Aluminum-properties.htm, July 2013.

[39] R Tew, M Ibrahim, D. Danila, T. Simon, S. Mantell, L. Sum, D. Gedeon, K. Kelly, J. Mclean, G. Wood, and S. Qiu, "A Microfabricated Involute-Foil Regenerator Stirling Engines," NASA/CR –2009-215516, June 2009

[40] L Sun, T.W.Simon, S.C. mantel, M. B. Ibrahim, D. Gedeon and R. Tew, "Thermo-fluid Experiments Supporting Microfabricated Regenerator Development for a Stirling Space Power Engine," AIAA 2009-4579, 7th International Energy Conversion Engineering Conference, Denver, Colorado, Aug 2009.

[41] C. Zhang, F.A. Shirazi, B. Yan, T. W. Simon, P. Y. Li, and J, Van de Ven, "Design of an interrupted-plate heat exchanger used in a liquid-piston compression chamber for compressed air energy storage". Paper #17484, ASME 2013 Summer Heat Transfer Conference. Minneapolis

[42] Robert H. Perry and Donald W. Green, editors. Perry's Chemical Handbook for

Engineer's. McGraw-Hill, 1984.

[43] C. Zhang, T. W. Simon and P. Y. Li, "Storage Power and Efficiency Analysis Based on CFD for Air Compressors used for Compressed Air Energy Storage", ASME IMECE, Paper #88985 Houston TX, November, 2012.

[44] G. Borman and K. Nishiwaki. Internal-combustion engine heat transfer. Prog. Energy Combust. Sci., 13(1):1-46, 1987

[45] J.P Holman, Heat transfer, Tenth edition, McGraw-Hill, 2010

[46] C. Zhang, J.H. Wieberdink, F.A Shirazi, B. Yan, T. W. Simon and P. Y. Li, "numerical investigation of Metal-Foam filled liquid piston compressor using a two energy equation formulation based on experimentally validated models", Paper# 63854, proceeding of the 2013 ASME IMECE

[47] Henry, William. "Experiments on the quantity of gases absorbed by water, at different temperatures, and under different pressures." Philosophical Transactions of the Royal Society of London 93 (1803): 29-276.

[48] R. Sander, " Henry's Law Constants " in NIST Chemistry WebBook, NIST Standard Reference Database Number 69, Eds. P.J. Linstrom and W.G. Mallard, National Institute of Standards and Technology, Gaithersburg MD, 20899, http://webbook.nist.gov

[49] Han, P., and D. M. Bartels. 1996. Temperature dependence of oxygen diffusion in H2O and D2O. J. Phys. Chem. 100:5597-5602.

[50] Cussler, E. L. 1984. Diffusion - mass transfer in fluid systems. Cambridge University Press, Cambridge, United Kingdom.

[51] Kline, S. J., and F. A. McClintock: "Describing Uncertainties in Single-Sample

Experiments", Mech. Eng., p. 3, January 1953

[52] Chao Qin, Eric Loth, Perry Y. Li, Terrence W. Simon and James Van de Ven. “Spray-Cooling for Wind-based Compressed Air Energy Storage.’’ 10.2514/6.2013-3870, International Energy Conversion Engineering Conference. 2013

Appendix A

Nomenclatures

English letter symbols:

A	Total heat transfer surface area inside the liquid piston
A_{avg}	Average heat transfer surface area during a compression/expansion process
A_{insert}	Total heat transfer surface area of a the inserts placed in the liquid piton
A_{wall}	Total liquid piston wall area
Bi	Biot number
c_v	Specific heat of air at constant volume in mass basis
CF	Correction factor used for correcting the volume measurement by turbine meter
d	Diameter of the polycarbonate cylinder
dT	Differential of bulk air temperature during compression/expansion
dV	Different of air volume during compression/expansion
du	Differential of specific internal energy
dU	Differential of internal energy
dU_{air}	Differential of internal energy of air
E_p	Potential energy stored inside the final compressed air product
h	Heat transfer coefficient between air and heat sink/source
k	Thermal conductivity
k_H	Henry's constant
L_c	Characteristic length of the insert

m	Mass
m_{air}	Mass of air
n	Quantity of air in moles
P	Pressure of air inside the liquid piston chamber
P_0	Initial pressure
P_c	Pressure of air when reaches compression ratio of 10
P_{eq}	Pressure of air when air reaches thermal equilibrium
$P(t)$	Instantaneous pressure of air inside the chamber
r	Compression/expansion ratio
R	Universal gas constant
R_{air}	Gas constant for air
S	Specific surface area
t	Time
t_c	Compression time
t_e	Expansion time
T	Bulk temperature of the air inside the liquid piston
T_0	Initial temperature
T_c	Bulk temperature of air at the end of compression before isobaric cooling
T_e	Bulk temperature of air at the end of expansion before isobaric heating
T_{eq}	Bulk temperature of air when air reaches thermal equilibrium
T_{source}	Temperature of heat source
T_{sink}	Temperature of heat sink
$\dot{T}$	Temperature rate of change

u	Specific internal energy
U	Internal energy
U_{air}	Internal energy of air
V	Air volume
V_{adi}	Volume trajectory of an adiabatic expansion
V_{exit}	Volume of liquid that exited the expansion chamber after an expansion process
$\dot{V}$	Volume rate of change
V_0	Initial air volume
V_p	Volume of porous inserts
V_f	Finial air volume after compression/expansion
V_T	Total amount of liquid added into the chamber measured by the turbine meter
W_{in}	Input work during compression process
W_{out}	Work output during expansion process
Z	Compressibility factor

Greek letter symbols

$\delta Q_{air\ to\ sink}$	Infinitesimal heat transfer between air and heat sink
$\delta Q_{source\ to\ air}$	Infinitesimal heat transfer between air and heat source
ΔP	Finite change in pressure
ΔT	Finite change in bulk temperature of air
ζ_c	Pressure volume trajectory for a compression process
ζ_e	Pressure volume trajectory for an expansion process
η_c	Compression efficiency
η_e	Expansion efficiency
ρ	Density of air
ρ_c	Power density for compression process
ρ_e	Power density for an expansion process
$\emptyset$	Porosity of the insert

Appendix B

Apparatus details

Water is drawn from and returned to a plastic bucket. The pump is from Wanner Engineering, Inc, D-10-I series Hydra-Cell positive displacement diaphragm pump. The maximum flow rate is 0.25L/s (4 gpm) and maximum output pressure is 6.9Mpa (1000psi). The pump is driven by a 1.5hp Dayton 3N550 electric motor. The pressure relief valve is a Danfoss Power Pack Valve type VPH 15E and cracking pressure is set to 1.1Mpa (160psi).

The liquid flow into the compression chamber is controlled by a Bűrkert Type 6223 proportional solenoid control valve. The valve's pressure rating is from 50 kPa to 1MPa (7 to 145 psi). Although the testing condition is slightly above the pressure range, no leakage is found during the testing. The valve is directly connected to the DAQ board, and an op-amp circuit. The 0-5V signal from the DAQ board is amplified to drive the solenoid in the valve and the valve is supposed to respond to the 0-5 volt signal. However, the valve's response is either fully open or fully closed. The reason remains unknown. Then another control scheme is designed for the valve. By opening and closing the valve swiftly, the flow rate can be varied and the upstream pressure is used as a feedback to control the frequency of opening and closing the valve. The calibration curve for the valve under a constant upstream pressure and the corresponding flow rate is shown in figure B.1. This curve is used to estimate the required upstream pressure threshold to achieve a certain flow rate and hence compression time.

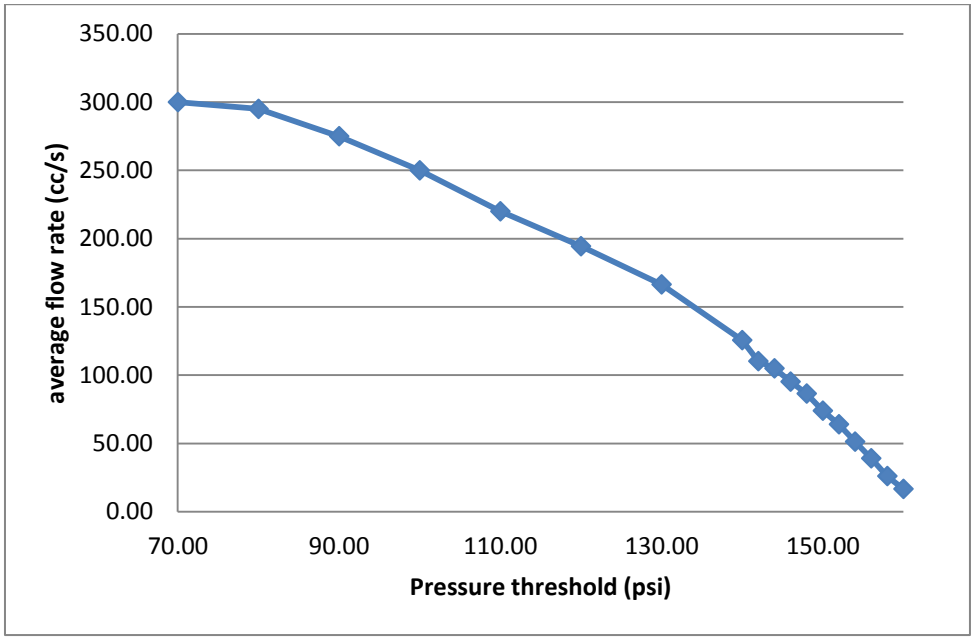

Figure B.1. Calibration curve for the control valve at constant upstream pressure vs. averaged flow rate

The pressure sensor used in this study is the Kulite ETM-375 diaphragm pressure transducer with a piezoresistive material as sensing element. The output is voltage from 0 to 5 volts with a corresponding to absolute pressure range of 0 to 72 MPa (0 to250 psi). The accuracy of the pressure sensor is 0.1% of the full range which is ±0.25 psi. The flow meter used in this study is an Omega FTB-1412 turbine flow meter. The measuring range of the meter is 2.8 to 28 LPM (0.75 to 7.5GPM). Fluid entering the meter first passes through an inlet flow straightener to reduce the turbulent flow patter. Then fluid passes through the turbine, causing the turbine to spin at a speed proportional to the fluid flow rate. As each turbine blade passes through the magnetic field generated by the meters magnetic pickup, an AC voltage pulse is generated and sent to the DAQ system. The frequency of the pulses is proportional to the volumetric flow rate. A customized counter

is developed is Matlab to count and the total number of pulses generated and the frequency of the pulses. The accuracy of the meter is ±1% of the reading.

Appendix C

Sample data processing and efficiency calculation

C.1 Compression experiments without insert

The data processing starts with acquiring air pressure measurement and liquid volume that exits the pressure chamber. The raw pressure measurement is shown in figure C.1. As the readers may notice, the noise level of the pressure measurement is quite substantial. A built-in Matlab function "smooth" is used to filter the raw data. This filter is using 100 data points moving average with zero phase lag.

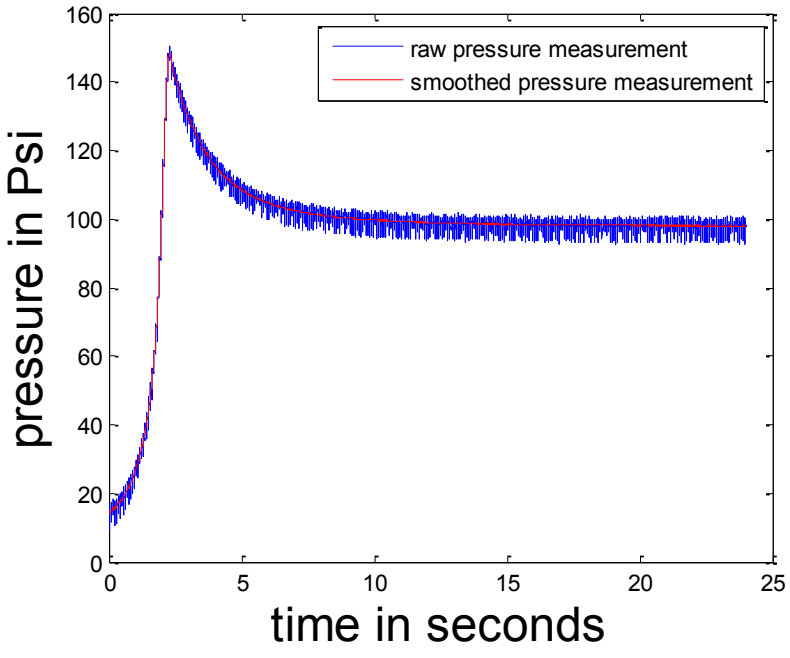

Figure C.1. Raw pressure measurement and filtered pressure measurement vs. time for a compression process without inserts.

The raw volume measurement signal is the voltage pulse generated by the spinning water turbine. The total amount of liquid passing the turbine is proportional to the number of pulses generated. The conversion factor, from the factory calibration

curve, is 2810 pulses per liter. The raw signal of the voltage pulse and the corresponding cumulative volume are plotted in C.2.(a) and (b). Where in C.2(a) is for an overall compression process and isochoric cooling and C.2.(b) is the zoomed-in version at the beginning of the compression process.

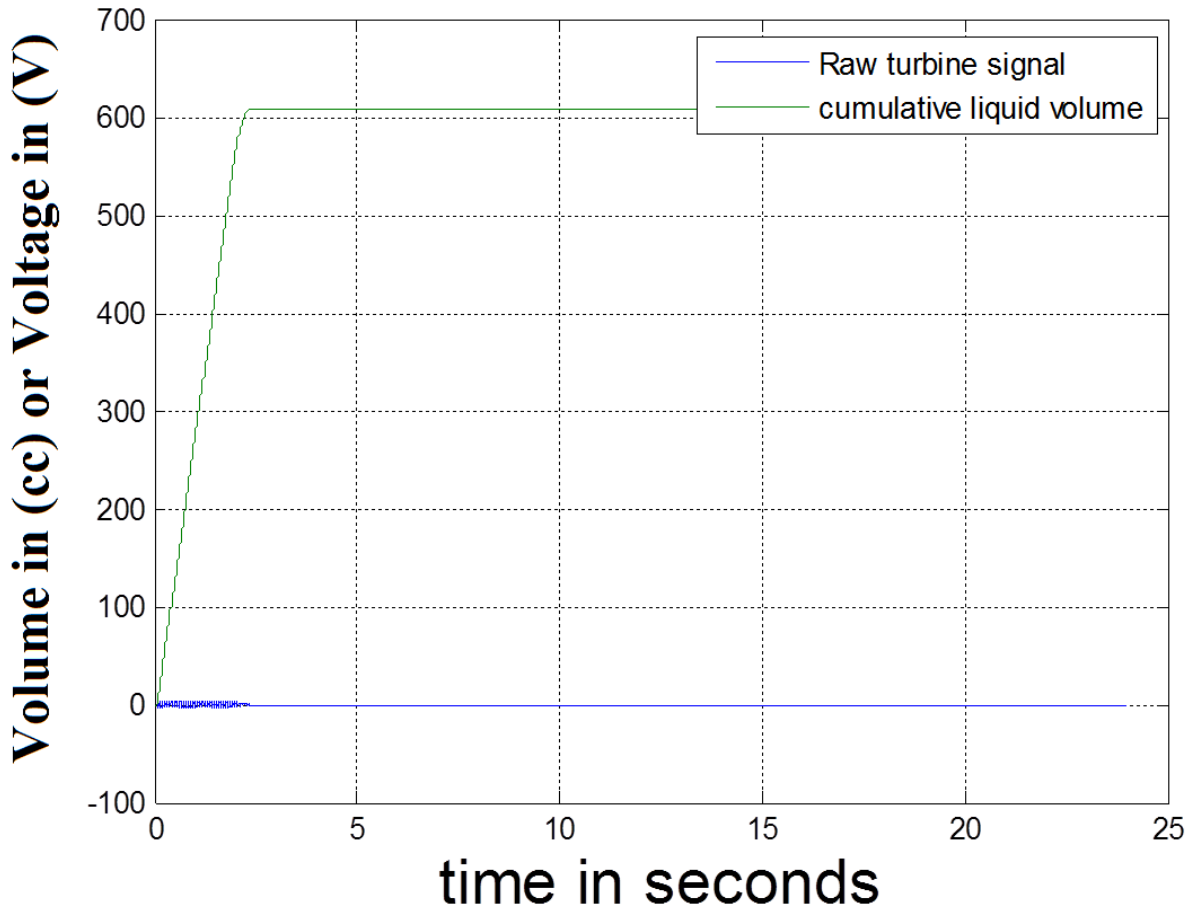

Figure C.2 (a). Raw turbine signal and cumulative liquid volume profile vs. time for a compression process

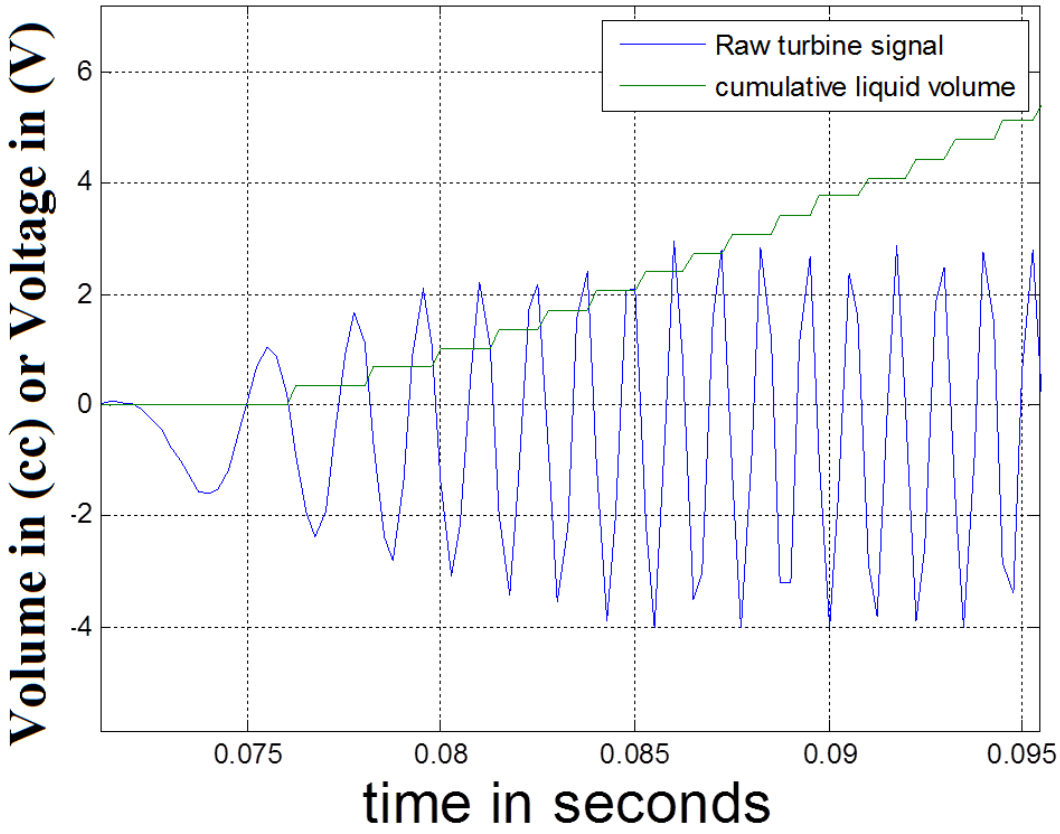

Figure C.2 (b). A zoomed-in raw turbine signal and cumulative liquid volume profile vs. time

Once the exit liquid volume profile is acquired, the air volume can be calculated assuming the pressure chamber is rigid and initial air volume is 715 cc. Since this study only focuses on the compression/expansion process. All the pressure and volume data are all processed up to compression ratio of 10 and expansion ratio of 6. The calculated air volume up to compression ratio of 10 is shown in figure C.3. The corresponding pressure profile is shown in figure C.4.

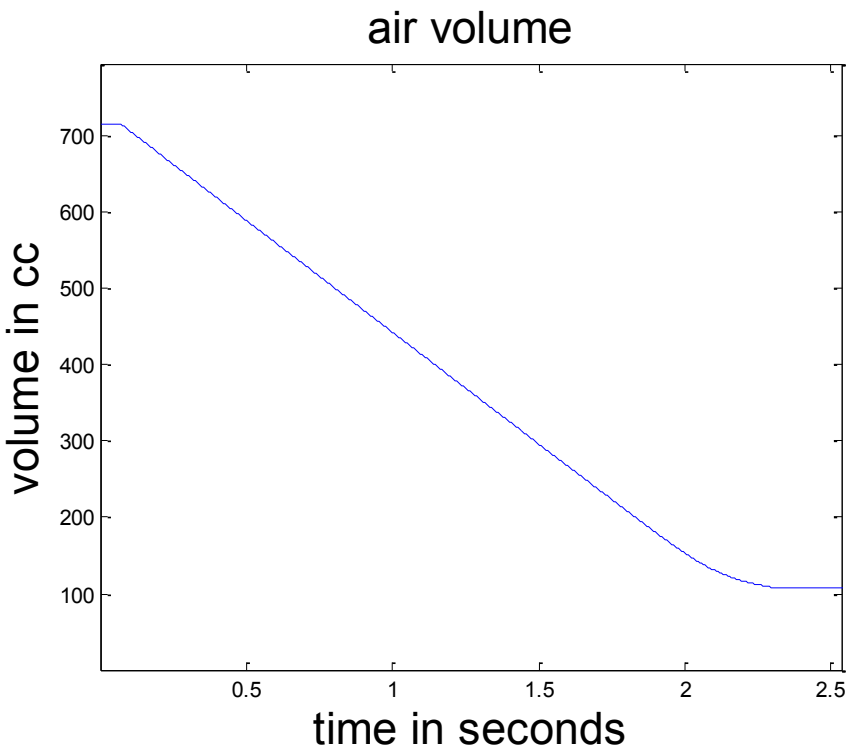

Figure C.3. Sample Air volume profile for a compression process with a compression ratio of 10

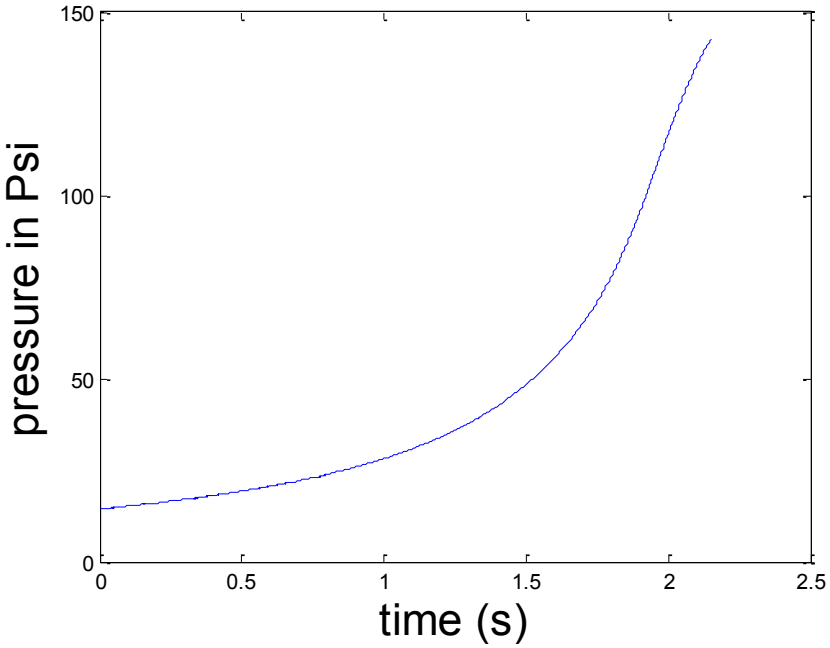

Figure C.4. Sample pressure profile for a compression process with a compression ratio of 10

Because the volume measurement by turbine meter is not accurate enough, it must be corrected using a correction factor CF:

$$CF = \frac{V_0 - V_f}{V_T} \tag{3.3}$$

Where:

$V_0 = 715\ cc$ is the initial air volume as measured by a graduated cylinder

$V_T = 632cc$ is the total amount of liquid added into the chamber as measured by the turbine meter

V_f is the final volume after compression and can be calculated using equilibrium concept introduced in Chapter 3 and Chapter 4:

$$\frac{T_{eq}}{P_{eq}V_{eq}} = \frac{T_o}{P_0V_0} \tag{3.4}$$

$$V_{eq} = V_f = \frac{T_{eq}}{P_{eq}\frac{T_0}{P_0V_0}} = \frac{\mathrm{P_0V_0}}{\mathrm{P_{eq}}} = 104\ \mathrm{cc} \tag{3.5}$$

With the calculated $V_0, V_t\ and\ V_{eq}$, correction factor CF can be calculated:

$$CF = \frac{V_0 - V_f}{V_T} = \frac{715 - 104}{632} = 0.967 \tag{3.3}$$

This correction factor is used by multiplying with the raw volume profile to get the corrected volume profile. With the pressure and volume vs. time profile, the PV trajectory for compression can be obtained. In figure C.5, the pressure-volume trajectory of a sample compression process with a compression ratio of 10 is plotted against the isothermal and adiabatic compression process.

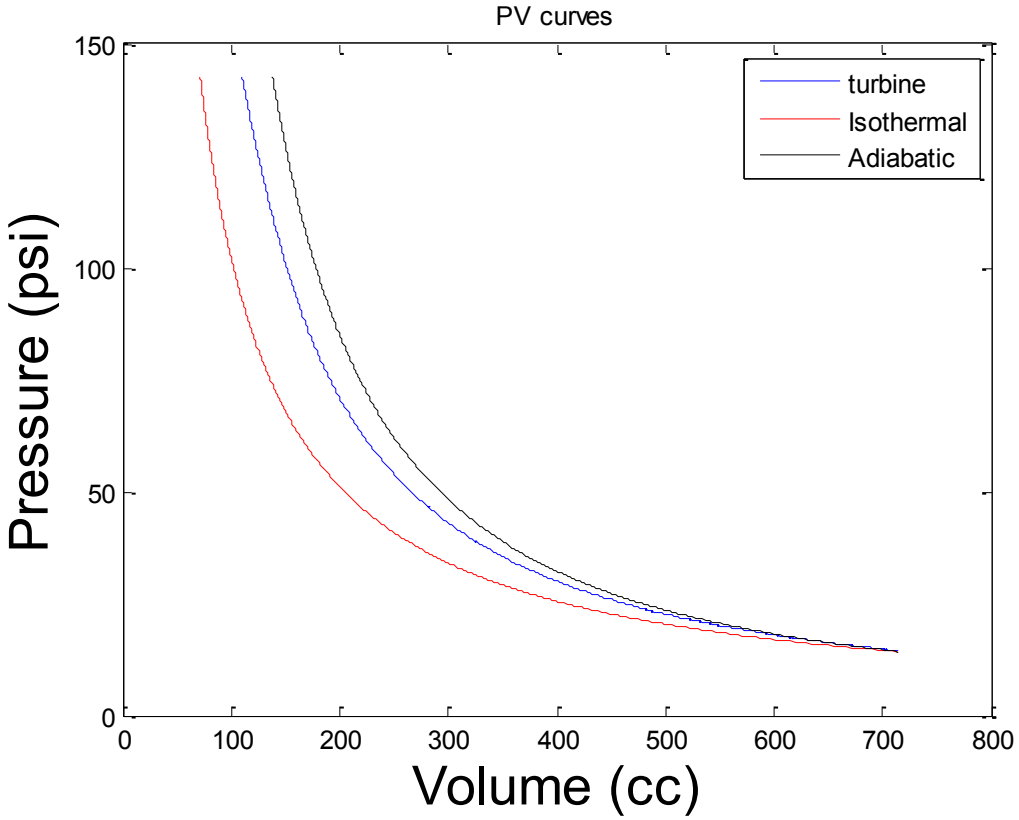

Figure C.5. Sample pressure volume trajectory profile for a compression process with a compression ratio of 10

With the pressure volume trajectory profile, the total amount of work input total potential energy stored and compression efficiency can be calculated using equation 2.3, 2.4, 2.5.

$$W_{in} = \int_{v_0}^{v_c} (P(t) - P_0)dV + \left(1 - \frac{1}{r}\right)(P_c V_C - P_0 V_0) + (P_c - P_0)V_{iso} \tag{2.3}$$

$$E_P = nRT_0\left[\ln(r) + \frac{1}{r} - 1\right] + (P_c - P_0)V_{iso} \tag{2.4}$$

$$\eta_c = \frac{E_P}{W_{in}} = \frac{nRT_0\left[\ln(r) + \frac{1}{r} - 1\right] + (P_c - P_0)V_{iso}}{\int_{v_0}^{v_c}(P(t) - P_0)dV + \left(1 - \frac{1}{r}\right)(P_c V_C - P_0 V_0) + (P_c - P_0)V_s} \tag{2.5}$$

The integral of $\int_{V_0}^{V_c}(P(t)-P_0)dV$ can be calculated through "*trapz*" a built-in integral function in Matlab, with $r = 10$, $P_0 = 9.8319\,x10^4$ Pa, $V_0 = 715x10^{-6}m^3$, $V_c = 109.6x10^{-6}m^3$, $V_{iso} = 71.5x10^{-6}m^3$. Corresponding values are W_{in}=207.05 J, E_P =161.9 J and efficiency η_c=78.18%. With the calculated energy stored, E_P, total compression time, t_c, and the given volume of the compression chamber, V_0, the power density, ρ_c, can be calculated using equation 2.6

$$\rho_c = \frac{E_P}{t_c V_0} = \frac{161.9J}{2.15s*715cc} = 105kW/m^3 \qquad (2.6)$$

C.2 Compression experiments with insert

The data processing for cases with insert are very similar to the cases without inserts. The follow section presents a sample data processing procedure and results for a compression process with a constant flow rate, a pressure ratio of 10 and a compression time of 2.3 seconds with porous inserts of 5mm interrupted plates (same testing condition as the previous case without inserts). Starting with raw pressure measurement and smoothed pressure measurement shown in figure C.6.

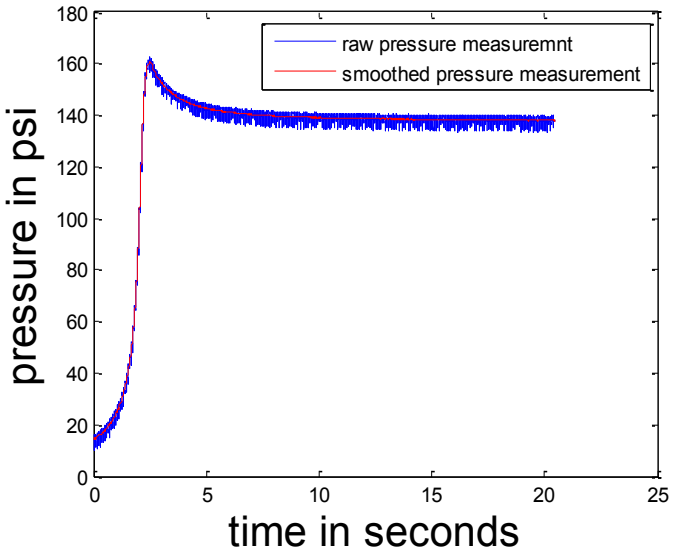

Figure C.6.: Raw pressure measurement and filtered pressure measurement vs. time for a compression process with 5mm interrupted plates

The calculated air volume up to compression ratio of 10 using the same equilibrium pressure method and equation 3.3, 3.4, 3.5 is shown in figure C.7. Keep in mind that due to the presence of the insert, the initial volume of the air is no longer 715cc. For this case, the initial volume is 644cc (the volume of 5mm interrupted plate insert is 71cc). The corresponding pressure profile is shown in figure C.8.

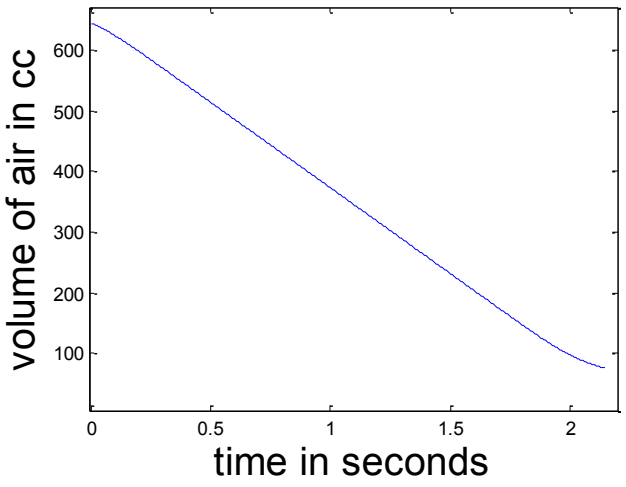

Figure C.7. Sample Air volume profile for a compression process with 5mm interrupted plates insert, under a constant flow rate, a compression ratio of 10 and a compression time of 2.3 sec

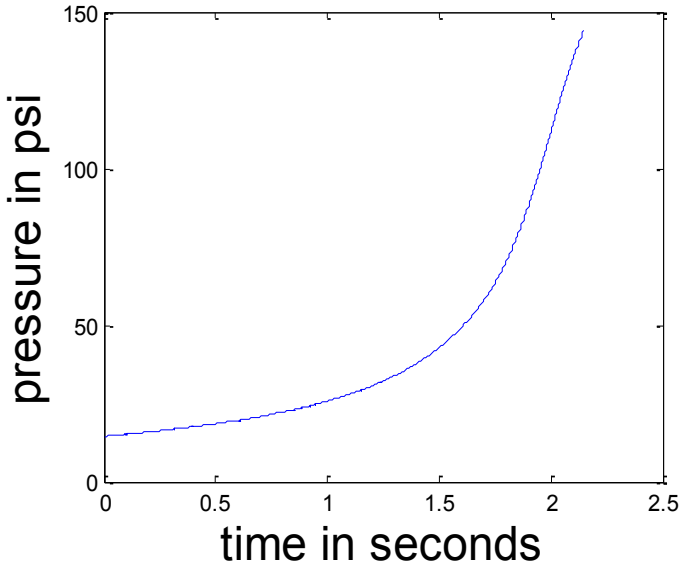

Figure C.8. Sample pressure profile for a compression process with 5mm interrupted plates insert, under a constant flow rate, a compression ratio of 10 and a compression time of 2.3 sec

With the pressure and volume vs. time profile, the PV trajectory for the compression can be obtained. In figure C.9 PV trajectory is plotted against the isothermal and adiabatic compression process. Compared to the previous case without insert, the PV trajectory is much closer to the isothermal compression line.

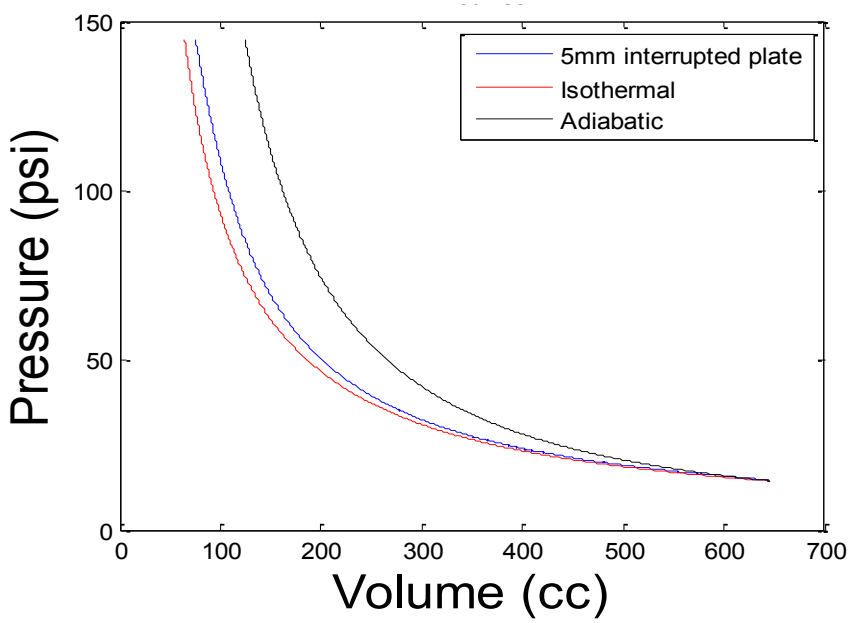

Figure C.9. Sample pressure volume trajectory profile for a compression process with 5mm interrupted plates and a compression ratio of 10

Total amount of work input total potential energy stored and compression efficiency can be calculated using equation 2.3, 2.4, 2.5. For this case, $r = 10$, $P_0 = 9.95\,x10^4$ Pa, $V_0 = 644x10^{-6}m^3$, $V_c = 75.5x10^{-6}m^3$, $V_{iso} = 64.4x10^{-6}m^3$, $t_c = 2.15s$. The corresponding W_{in}=160.2 J, E_P =147.7 J and efficiency η_c=92.2%. With the calculated energy stored, E_P, total compression time, t_c, and the given volume of the compression chamber, V_0, the power density, ρ_c, can be calculated using equation 2.6

$$\rho_c = \frac{E_P}{t_c V_0} = \frac{147.7}{2.15s*715cc} = 96kW/m^3 \qquad (2.6)$$

It seems the presence of the porous inserts slightly decreased the power density of the compressor (96 kW/m^3 compared to 105 kW/m^3) under the similar testing conditions. The decrease in power density is due to the reduced initial air volume that occupied by

the insert. However, the increase in efficiency is significant. For the compression efficiency is increased from 78% to 92%. The best performing insert is the 40ppi metal foam which increases the compression efficiency up to 96% under the same testing conditions.

C.3 Expansion experiments

In this section, a sample data process is presented for an expansion process with 2.5mm interrupted inserts and a pressure ratio of 6. Similar to the data processing in compression experiments, the pressure profile is also acquired first and then filtered using the same smooth function. The raw pressure profile and the smoothed profile is shown in figure

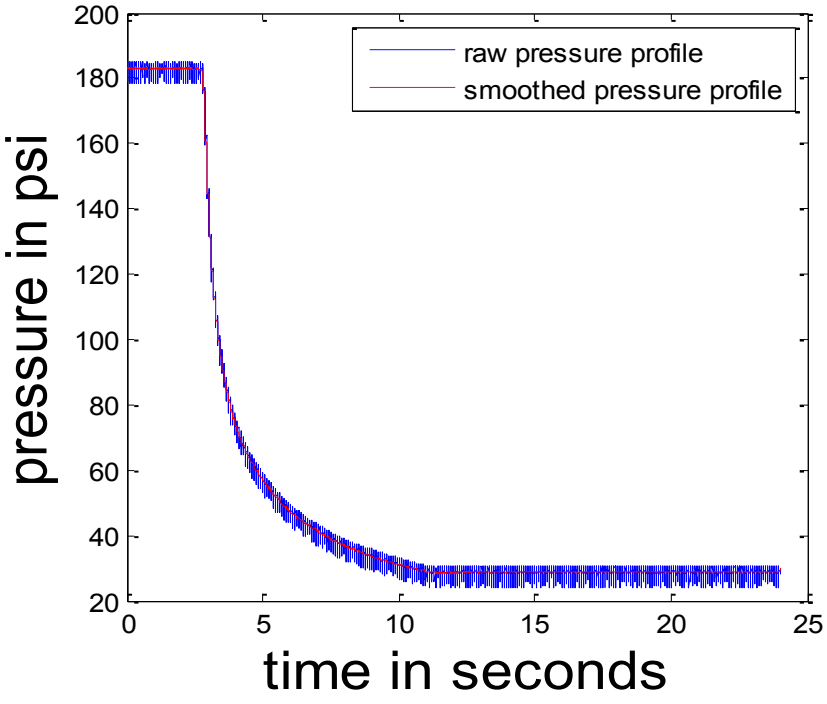

Figure C.10. Raw pressure measurement and filtered pressure measurement vs. time for an expansion process with 5mm interrupted plates

The calculated air volume up to expansion ratio of 6, using load cell volume measurement and assuming the initial trajectory is adiabatic using equation 4.1 is shown in figure C.11. The corresponding pressure profile is shown in figure C.12. In this case, initial volume, V_0, is 95.8 cc and initial pressure, P_0, is 12.6 bar (183 psi), expansion time, t_e is 7.42 seconds. For the cases shorter than 4 seconds, turbine meter is used for volume measurement

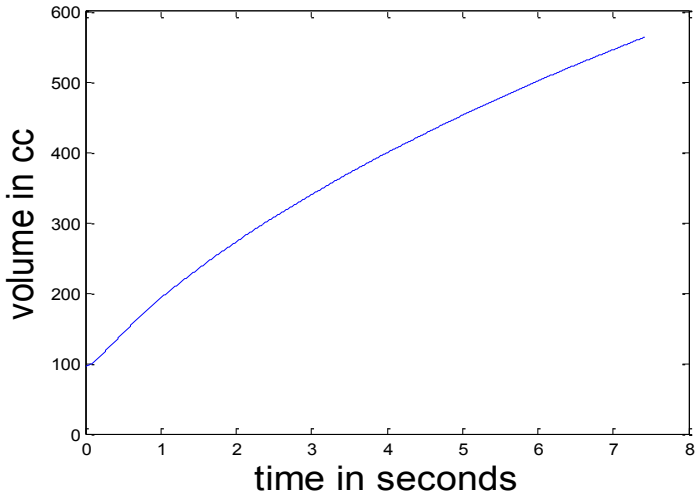

Figure C.11. Sample Air volume profile for an expansion process with 2.5mm interrupted plates insert and an expansion ratio of 6. The volume trajectory is determined by a constant orifice.

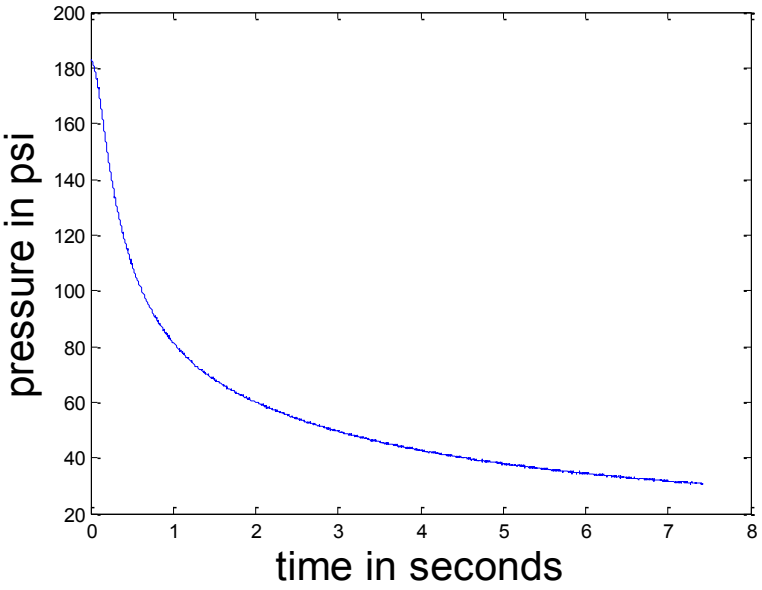

Figure C.12. Sample pressure profile for an expansion process with 2.5mm interrupted plates insert and an expansion ratio of 6

As the reader may notice that the slope of the volume profile is not a constant. The corresponding flow rate is shown in figure C.13. The flow rate decreases as pressure decrease during the expansion process. For this particular case, the number of turns on the needle valve is three.

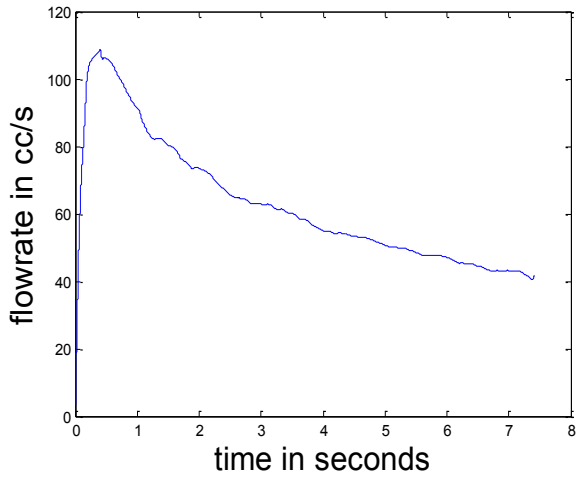

Figure C.13. Sample flow rate profile for an expansion process with 2.5mm interrupted plates insert and an expansion time of 7.4 seconds

With the pressure and volume vs. time profile, the PV trajectory for the expansion process can be obtained. In figure C.14 PV trajectory is plotted against the isothermal and adiabatic compression process, it suggests that at the beginning the experiments,

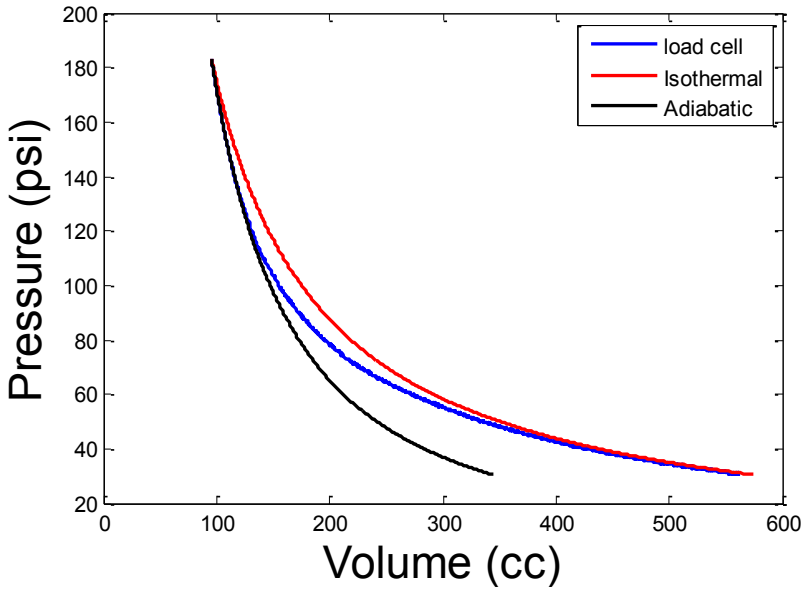

Figure C.14. Sample PV trajectory profile for an expansion process with a expansion ratio of 6

the trajectory is very close to the adiabatic trajectory and as expansion flow rate decreases, the trajectories approaches the isothermal line.

Total amount of potential energy, actual work output and expansion efficiency can be calculated using equation 2.7, 2.8, 2.9.

$$W_{out} = \int_{V_0}^{V_e} (P(t) - P_{atm})dV + (P_c - P_{atm})V_0 \quad (2.7)$$

$$E_P = P_c V_0[\ln(r)] - [P_{atm}(V_{iso} - V_0)] + (P_c - P_{atm})V_0 \quad (2.8)$$

$$\eta_e = \frac{W_{out}}{E_P} = \frac{\int_{V_0}^{V_e} (P(t) - P_{atm})dV + (P_c - P_{atm})V_0}{P_c V_0[\ln(r)] - [P_{atm}(V_{iso} - V_0)] + (P_c - P_{atm})V_0} \quad (2.9)$$

For this case, $r = 6$, $P_0 = 1.26\,x10^6$ Pa, $V_0 = 95.7x10^{-6}m^3$, $V_e = 563.2x10^{-6}m^3$, $V_{iso} = 574.2x10^{-6}m^3$, $t_e = 7.42s$. The corresponding W_{out}=265 J, E_P =281 J and efficiency η_c=92.2%. With the calculated work output, W_{out}, total compression time, t_e, and the given volume of the expansion chamber, V_E, the power density, ρ_c, can be calculated using equation 2.10:

$$\rho_e = \frac{W_{out}}{t_c V_E} = \frac{265}{7.42s*715cc} = 50.0kW/m^3 \quad (2.10)$$

Appendix D

Sample uncertainty analysis

A sample uncertainty analysis for a baseline compression process is carried out following Kline and McClintock's method. The compression process has a compression ratio r=10, initial volume $V_0 = 715$ cc, work input $W_{in} = 207.05$ J and compression efficiency $\eta_c = 78.18\%$.

Part I: Uncertainty for volume data and pressure data

Variable:

Constants:

Uncertainty:

$V_0 = 715\ \text{cm}^3$ $\quad W_{V0} = 2.0\ cc$

$P_0 = 14.25$ psi $\quad W_{P_0} = 0.25$ psi

$T_0 = 298$ K $\quad W_{T_0} = 1K$

$P_{eq} = 97.96$ psi $\quad W_{P_{eq}} = 0.5\ psi$

$P_c = 142.64$ psi $\quad W_{P_c} = 0.25\ psi$

$V_{iso} = 71.5\ \text{cm}^3$ $\quad W_{V_{iso}} = 0$

$r = 10$ $\quad W_r = 0$

Since the volume measurement is calibrated based on equilibrium volume, it is necessary to determine the uncertainty of the calibration:

$$V_f = \text{V}_{\text{eq}}(P_0, V_0, P_{eq}) = \frac{P_0 V_0}{P_{eq}} = \frac{14.25\ psi\ x715\ cc}{97.96\ psi} = 104\ cc$$

Using Kline and McClintock's methods, the uncertainty of V_f can be calculated as:

$$W_{V_f} = \sqrt{(\frac{\partial V_{eq}}{\partial P_0} W_{P_0})^2 + (\frac{\partial V_{eq}}{\partial V_0} W_{V_0})^2 + (\frac{\partial V_{eq}}{\partial P_{eq}} W_{P_{eq}})^2} = 1.92\ cc$$

Part II: Uncertainty for work input

Once the uncertainty for pressure and volume is calculated at an initial state and a final state, the error band can be applied to the PV trajectory of the compression process, which is shown in figure D.1:

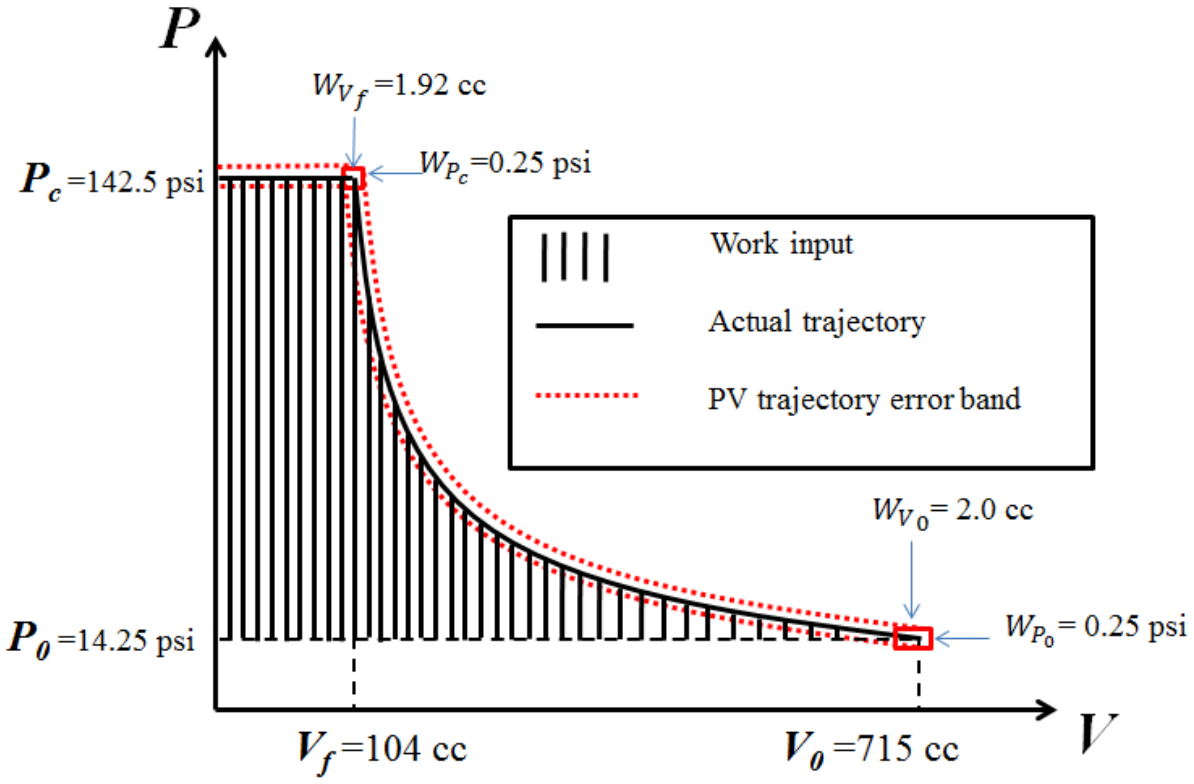

Figure D.1. Sample pressure volume trajectory profile with error bands for a compression process with a compression ratio of 10

Where the area shaded by the solid black line represents the work input $W_{in} = 207\ \mathrm{J}$. It is calculated using the MATLAB imbedded integral function "*trapz*". The dashed red lines are the error bounds for the PV trajectory and the total uncertainty in the

work input can be estimated to be the area bounded by the red dashed lines. For simplicity, the total area can be calculated separately, the top left corner is the uncertainty for isochoric cooling work plus ejection work and it can be treated as a rectangular with a fixed width of $V_f = 104$ cc , and a fixed height of $W_{Pc} = 0.25\ psi = 1723.7Pa$. The area of the rectangular is 0.18 J. For the uncertainty along the compression process, it can be approximated as a trapezoid with a top width equal to $\mathrm{W}_{\mathrm{V}_f} = 1.92$cc , a bottom width of $\mathrm{W}_{\mathrm{V}_0} = 2$ cc , a height of $P_c - P_0 = 128.25$ psi $= 884.25$ kPa . The area of this trapezoid is estimated to be $(P_c - P_0)\frac{\mathrm{W}_{\mathrm{V}_f}+\mathrm{W}_{\mathrm{V}_0}}{2}$ =1.73 J. So the total uncertainty for work input $W_{W_{in}}$ is 0.18 J+1.73 J =1.91 J. The percentage error for work input is calculated to be 0.924%.

Part III: Uncertainty for Efficiency

The efficiency for compression is defined as 2.5 in chapter two:

$$\eta_c = \frac{E_P}{W_{in}} = \frac{P_0 V_0 \left[\ln(r) + \frac{1}{r} - 1\right] + (P_c - P_0)V_{iso}}{W_{in}} \tag{2.5}$$

Assuming r =10 and $V_{iso} = 71.5$cc is the ideal final volume of the air if it is compressed isothermally. With the unknown uncertainty $W_{P_0}, W_{V_0}, W_{P_c}, W_{W_{in}}$ and using Kline and McClintock's methods, the uncertainty of η_c can be calculated as:

$$\mathrm{W}_{\eta_c} = \sqrt{(\frac{\partial \eta_c}{\partial P_0} W_{P_0})^2 + (\frac{\partial \eta_c}{\partial V_0} W_{V_0})^2 + (\frac{\partial \eta_c}{\partial P_c} W_{P_c})^2 + (\frac{\partial \eta_c}{\partial W_{in}} W_{W_{in}})^2} = 1.5\%$$

Appendix E

Drawings for high pressure compression/expansion chamber

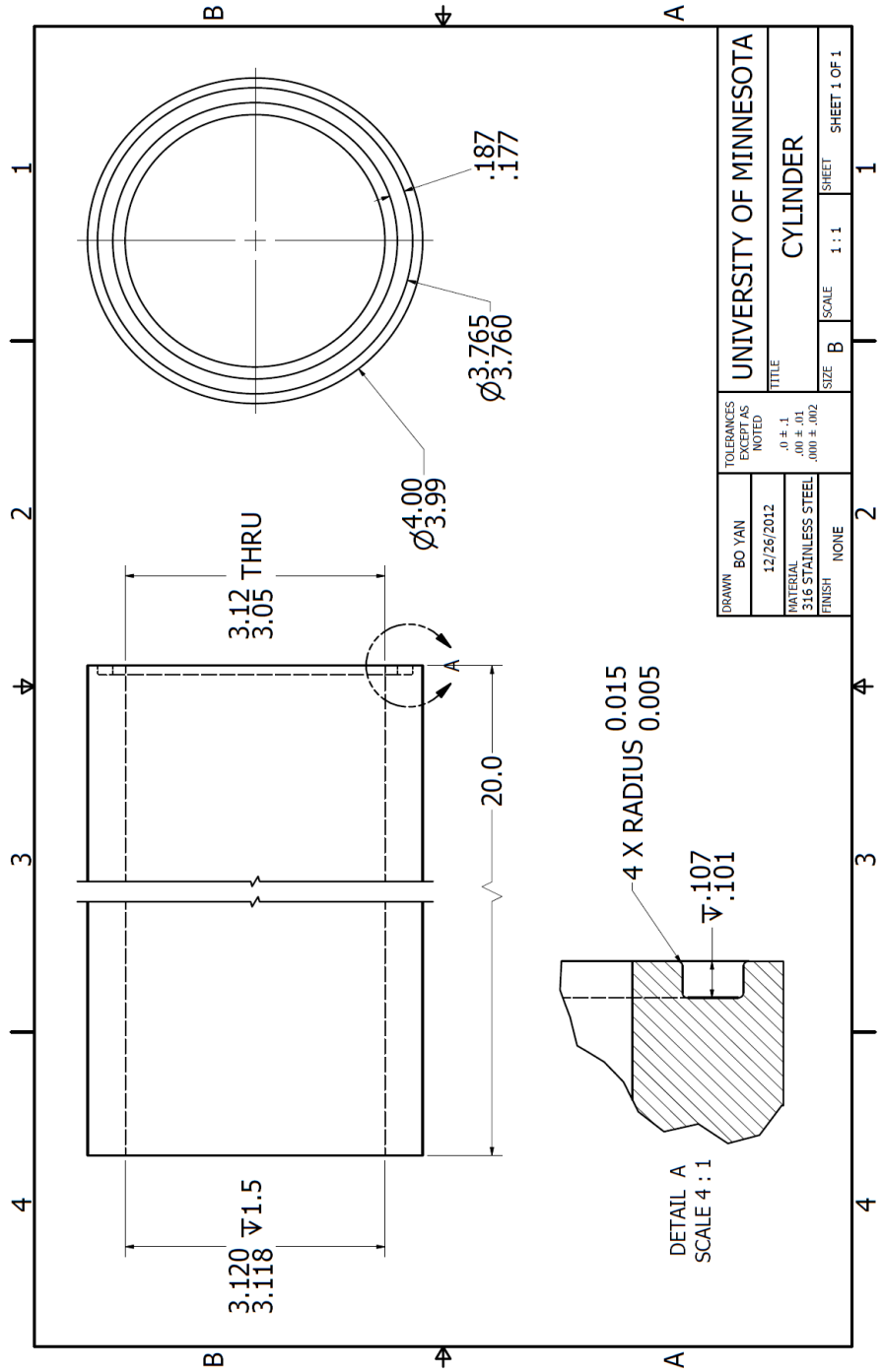

Figure E.1. Detailed engineering drawing for the middle tube for the high pressure compression/expansion chamber

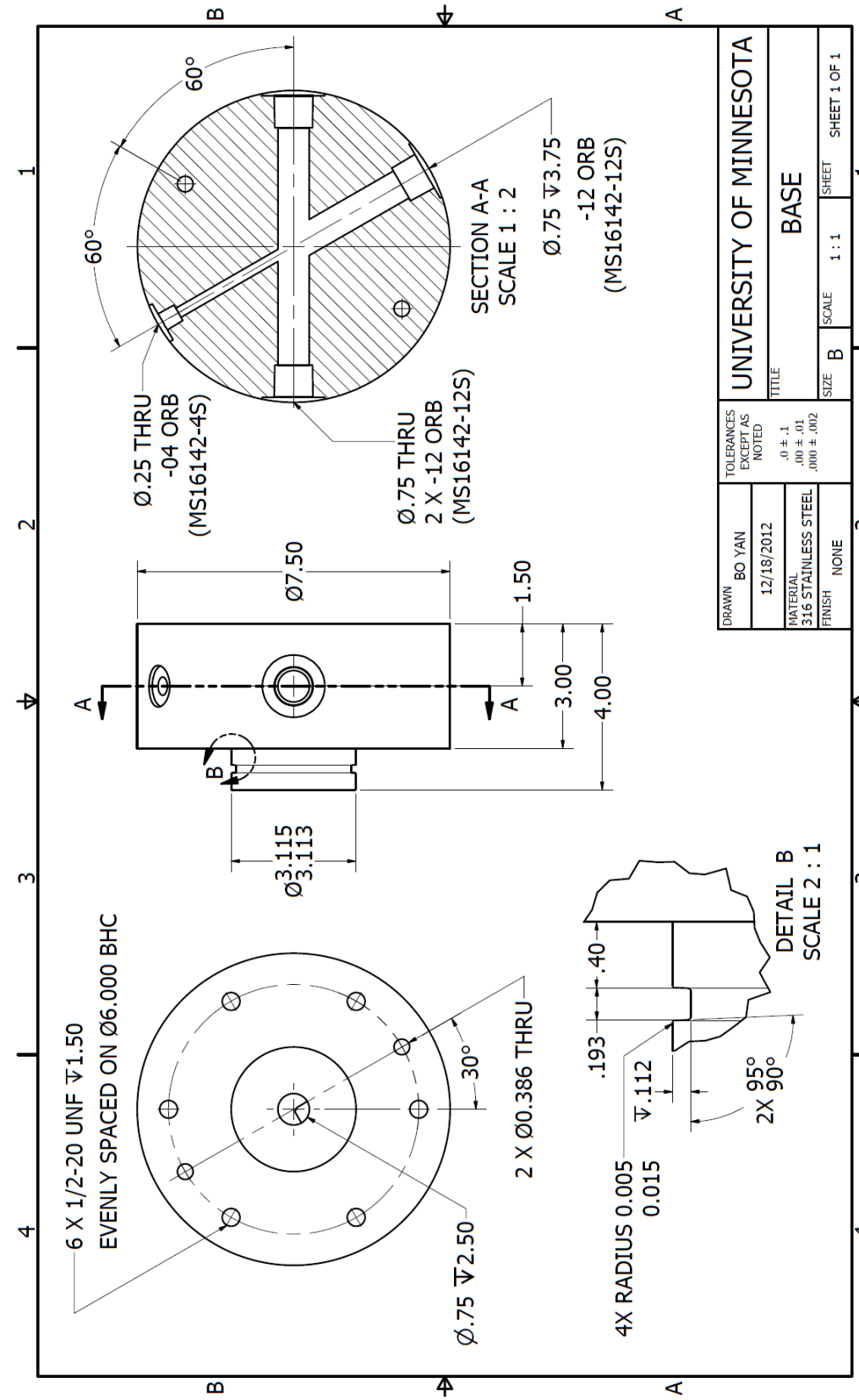

Figure E.2. Detailed engineering drawing for the base of the high pressure compression/expansion chamber

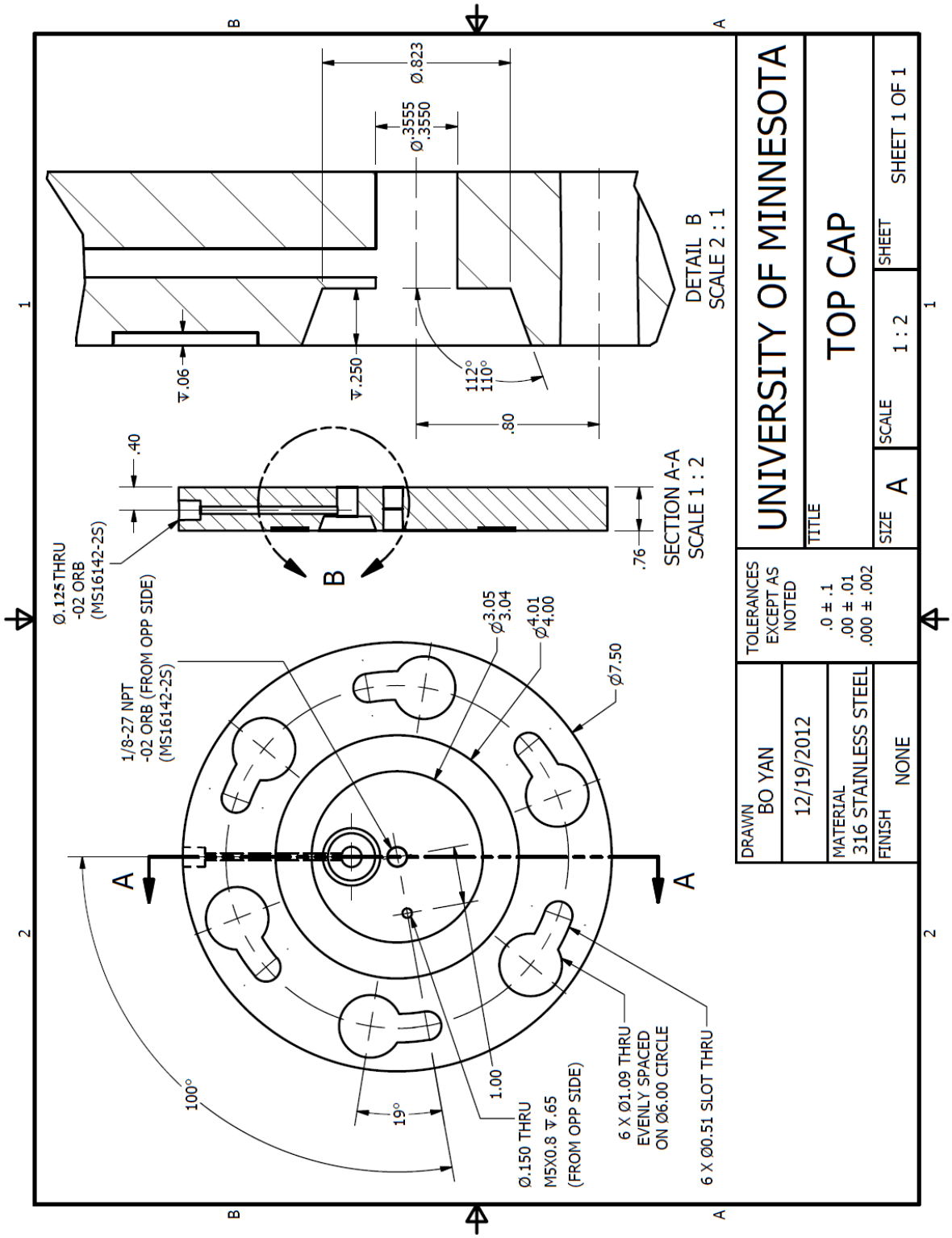

Figure E.3. Detailed engineering drawing for the top cap of the high pressure compression/expansion chamber

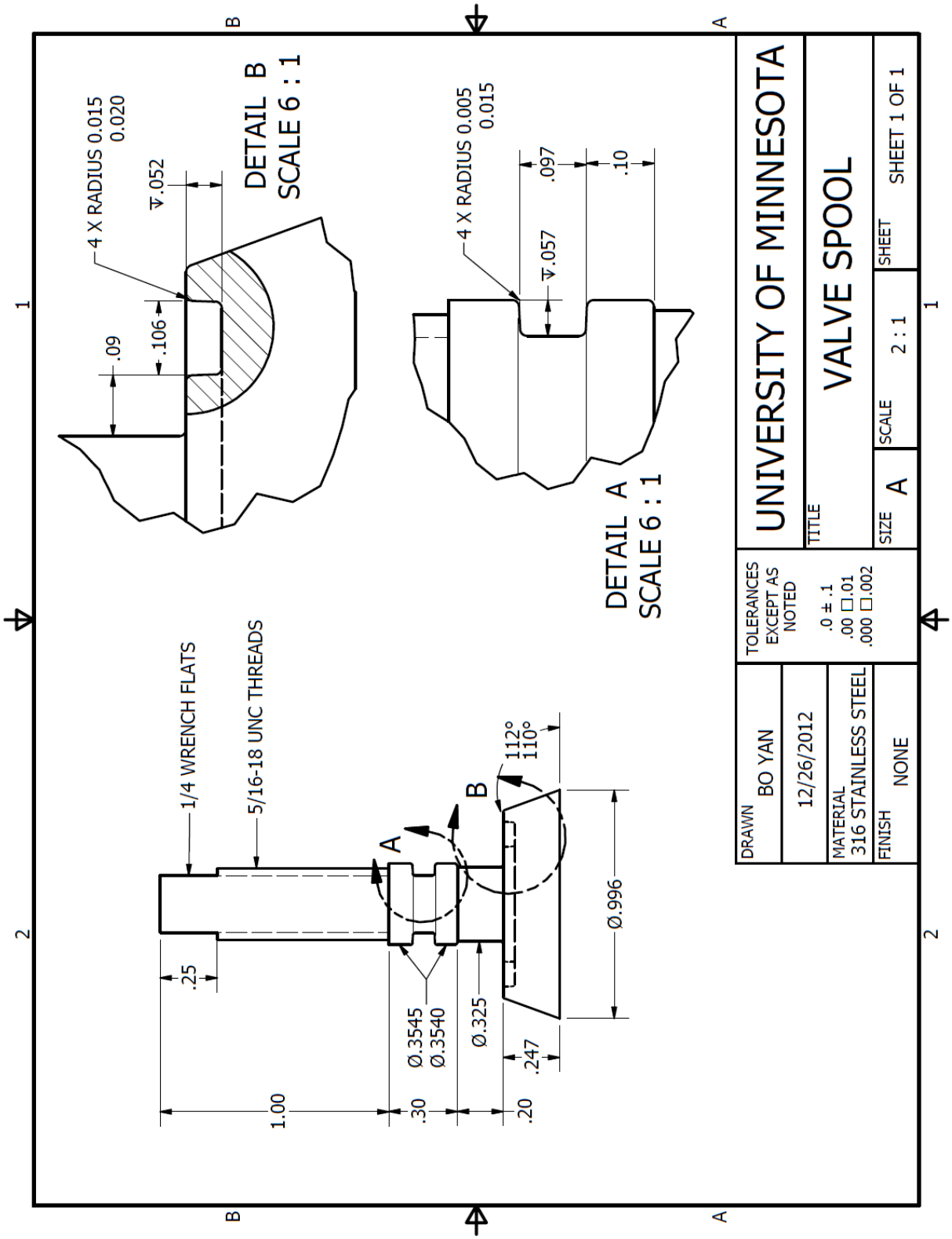

Figure E.4. Detailed engineering drawing for the spool valve of the high pressure compression/expansion chamber

Table E1: Bill of materials for the components of the high pressure compression chamber

Item	Description	Vendor	Material	Quantity
1.	Compressor Chamber Cylinder	McMaster	316 Stainless Steel	1.00
2.	Compressor Base	LightSail Energy	304 Stainless Steel	1.00
3.	Compressor Cap	LightSail Energy	304 Stainless Steel	1.00
4.	Spool Valve	LightSail Energy	304 Stainless Steel	1.00